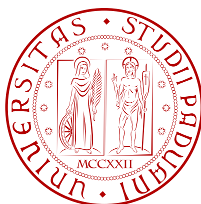

UNIVERSITÀ DEGLI STUDI DI PADOVA

DIPARTIMENTO DI FISICA E ASTRONOMIA
"GALILEO GALILEI"

CORSO DI LAUREA MAGISTRALE IN FISICA

Tesi di Laurea Magistrale

Influence of surface pre-treatments on the growth of $InAs$ nanowires on Si substrates: experiments and ab-initio simulations

Laureando:
Nicoló SARTORI
matr. 1104736

Relatore:
Dott. Enrico NAPOLITANI
Correlatore:
Dott. Filadelfo CRISTIANO

Anno accademico 2015/2016

Contents

Abstract **3**

Sommario **5**

1 Introduction **7**

1.1 Nanoelectronics 7

1.2 Semiconductors and nanowires 8

1.3 Experimental state of the art 12

1.4 *Ab-initio* simulation state of art 16

1.5 Purpose 17

2 Experimental tools **19**

2.1 Molecular Beam Epitaxy 19

2.1.1 RHEED fluxes calibration 22

2.1.2 H plasma cell 24

2.2 Electron Microscopy 27

2.2.1 Scanning Electron Microscope 28

2.2.2 Transmission Electron Microscope 31

2.3 Ellipsometry 35

2.4 Atomic Force Microscope 36

3 Growth on unpatterned Si(111) surface **39**

3.1 Surface treatments and growth parameters 40

3.2 TEM and EDX characterization of the best NWs 44

3.3 H plasma effect 52

4 Growth on patterned Si(111) surface **57**

5 *Ab-initio* simulations **63**

5.1 Substrate construction and approximations . . . 63

5.2 The H-terminated $Si(111)$:1x1 surface . . . 67

5.3 The As-terminated $Si(111)$:1x1 surface . . . 74

6 Conclusions and prospectives **81**

Appendix A *H* plasma cell starting procedure **85**

Appendix B TEM sample preparations **87**

B.1 Holey carbon grid . . . 87

B.2 Focused Ion Beam Lamellae . . . 88

Appendix C Silicon oxide patterning **91**

Appendix D Simulation theory and approximations **93**

Acronyms **100**

Abstract

This thesis reports about the influence of silicon surface pre-treatment on the nucleation and growth of indium arsenide nanowires. Several processes are applied on a silicon(111) substrate before nanowires growth takes place through a solid state Molecular Beam Epitaxy system. In particular the influence of hydrofluoric cleaning, thermal annealing and hydrogen plasma treatment is investigated. The key point in the experimental procedure is that the growth is performed without an external catalyst, so by *self assisted* and/or *selective area epitaxy.* Thus, in this framework it is expected that the surface conditions are more relevant then in an *catalyst assisted* growth. Scanning Electron Microscope and Transmission Electron Microscope are used as main characterization tools for fully grown samples, while Ellipsometry and Atomic Force Microscope are used to analyze surface treatments effects.

At the same time, a simulation activity has been carried out: even if several physical models have been elaborated on nanowires nucleation, none of them goes entirely thorough the physical phenomena happening. With this uncertain theoretical background, a first principles approach has been used to better understand how As and In interact on simple possible surface configurations. The aim is to acquire sufficient information to elaborate a kinetic Monte Carlo simulation about the nucleation stage.

Sommario

Questo lavoro di tesi analizza come i trattamenti superficiali di un substrato di silicio influenzino la nucleazione e la crescita di nanofili di arseniuro di indio. Diversi processi sono applicati ad un substrato di silicio (111) prima della crescita che avviene tramite epitassia a fasci molecolari da sorgenti a stato solido. Il punto chiave della procedura sperimentale è che la crescita è effettuata senza l'utilizzo di un catalizzatore esterno, cioè esclusivamente tramite *self assisted epitaxy* e/o *selective area epitaxy*. Dunque, in questo contesto ci si aspetta che le condizioni della superficie siano più rilevanti rispetto ad un processo di crescita assistita da catalizzatori eterni. Il microscopio elettronico a scansione e a trasmissione sono utilizzati come principali strumenti di caratterizzazione dei campioni totalmente cresciuti; invece, l'ellipsometria e il microscopio elettronico a forza atomica sono utilizzati per analizzare gli effetti dei trattamenti sulla superficie.

Al contempo si è svolta un attivita di simulazione: anche se esistono molti modelli fisici sull nucleazione dei nanofili, nessuno di questi è totalmente esaustivo sulla descrizione dei fenomeni che avvengono. A cause di questo contensto teorico incerto, si è adoperato un approcio a principi primi per comprendere meglio come In e As interagiscono sulle possibili configurazioni superficiali basilari. L'obiettivo è quello di raccogliere sufficienti informazioni in modo da poter successivamente implementare un modello cinetico Monte Carlo sulla fase di nucleazione.

Chapter 1

Introduction

1.1 Nanoelectronics

Nanotechnology is the collection of all the interconnected applied sciences studing structures or phenomena with at least one characteristic size of less than few hundreds nanometers. One of its discipline is nanoelectronics that deals with the development of nanoscaled electronic components as for example transistors. These are the fundamental blocks of all digital devices, from PC to microwave oven, from TV set to filming camera, so that it is impossible to find a modern device without them. Taking into account that almost all today activities involve the use of electronic devices, it is easy to understand why nanoelectronic research has such an important role in modern society.

Until now, the micro-nanoelectronic industry has satisfied the market request for faster, more compact and energy efficient products either by reducing the minimum feature size of basic circuits or by introducing new architectures. This technological run is well depicted by the empirical Moore's law which states that the number of transistors in a processor double every two years (Fig. 1.1 (a)). The challenge that nanoelectronics is facing now is that, in commercial products, the downscaling has reached a minimum feature size of $14\,nm$ [1]. At this scale many negative intrinsic phenomena, such as leakage current, are becoming greater and greater and Silicon (Si), the main material of electronic devices, is already pushed to its limit[1]. It is foreseen that in the 2020 it will be possible to reach a minimum feature size of $5\,nm$ on Si, however, after this node, a new innovation will be required. Knowing this limit from long time, research has focused on new materials, such as Indium Arsenide ($InAs$) or Gallium Phosphide (GaP), and also on new architectures such as tri-dimensional structures. Actually the latter has already

[1] The mobility of carriers in silicon has already be enanched by using the effect of strain on their effective mass.

been implemented in commercial processors. Indeed, in 2011 the 3D gate was introduced by Intel [2](Fig. 1.1 (b)), but up to now no commercial processor based on a different material from Si was ever created.

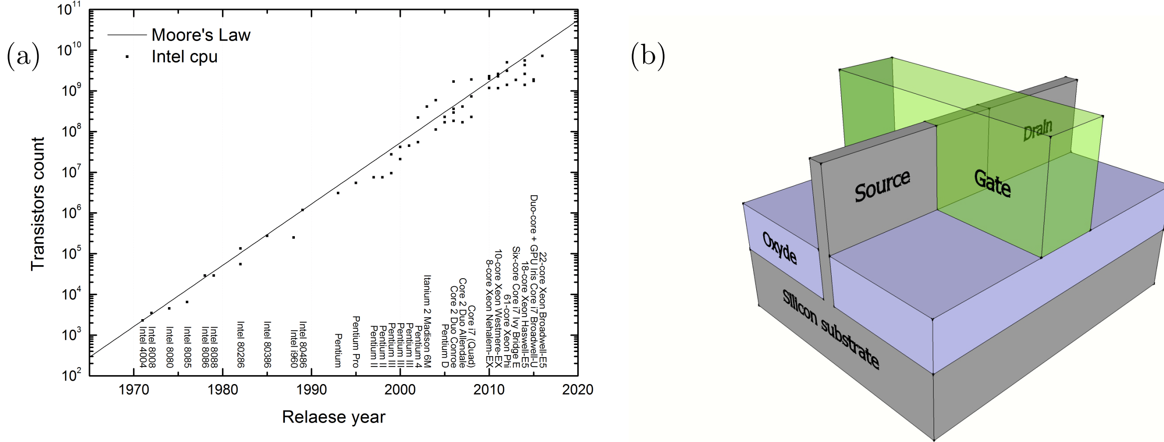

Figure 1.1: (a): Moore's law for Intel cpu from 1971 to 2016. (b): schematic of a tridimesional gate transistor.

The lack of products made of innovative materials is in first place due to their high manufacturing cost, though the interest toward them is as much high due to their really peculiar performances. It is also worth noting that it would be extremely expensive for chip industries to change their production from Si based technology to a new technology. To overcome these obstacles the main idea is to find ways to integrate innovative materials on silicon substrates.

1.2 Semiconductors and nanowires

All electronic devices are based on semiconductors. These materials have a energy band structure with an energy interval in which no electron states exist. This region is called *energy gap* (E_g) and it is such that electrons can be excited from the lower band, *valence band* (VB), to the upper band, *conduction band* (CB), just by thermal excitation. Therefore the E_g takes values between some tenth of eV and few eV and the gap can be of two types: it is *direct* if the maximum of the VB and the minimum of the CB are at the same point; otherwise it is *indirect*. It is important to underline that the energy band structure is strongly related to the periodic crystal structure and every imperfection or defect has an influence on it. Considering pure semiconductors, it is possible to recollect them in a diagram E_g vs the lattice constant (see Fig. 1.2). In this figure continuous and dashed lines indicate the properties of the alloy between the materials at the extremes and the absence of lines between the left and the right group is due to their different

crystal structure: the previous has a wurtzite phase (WZ), the latter has a diamond/zincblend phase (ZB). Among all the represented materials the most used ones belongs to two categories: *group IV elemental semiconductors* are composed of a single chemical element from group IV (i.e. Silicon *Si* and Germanium *Ge*); *group III-V compound semiconductors* are composed of a pair of elements, one from group III and one from group V with 1:1 ratio (Indium Arsenide *InAs*, Indium Phosphide *InP*, Gallium Nitride *GaN*, etc).

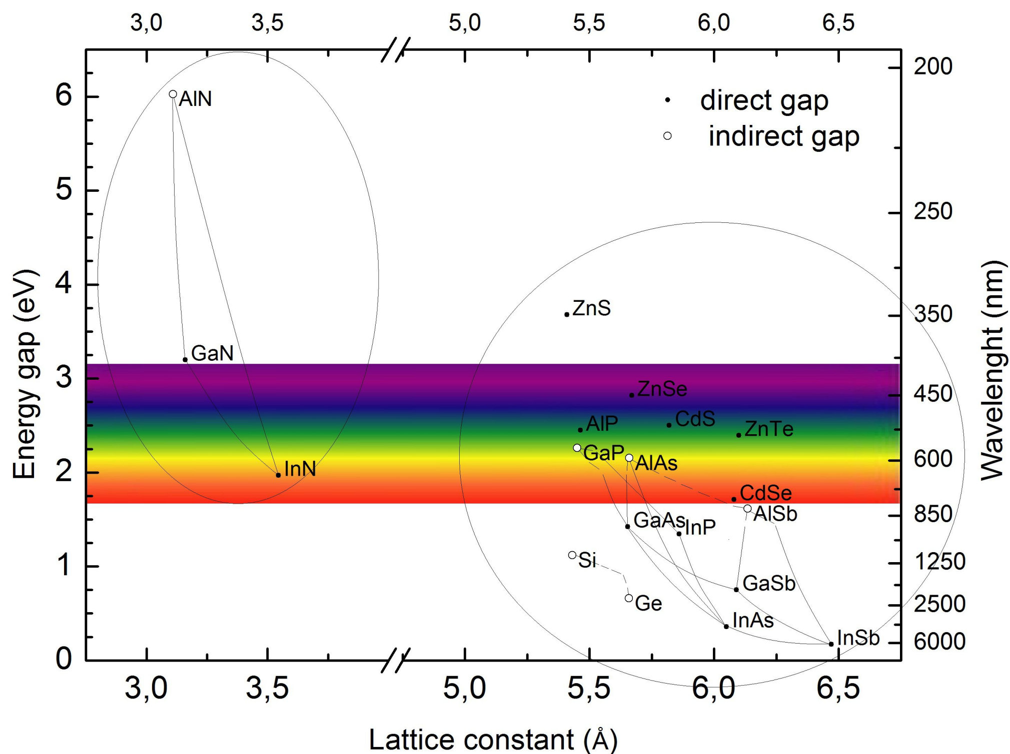

Figure 1.2: Energy gap vs lattice constant of main semiconductors. In the left circle the crystal phase is *wurtzite*, in the right one it is *diamond/zincblend*. Lines rapprensent properties of alloys and are dashed if the gap changes position.

Even if it is possible to create with ease alloys using semiconductors with different lattice constants (but same crystal structure), it is normally impossible to create a perfect junction between two pure phase of them. This is due to the omnipresent discrepancy of lattice constant among all possible combinations of semiconductors. Indeed, even just few percent points of mismatch can lead to the inability of generating the continuous and ideal desired junction. The process of depositing materials on each other to form a junctions is called epitaxy and it is distinguished between *homoepitaxy* or *heteroepitaxy* if materials are the same or not, respectively. Epitaxy greatest strength is that the deposited material tends to follow the substrate crystal

phase and orientation even if they are different; however in the case of heteroepitaxy the lattice constant mismatch between the two materials generate a stress at the junction. If only few atomic layers of material are deposited or if the mismatch is small, the stress is accumulated as elastic energy and normally a non-equilibrium film is obtained. Instead, when the deposited layer becomes too thick or the mismatch is too large, the strain is relieved by the formation of dislocations (Fig. 1.3). It is well known that these dislocations are detrimental for the proper working of devices because they act like a recombination point for carriers and it might also happen that they propagate through the material inducing more defects or imperfection, thus changing the semiconductor properties.

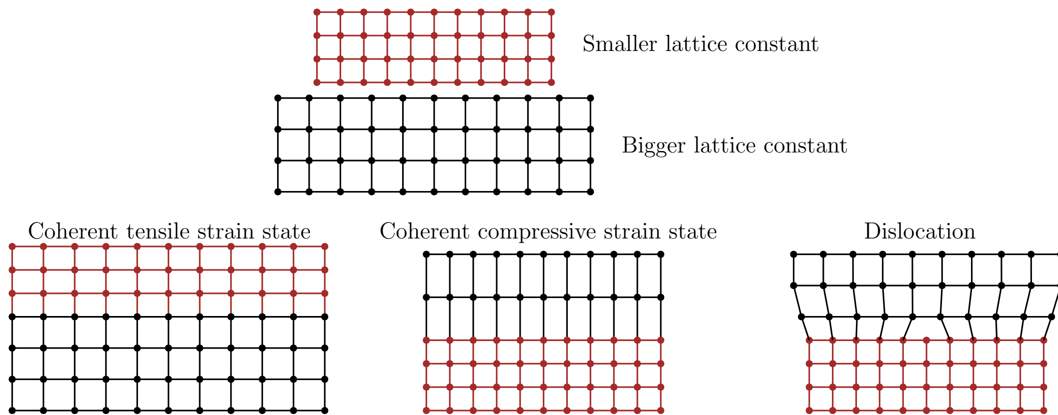

Figure 1.3: Not-scaled schematics of the most simple deformations due to lattice mismatch.

It has been proven in many articles [3, 4, 5] that is possible to eliminate, or at least reduce, junction imperfections by growing on a substrate vertical standing rods, the *nanowires* (NWs) (Fig. 1.4 (a)). They are simply exagonal shaped crystals with a length several times longer then the diameter, so that they are like wires. With their peculiar geometry, the contact area between substrate and nanowire is very small and this allows the mismatch to be accommodated only at the interface, so that the upper grown nanowire is unaffected by defects or strain [3, 4, 5]. In particular, in [3], Tomioka et al. suggested that if the nanowire diameter is lower then the mean distance between dislocations caused by lattice mismatch, no dislocations at all would affect the junction. This property, together with the possibility of building them with peculiar materials, has risen interest in NWs research and applications. In fact, III–V heterostructure nanowires can be grown epitaxially on Si and this enables the integration of optoelectronic III–V devices with Si technology (which is a long-time goal for the semiconductor industry). Nowadays the challenge is to get the best possible control on all nanowires properties: diameter, length, position, reciprocal distance, vertical yield, crystal phase and so on. The aim is to obtain an independent control on

all these characteristics; for this purpose, many fabrication techniques have been developed and the chemical-physical processes behind nanowires formations are largely studied. As we will see more in detail later, despite NWs are know since 1964, when Wagner and Ellis reported on the vapor-liquid-solid growth mechanism for the growth of elongated crystals[6], still not all growth processes have been fully explained.

In general NWs can be fabricated with two approaches: the bottom-up (B-U) methods rely on chemical self assembly of NWs on a substrate (i.e. epitaxy); the top-down (T-D) fabrication is based on a selective etching of a patterned planar material (i.e. lithography). Each method has its own advantages and drawbacks: the B-U route enables NWs to be grown using a large variety of materials, however it is expensive and the NW growth control is still not perfect; the T-D approach may be quickly integrated into standard CMOS processes with its good reproducibility and NW growth control, but it does not grant the same junction quality as B-U processes.

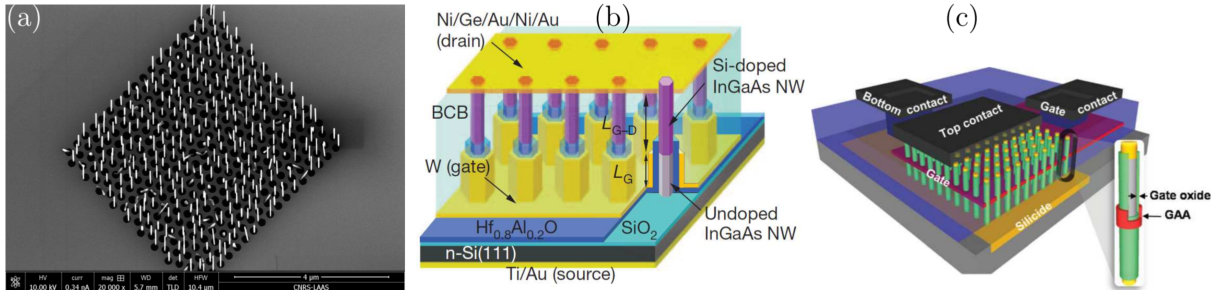

Figure 1.4: (a) Array of NWs growth on patterned oxide mask. (b) Tomioka's gate-all-around FET architecture (pic. from [7]). (c) Larrieu's gate-all-around FET architecture (pic. from [8]).

From the previous statements, it is clear that the hetero-epitaxial growth of NWs solves the problem of different materials integration. Indeed, this technology has already been used in several field such as electronics, optoelectronics, energy development and environment protection and it has made possible the production of high performance devices like solar cells [9, 10, 11], lasers [12, 13, 14], photodetectors [15], integrated photonic circuits [16] and biological and chemical sensors [17]. In most of these works a III-V semiconductor is used due to its peculiar opto-electronic properties in combination with a low cost substrate that does not change its performance. Moreover, going back to the transistors development and fabrication, the integration of III–V semiconductor NWs directly onto Si substrate has emerged as a feasible way to create cost competitive CMOS architectures. In [7] and [8] Tomioka's and Larrieu's groups, respectively, reported about gate-all-around FET based on nanowires; both works underline as the proposed architectures have a high potential but further research in NWs control is needed to downscale them.

1.3 Experimental state of the art

This thesis is inserted in an ambitious project that aims at the realization of a nanowire based gate-all-around transistor. To reach this purpose a huge amount of time and many efforts are required, thus the present work will be able to cover just a small part of the whole activity. The first step is to develop a reproducible and trustworthy procedure to grow nanowires with controlled properties. In particular, for the moment, the research is focused on Indium Arsenide, a III–V semiconductor with a small energy gap of $E_g \approx 0.35\,eV$ so that also its resistance is low, $R \approx 0.16\,\Omega/cm$. The interest toward $InAs$ is justified by the fact that it offers a very small electron effective mass allowing very high electron mobility, high injection velocities, as well as surface Fermi level pinning which facilitates easy formation of low resistance ohmic contacts. In addition, several applications of this material properties have already been proposed; for example if it is alloyed with $GaAs$ it enables a wide direct band tuning from 0.36 to $1.42\,eV$, opening up attractive NW photonic device applications; or if a heterojuction is formed between $InAs$ and $GaSb$, it would be of type II, thus allowing for the realization of tunneling field effect transistors.

The studied $InAs$ NWs are grown on a $Si(111)$ substrate using a solid state Molecular Beam Epitaxy machine (MBE) with a *catalyst free* process (B-U approach). Although almost all commercial transistors are built on $Si(100)$, the different choice of substrate taken in this work is due to the serious difficulties presented by the growth of vertical III–V NWs on other Si facets then the (111). The actual intention is to study in details the growth in this easier configuration so that later it will be possible to transpose the acquired knowledge on more difficult ones. As already explained, because epitaxy allows to follow with ease the substrate crystal orientation, it is expected that the NWs would follow the (111) substrate direction, thus growing vertically. However, in this configuration, III–V materials in ZB phase have four possible growth directions due to the two possible surface terminations of the Silicon substrate. In an ideal flat surface, if the growth starts with the $InAs$ (111)B plane, i.e. the surface is As-incorporated or In-terminated, then the NWs are vertical; otherwise if it starts with the $InAs$ (111)A plane, i.e. the surface is In-incorporated or As-terminated, then the NWs are inclined with an angle of $19.6\,^\circ$ to the surface. These surface conditions are schematically represented in Fig. 1.5 and it is worth noting that, due to the symmetry of the crystal, the (111)A starting condition can lead to three growing direction, making a total of four possible directions with the (111)B vertical one. The matter has been discussed by Tomioka et al. in [3] where they propose a procedure to ensure good vertical yield for a *selective area* Metal-Organic Vapor Epitaxy process (MOVPE). They suggest that the

direction control problem is strongly related to the polar/nonpolar nature of the two materials ($InAs$ and Si respectively) but with a good surface cleaning procedure, low roughness and a flow-rate modulation at the start of the epitaxy, a vertical yield of 95% can be obtained.

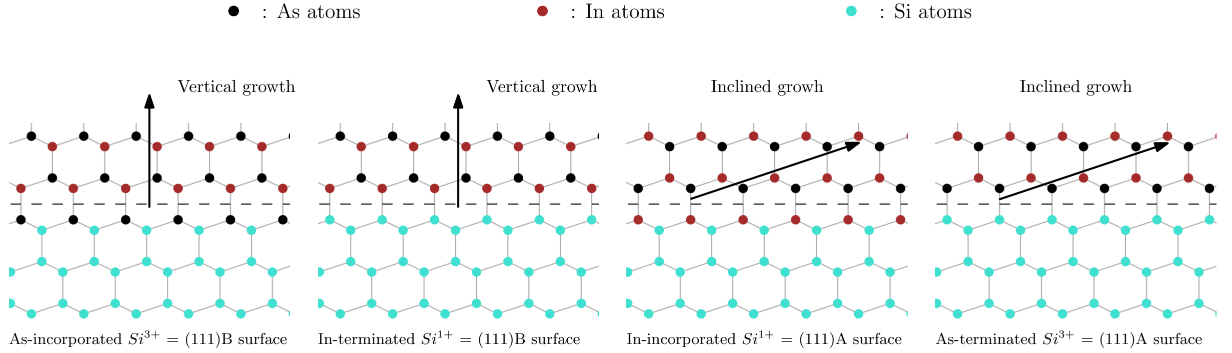

Figure 1.5: Ideal possible surface terminations for an $InAs$ film epitaxialy grow over a perfect Si substrate.

At this point it is mandatory to underline that the technique called Metal-Organic Vapor Epitaxy or Meral-Organic Chemical Vapor Deposition (MOVPE - MOCVD) is strongly different from the Molecular Beam Epitaxy (MBE) because different physical-chemical phenomena are involved, so that repeating the Tomioka's procedure in our experimental setup can bring quite surely to different results. To further complicate the literature framework is the fact that many surface treatments and preparation techniques have been developed and many parameters have to be specified to uniquely define the experimental situation in which some results are obtained. Because a comprehensive look on the literature about NWs growth is out of the scope of this work, in the following we will only discuss about the most important points that have to be known in order to understand what we are going to explore later.

In addition to the epitaxy machine used, the substrate conditions play a crucial role in the physical-chemical phenomena that take place during deposition. A first distinction exists between processes that use a catalyst to help nucleation and/or growth of NWs and those that do not and that are defined *catalyst free*. In the first case the catalyst is usually a droplet deposited on the surface just before growth takes places; the droplets can be made of the same material of NWs, so that the process is *catalyst self-assisted*, or they can be made of a foreign material, so that the process is *catalyst Au-assisted* if, for exemple, the droplets are made of Au. The *catalyst assisted* processes are often, but not always, driven from the well known mechanism Vapor-Liquid-Solid (VLS) [6, 18, 19]; instead the remaining *catalyst assisted* and quite all *catalyst free* processes are driven by a Vapor-Solid (VS) and/or Vapor-Solid-Solid (VSS) mechanism. Many controversies still exist on which mechanism actually drives a given process but in general the VS and VSS

phenomena are not so well know as the VLS ones. This is due to the fact that it is hard to have an insight view at what is happening during VS or VSS, while this is possible when the mechanism involved is VLS. Indeed, in the latter, a liquid droplet, deposited on the solid substrate, adsorbs particles from the surrounding vapor and quickly gets to supersaturation conditions; then a crystal growth occurs at the base of the droplet and a nanowire rise, lifting the droplet. This has been seen clearly because the catalyzing droplet can be crystallized and studied via Scanning or Transmission Electron Microscope (SEM - TEM). Instead what is believed to happen during VS is that particles from the vapor directly condensates to solid, so that a NW grows due to lower energy configuration created by the facets of a slowly growing crystal. Together with this process it is believed that a VSS can take place: if a crystal is formed via VS, or if a crystal droplet has already been deposited, this brings to a catalyzed process.

In this landscape a key role is played by the surface because many particles from the vapour phase can impinge and stick on it and then diffuse from there. Sometimes the surface is covered by a patterned or not, native or grown, oxide that changes both the diffusion length and the absorption/desorption of the atoms sticking on it from the vapor. In this conditions we talk about: *selective area epitaxy* if the oxide prevents the nucleation of NWs in any place covered by it; *control positioned growth* if the apertures in the oxide are not random but ordered and opened via Electron-Beam Lithography (EBL) or Nano-Imprint Lithography (NIL); *oxide assisted growth* if the nucleation of NWs tends to start at the border between the oxide and the substrate. Instead, if a clean surface is required, many cleaning techniques have been developed to reach the wanted results. Chemical etching, plasma treatment and thermal annealing have been studied and combined with all their variations and parameters; however, to our knowledge, their influence on the NWs growth have been analyzed in depth for $InAs$ on Si substrate only for the catalyst-free MOCVD process [20].

Many articles exist in literature about the investigation of $InAs$ NWs growth on Si substrate but it is worth mentioning at least the followings:

- In [21] Mandl et al. explain how nucleation and growth of self-seeded III-V NWs happen while trying to identify situations in which VLS or VSS take place. In particular, for the formation of $InAs$ NWs via MOVPE, they claim that it is driven by a VLS process in which the presence of an oxide layer is required to immobilize In droplets on the surface and to limit NWs size.

- In [22] Robson et al. make a comparison upon the effect of different growth modes for

MBE; more in details, they explore randomly positioned and patterned Au-assisted growth, catalyst-free growth, Au-assisted selective area epitaxy and simple selective area epitaxy. Within their parameter space, they identify the selective area epitaxy as the mode with the highest yield of vertical NWs.

- In [23] Wang et al. highlight that the oxide layer thickness is an important parameter for self-catalyzed growth when using MOCVD. They suggest that if the oxide has the right thickness ($\approx 10\,\text{Å}$), it helps the formation of good starting nucleation droplets, whereas if it is too thick it doesn't allow the droplet formation, or if it is too thin the droplets become so big that the NWs do not have a good aspect ratio.

- In [20] Jing et al. show the importance of surface cleaning treatments. They performed many tries by combining ozone plasma treatment, buffered oxide etching, rinsing with deionized water for different times with or without ultra-sonification, rinsing with isopropyl alcohol and thermal annealing. From their experiments they concluded that: *"The key to achieve high-yield vertical $InAs$ NW growth is to have a oxide-free Si surface for NW nucleation and oxide patches to hinder formation of large $InAs$ islands."*

A special role is covered by the works of Hertenberger et al. that investigate $InAs$ NWs growth with the most similar conditions to our: *catalyst free* process by *selective area* Molecular Beam Epitaxy (SA-MBE). In [24] they show that is possible to grow good arrays of vertical standing $InAs$ NWs by using a patterned $Si(111)$ substrate. The oxide mask is realized applying EBL to a thermally grown SiO_2 and then a careful etching of the holes is required to increase growth yield from $\sim$ 30% to $\sim$ 90%. In the fabrication process they try also the "recipe for uprightness" suggested by Tomioka ([3]) but no different results are obtained, thus demonstrating independence of the vertical growth yield to the prewetting conditions and the polar/nonpolar nature of the two interfaced materials. This difference underlines how MBE and CVD, even if starting from the exact same configuration, can bring to two totally opposite results. The main point of the article is that two growth regimes exist: (i) for low interwire distances there is a competitive growth governed by redistribution of In adatoms over multiple NWs as well as direct impingement; (ii) otherwise, a diffusion limited growth dominates due to the limited diffusion length of In on the SiO_2 surface. Then, in [25], they demonstrate how the substrate temperature, often called growth temperature (T_g), has a strong influence on NWs diameter and length: there is a T_g window that allows NWs growth and in which a well defined temperature exists that both maximizes length and minimizes diameter, thus, giving NWs with the best aspect

ratio. Moreover, there they declare to not know with which mechanism the NWs are growing, however, with further investigations using RHEED, TEM and SEM ([26]) they totally excluded the presence of VLS. Eventually, in [27] the group largely explores the growth parameters space. The main point is that there is a strong relation between the V/III flux ratio and the best growing temperature, thus the parameters space is quite complicated. Moreover, the existence of a best T_g is justified identifying two regimes: at low T the surface migration length of In adatoms is rather low resulting in higher sticking coefficient and extensive cluster formation; at high T a loss of In is claimed due to thermal desorption of adatoms from the oxide surface and to NWs decomposition.

Comprehensively, a reproducible recipe for NWs is expected by controlling: growth temperature, In and As fluxes[2], growth time, surface cleaning processes, pitch and holes dimensions in a patterned SiO_2 mask.

1.4 *Ab-initio* simulation state of art

As already explained, a valid and globally accepted model for the nucleation and growth of $InAs$ NWs in a *catalyst free* process is still missing. Because of this lack of knowledge, we decided to use a first principle approach (*ab-initio*) both to find the best conditions for NW nucleation and to understand how As and In interact with different Si surface configurations. The *ab-initio* calculation simply considers the system composed of nuclei and electrons and aims to find the configuration with the lowest energy by solving the associated quantum Hamiltonian. Despite this possibility, it is impossible to solve an Hamiltonian that takes in to account the full growing system due to its dimension. Indeed, if we want to simulate the growth of an $InAs$ NW with diameter of $\sim 50\,nm$ and length of $\sim 100\,nm$, the simulation should at least consider a number of nuclei of the order of $10^7 - 10^8$ (with relative electrons), whereas present calculation power and techniques only allow to solve, in a reasonable time interval, the Hamiltonian of a system composed by $\sim 10^4$ atoms; therefore only much much smaller systems can be considered[3]. The problem with this kind of approach resides in the fact that atomistic physical-chemical phenomena that govern deposition, adsorption and diffusion operate with characteristic length and time respectively from 0.1 to $1\,nm$ and from femto– to pico– seconds. Instead, the deposition itself is a much larger scales process that interests an area of few μm^2 and a time of few seconds

[2]Not only the V/III ratio is important but also the neat values due to the influence of In or As flux on itself diffusion length.

[3]Furthermore, the problem is not linear in the number of nuclei and electrons, but has different exponent relation depending on the implemented calculation method.

(time needed to epitaxially grow a monolayer (ML)). The solution to this multi-scale problem is to combine an *ab-initio* method, as Density Functional Theory (DFT), with a statistical mechanics method, as kinetic Monte Carlo (kMC). The idea is to extract with DFT the parameters related to interaction processes between adatoms and surface. Then, the obtained potential barriers, adsorption and interaction energies can be used to implement a kMC simulation to capture the kinetic mechanisms. With this procedure the outcome of the latter step is reliable as the theory that solves the quantum-mechanical Hamiltonian of the nuclei-electrons system, i.e. DFT and other approximations.

In the literature framework, many works exist that make use of the described integration between DFT and kMC, especially for diffusion related phenomena [28, 29, 30]. Despite this, very few of them deal with dimensional scales big as those that interest us, and, up to our knowledge, none of them study our same system (In and As on $Si(111)$ reconstructed surfaces). This is due to the fact that the computational power needed to solve such systems Hamiltonian is available only since the very last decade. On one hand, this let us explore an uncontaminated field, on the other, it deprives us of the possibility of a feedback that has to be sought in the experiments, not always easily.

1.5 Purpose

The experimental work presented in this thesis aims to comprehend the effect of surface pre-treatment on the growth on $InAs$ NWs. The first NWs characteristic that we want to control is their growth direction, namely their uprightness. To reach this objective we know that a really clean surface is mandatory so that the NWs can epitaxially grow directly from the crystal substrate. The growth takes place in a MBE system with a *catalyst free* process and we firstly investigate oxide removal from unpatterned silicon substrates. During the activity, the growing recipe is modified to downscale the NWs diameter because of the ultimate objective of devices application.

The cleaning processes that we use are:

- **HF**: hydrofluoric acid is the commonly used acid for *ex-situ* removal of oxide and of any organic contaminant on the surface;
- **degasing**: it is a mandatory *in-situ* low temperature thermal process to get rid of any gas trapped at the substrate surface before the growth;

- **H plasma**: we investigate if an *in-situ* low energy hydrogen plasma treatment have any effect on the silicon oxide and the NWs features;
- **thermal annealing**: it is performed at different temperatures in the MBE growth chamber, thus *in-situ*.

Firstly, these techniques are performed individually to clearly see the effect of each of them on NWs growth and then their combinations are explored. It has to be noticed that it is difficult to completely know how a given treatment affects the surface because the scale at which we are interested to see these effects is the nanometric one. Therefore, the experimental deductions are based mainly on the characterization of the NWs grown on a treated surface and the knowledge that is acquired about the treatments is mainly indirect. Eventually, direct inspection of particularly interesting surface conditions are carried out without performing the epitaxial growth step.

Each sample is characterized using a Scanning Electron Microscope (SEM) to have a direct and immediate view on vertical yield, density, diameter and length of NWs. Instead, only the best specimen is investigated in depth using Transmission Electron Microscope (TEM) to gain information about the interface between Si and $InAs$, the NWs crystal phase and to check for the presence of any defect. Furthermore, special samples are used to characterize H plasma treatment by using Ellipsometry and Atom Force Microscope (AFM).

The acquired knowledge is transposed to substrates with a patterned thermally grown oxide in order to clean any remaining oxide traces from the bottom of the holes. Here the aim is to obtain ordered arrays of vertical NWs with a very clean surface and investigate how the geometrical properties of the pattern influence their characteristics.

At the same time, to have a better understanding at the not perfectly clear physical phenomena behind the nucleation and growth of NWs, *ab-initio* simulations based on DFT are carried out. As already explained, this approach is used to collect information and data needed for kinetic Monte Carlo models. This part of the work starts from considering simple and idealized surface configurations to find adatoms most stable positions, their adsorption energies and to see how the system reacts to their presence. Then, some chemical reactions with the surface, interaction energies between two or more adatoms and energy barriers are calculated.

Chapter 2

Experimental tools

In this chapter I will report about all the experimental tools used directly in my work. After describing the Molecular Beam Epitaxy (MBE), a specific subsections will be reserved to its RHEED, used for fluxes calibration, and to its Radio Frequency (RF) H plasma cell, used for surface treatments. Then the characterization tools will be presented: the Scanning Electron Microscope (SEM), the Transmission Electron Microscope (TEM), the Ellipsometer and the Atomic Force Microscope (AFM).

2.1 Molecular Beam Epitaxy

MBE is commonly recognized as the most clean, precise and accurate technique developed to perform non-equilibrium epitaxial growth of a wide variety of materials. These are deposited on a substrate after being evaporated from effusion cells in a chamber under ultra high vacuum (UHV). At such low pressures, less than $10^{-7}\,Pa$, the mean free path of evaporated particles is bigger than the distance between the furnaces and the substrate, thus no collision happens among them. This UHV environment, together with MBE features, helps to minimize the incorporation of unwanted impurities and leads to deposited films with higher quality compared to other techniques (MOVPE, CBE). Moreover, it is possible to control the films thickness with the highest accuracy possible: the exact number of deposited atomic layers can be determined because both the growth rates are calibrated with a sub-monolayer per second precision ($0.1\,ML/s$) and the sources are equipped with fast shutters ($0.1\,s$ opening/closing time). Indeed, as we will see later, using the Reflection High-Energy Electron Diffraction (RHEED) allows live monitoring of the growth of a single monolayer and changing the evaporated material at the right instant brings to the creation of an hetero-interface with abrupt atomic termination.

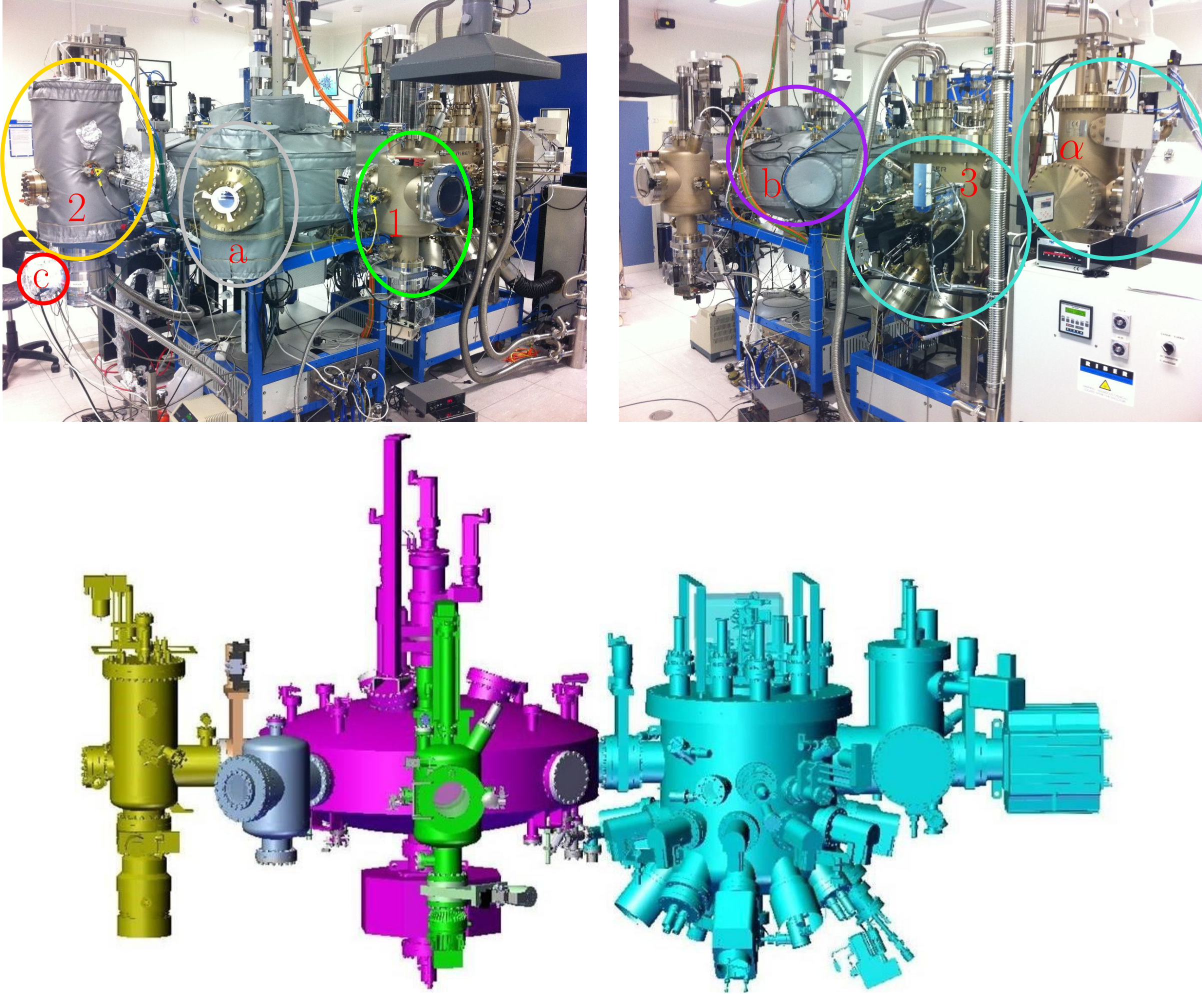

Figure 2.1: Pictures and schematic of the Riber MBE 412 at LAAS-CNRS. The highlighted elements are: 1) loading chamber; 2) degas chamber; 3) growth chamber; *a*) parking chamber; *b*) manipulator chamber; *c*) *H* plasma cell; α) growth chamber pumping system.

All growths reported in this thesis are performed using the Riber MBE 412 of the *Laboratoire d'analyse et d'architecture des systèmes* (LAAS-CNRS) which pictures and schematic are reported in Fig. 2.1. As can be seen, the machine is a multi-chamber system composed by three functional chambers (the numbered ones in the picture) and many other features and tools. The treatment chambers are interconnected by a central manipulator stage and separated by hermetic valves that grant independent UHV to avoid cross contamination. In the following we explain the main features of these chambers.

1. Loading chamber: here samples are loaded inside the machine using a special holder that permits their automatized relocation; a turbo molecular pump (*Varian Turbo-V 551 Navigator*), combined with a membrane pump, rapidly get to high vacuum whenever the door is opened.

2. Degas chamber: here samples can be degased by thermal annealing at temperatures up to $\sim 750\,°C$ for several hours. The heating is provided by a series of coil resistances behind the substrate, while the UHV is granted by an equivalent pumping configuration as in the loading chamber. A specific aperture, normally closed by a valve, connect the "degaser" with a RF hydrogen plasma cell, thus allowing for *in-situ* H plasma treatment.

3. Growth chamber: here is where the materials deposition takes place (schematics in Fig. 2.2). The sample is located at the center of a circular room on a holder made of molybdenum designed to optimize temperature uniformity when the heating coils behind it are turned on. The substrate is facing down towards the source cells that are all in the same symmetric position so that the angle between them and the sample is always the same. To grant a more homogeneous deposition the sample is usually kept in rotation at $13\,rpm$ while its temperature is monitored by a thermocouple positioned at the center of the circular heating coils and at $\sim 1\,cm$ from the surface. This distance is the cause of the relatively big uncertainty on the real temperature of the substrate (up to $\sim \pm 50°C$). Control over the fluxes from effusion cells, valved crackers and RF plasma cells is obtained through their temperatures and relative shutters aperture. Moreover the chamber is equipped with the RHEED system kSA 400, that in this work has been used only for fluxes calibration, and a semiconductor temperature monitor kSA BandiT. In this stage the high vacuum is maintained by liquid N_2 cryopanels that surround the whole chamber in addition to a *Cryo-Torr 8 Cryopump* and an ion pump.

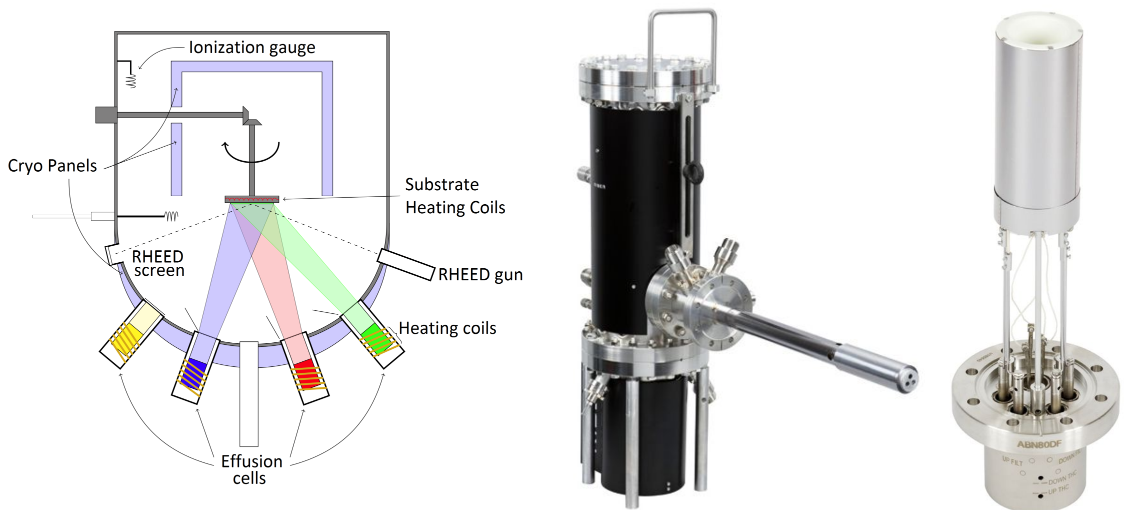

Figure 2.2: On the left, schematic of MBE growth chamber. In the center, picture of an As valved-cracker. On the right, picture of an In effusion cell.

2.1.1 RHEED fluxes calibration

The only sources used in this work are the As valved-cracker cell and the In effusion cell which photos can be seen in 2.2. The calibration that has to be done in this context has the role to connect the growth rate of $InAs$ and the amount of evaporated material from the crucibles. However, because we are interested in calibrating the growth rate of a III-V material, a special procedure has to be followed due to the alternating of III and V planes. In fact, it is clear that in such case the two singular fluxes, of element III and element V, are correlated. The parameters that have to be fixed are the temperature of the crucibles and the opening percentage of relative shutters. This has to be done at a conventional reference point that is given by a well defined growth rate.

The Radiation High-Energy Electron Diffraction (RHEED) is the tool that allows us to do the calibration. In Rheed a collimated mono-energetic electron beam is directed towards the surface at a grazing angle of about 1° with an energy that lies between $5 - 40\, keV$. Since the energy component perpendicular to the substrate is of the order of $100\, eV$, the penetration depth of the beam is limited to the first few atomic layers. As a result, a smooth crystal surface acts as a two dimensional grating which diffracts the incident electrons. A CCD, at the opposite position of the electron gun, collects the diffraction pattern generated by the reflected beam. Knowing the substrate crystal orientation, it is possible, using the Ewald's construction, to predict the diffraction pattern. Actually, what is more important for us in this context, it is that the intensity of the pattern oscillates as a function of time during MBE growth. It has been shown that this effect is the result of oscillations in the surface roughness and that the oscillation period is equal to the time required to deposit one monolayer [31, 32]. A simple model of why this happens is reported in Fig. 2.3: if we start from a perfectly flat surface, the conditions for diffraction are the best possible, thus the intensity of signal is maximum. As a new layer starts to be formed, the increasing roughness reduces the intensity of the diffracted pattern up to when the surface is 50% covered; after this point the intensity increases again because the completion of the new monolayer equals a reduction in the surface roughness. Of course this keeps going in a loop, layer after layer, giving a periodic oscillation in the Rheed pattern intensity. Thus it is possible to estimate the growth rate at given III and V fluxes simply by reading the oscillation frequency.

To actually do the calibration, first a flat surface of element V is obtained by evaporation of a consistent amount of material. Then the RHEED intensity oscillation are studied by keeping the flux of element V turned on and starting the evaporation of element III. The flux of the

latter is fixed so that the growth rate goes to $1\,bilayer/s$[1]. In this situation, for example for $InAs$, the amount of In limits the growth, while the As is in excess. At this point the III flux is fixed and the V flux is reduced down to the minimum value at which the growth rate is still $1\,bilayer/s$. Thus, with this procedure the reference values for temperature of crucibles and openings of shutters are obtained for a given deposition speed. Inserting Bayard-Alpert Ionization Gauge (BAG) in front of the sample allows to link the $layer/s$ speed with the Beam Equivalent Pressure (BEP) of each single material flux. It has to be noticed that this procedure is performed at a temperature of the substrate usually lower that the one used for NWs growth. In our case the one used during calibration is $400-420°C$ while, as we will see later, the usual temperature for NWs growth is $\sim 500°C$.

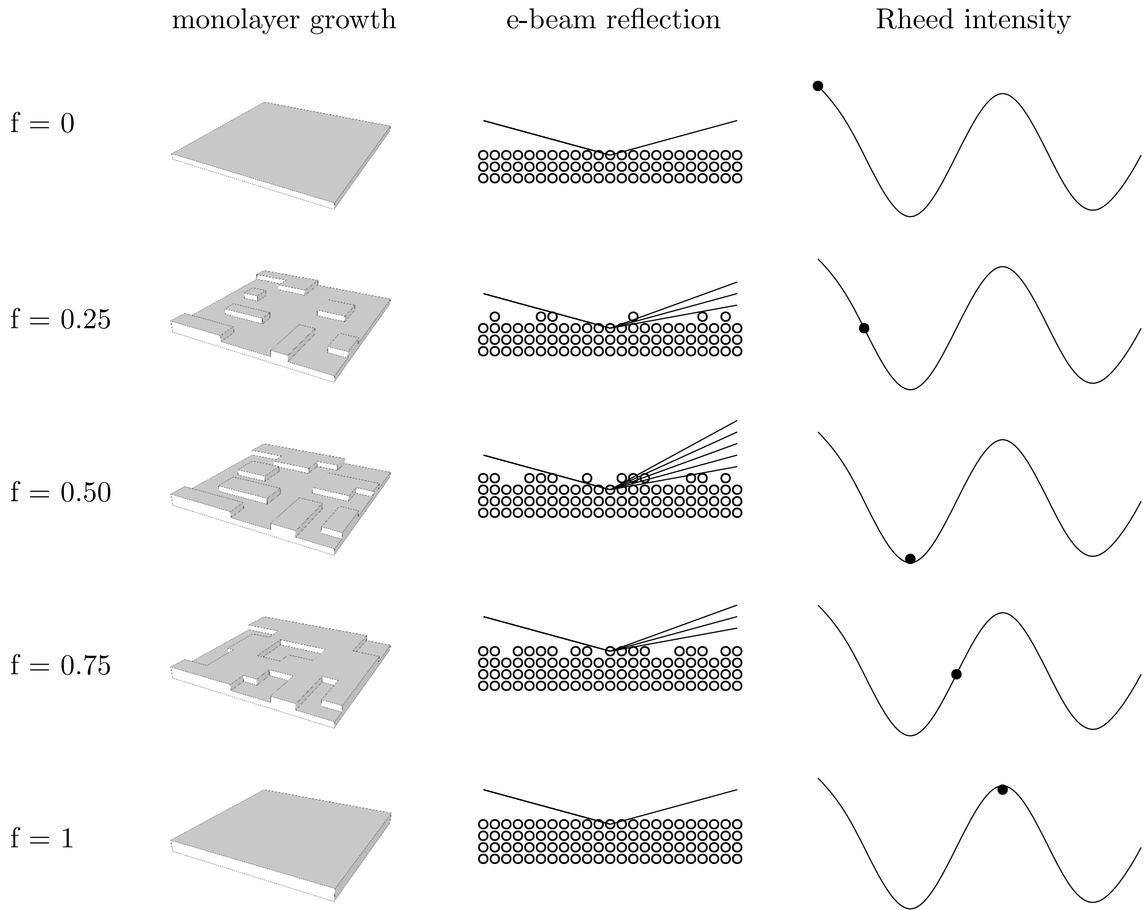

Figure 2.3: Explanation model for Rheed oscillations. f is the percentual converage of the last growing monolayer.

The Rheed equipped on our system is the kSA 400 from k-Space Associated that provides both the electron gun, the acquisition system and the data analysis software.

[1]The word bilayer is referred to the fact that a proper III-V layer is composed by a monolayer of element III and one of element V.

2.1.2 H plasma cell

A Radio Frequency H plasma cell is mounted on the degas chamber in order to perform *in-situ* plasma treatment. The full system, which schematic is reported in Fig. 2.4, is composed by several components: a H_2 bottle at high pressure ($40\,bar$) provides high purity hydrogen, then a pressure regulator and a Mass Air Flow sensor (MAF) allow to finely control the incoming H flow that, in normal regime conditions (valve 1 closed), enters the RF chamber to finally diffuse as plasma in the degas chamber (if metal shutter 3 is open). The valve 5 has just the role to bypass the MAF when the system has to be completely pumped, whereas valve 6 and 4 have the role to isolate different parts of the system if needed. The RF cell is provided by Oxford Applied Research and is equipped both with a water and an air cooling systems that have to carry out the heat dissipated by plasma and radiation in order to keep the system stable. To check the plasma condition an optic sensor measures the intensity of the light emitted and a signal analyzer reveal the amount of irradiated power not absorbed by the plasma. This power, called reflected power, can be reduced to zero by changing the geometrical parameter of the RF cavity using two knobs. The precise procedure to start the plasma is reported in the Appendix A.

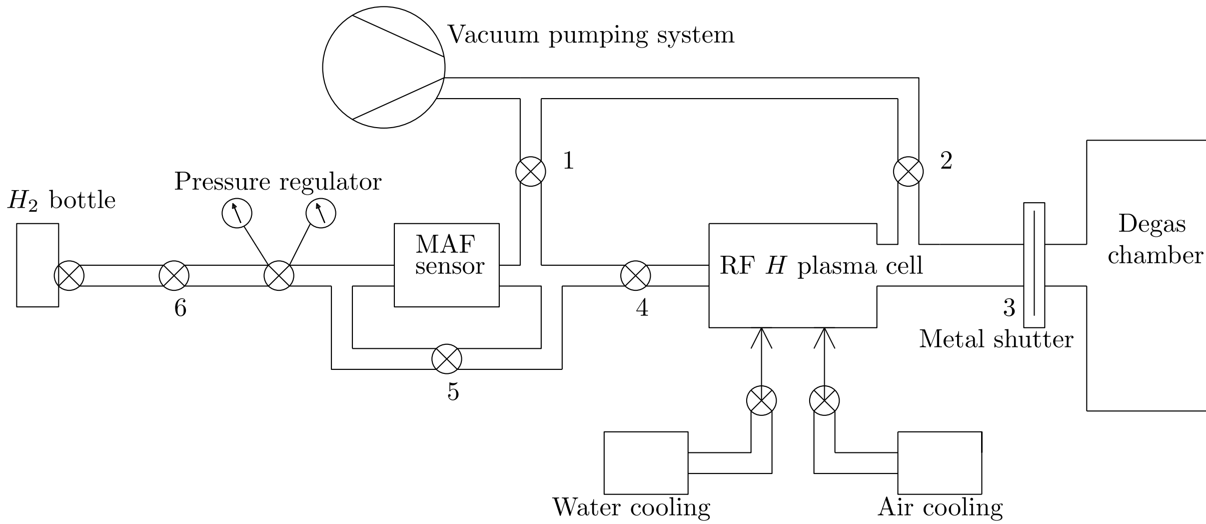

Figure 2.4: Radio Frequency H plasma cell schematic.

Because of the absence of a characterization tool for the plasma, for example to know the ionization percentage or the ions mean energy, an investigation was carried out through the measure of its emitted light intensity. Three kind of analysis were done:

- The H flux and the supplied RF power were fixed to check if plasma was stable in time.

What was found is that the plasma luminosity drops exponentially to a stable value:

$$I(t) = A \cdot exp(-\frac{t}{\tau}) + I_{EQ} \tag{2.1}$$

This is caused by two factors: the progressive increase of cell temperature, that after a transient tends to be constant and the degradation of the RF cavity. The previous point is suggested by the fact that if an external fan is used to slow down the cell heating, the plasma luminosity drop is slower and, if the cell is cooled after being heated, the luminosity increases while the temperature decreases. Instead, the latter point is a consequence of the observation that the longer the cavity has been pumped, the higher is the plasma luminosity at ignition instant. This has been related to the fact that the lower is the cavity starting pressure the cleaner it is. More probably a combination of both effects causes the observed drop but with a prevalence of the heating effect. The results of these tries are reported in Fig. 2.5a. It has to be said that the data series are not easily comparable because of the many changes that happened to the apparatus during the time that was needed to collect them all. Despite of this, what has been concluded is that using a too high power is not efficient because, even if at the start the plasma luminosity is higher, the cell temperature increases so much that the following luminosity drop is bigger than the luminosity gained from power increase.

- In another test the supplied RF power was fixed and the H flux was changed in a loop both to investigate the dependence from flux magnitude and to check if there is an hysteresis related to the flux itself. What has been found can be clearly seen from Fig. 2.5b: the dependence luminosity-flux is almost linear and the hysteresis is negligible or really small either if the external fan is turned ON or OFF.
- Lastly, a try was done keeping the flux constant and varying the supplied RF power in three loops. The hysteresis found, see Fig. 2.5c, can easily be related to the already explained hysteresis in time. Instead the relation between luminosity and supplied power is approximately linear.

It has to be noticed that the emitted light intensity can not be taken as a perfect reference for calibration of plasma because the optic sensor is externally mounted and, if it is moved, or unmounted for other purposes, the measures are not anymore perfectly reproducible. Moreover, some changes have been done to the apparatus during the activity and the time the RF cavity has been pumped has an influence on the starting luminosity of the plasma. Taking in to account

all these small but important differences, what has been done is to perform all the treatments with a H_2 flux of $2\,SCCM$, RF power of $250\,W$ and time duration of one hour. If any different parameters are used, it will be clearly specified in the following.

Finally, it is worth noting that during the treatment the reflected power in the cavity increases due to its thermal expansion, thus, to keep the supplied power constant, the reflected component was kept null by continuously modifying the cavity geometry.

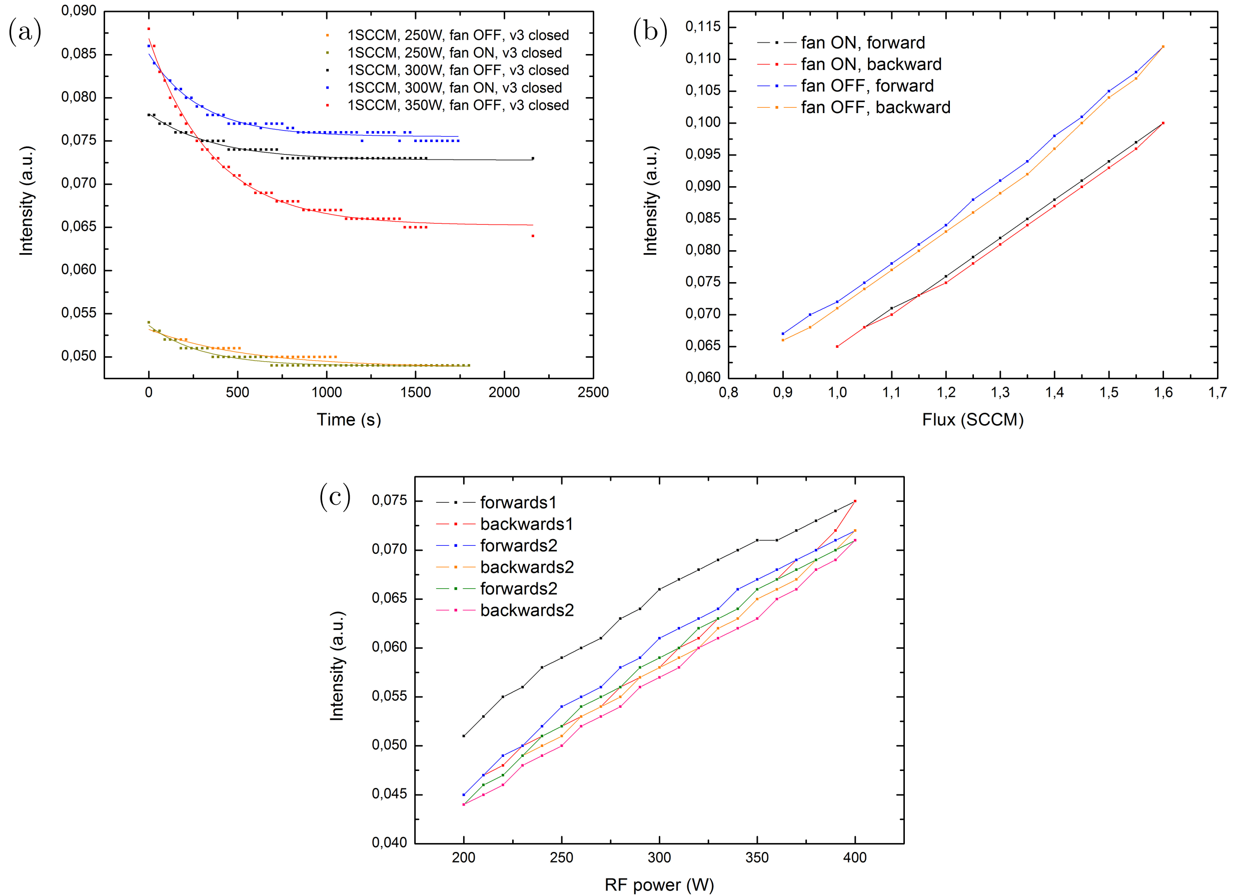

Figure 2.5: (a) Plasma luminosity intensity *vs* time for different radiation power and external fan turned off or on.
(b) Plasma luminosity intensity *vs* flux at $300\,W$ in two different cycles. Every point is take from the previous after 30 seconds.
(c) Plasma luminosity intensity *vs* RF power at $1\,SCCM$. Three cycles in the same run, with all the backwards always under the respective forward. Every point is take from the previous after 30 seconds.
Series in graph (a) and (b) are not comparable due to maintenance service that has changed the intensity detected. Otherwise looking at this graph it would seem that with fan turned on the plasma luminosity would decrease, while it has been seen clearly that it is the opposite.

2.2 Electron Microscopy

Electron microscopes are commonly used as the main characterization tools to look at the structural properties of NWs. As the name suggests, the beam that probes the sample is not made by light, as in normal optical microscopes, but it is made by electrons. This approach is necessary when looking at the nanometer scale because of the intrinsic resolution limit given by the wavelength: in an ideal case, it is possible to distinguish between two points only if they are separated by more than half of the wavelength of the probing wave. Because light in the visible spectrum has a wavelength in the range $400 - 700\,nm$, it poses a resolution limit around few hundreds nanometers. Instead, the wavelength of a massive particle is related to its energy by:

$$\lambda = \frac{h}{\sqrt{2mE}}$$

where h is the Planck constant, m the particle mass and E its energy. Thus increasing the energy of the particle beam would decrease the wavelength, and so increase the resolution. For exemple, considering an electron beam with $10\,keV$ energy, the related wavelength would be $12\,pm$. However, because of intrinsic aberrations in the microscope lens system, the actual resolution is several order of magnitude higher than this and only in advanced equipment, with specialized methods, it reaches the Angstrom scale.

When the electron beam interacts with the surface, a radiation composed both by electrons and X-rays emerges as schematically shown in Fig. 2.6. Each of these signals carries different information about the substrate and specific tools and techniques are required to analyze them. In particular, the Scanning Electron Microscope (SEM) generates images of the specimen by detecting the electrons scattered above the surface, like backscattered and secondary electrons. Instead, Transmission Electron Microscope (TEM) generates images using the transmitted electrons that may undergo elastic or inelastic scattering. Of course, there is a transmitted electron signal only if the probed sample is thin enough (order of $100\,nm$), thus specific preparation methods are applied according to what has to be investigated. Moreover, TEMs are normally equipped with a Energy Dispersive X-Ray system (EDX) that analyzes the emerging characteristic X-rays. If the X-ray acquisition is ran in STEM mode a map of the chemical composition of the sample is obtained.

In this work both SEM and TEM have been used: SEM is used to easily investigate the morphology (shape, dimensions, section., etc) and distribution of NWs; TEM is used to investigate crystal phase, crystal composition and growth direction of NWs, but also to look for defects and

check the abruptness of the interface between the NWs and the substrate. In the following we will briefly present the main characteristics of such microscopes, with attention also to the EDX working mechanisms.

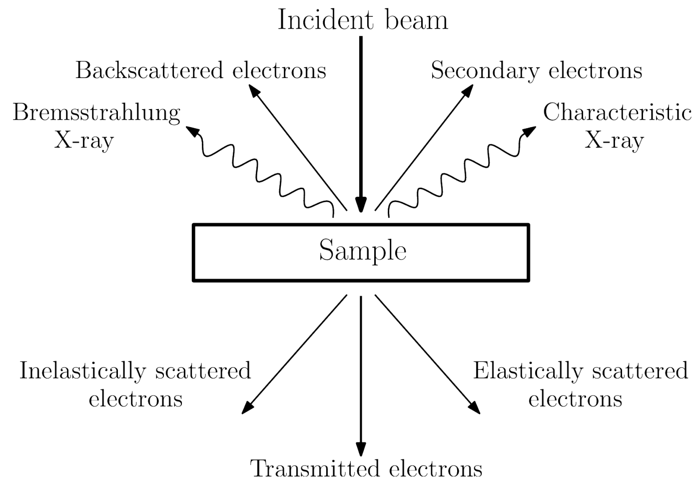

Figure 2.6: Main components in the outcoming radiation after interaction of a high energy electron beam with matter.

2.2.1 Scanning Electron Microscope

In a typical SEM, of which a schematic can be seen in Fig. 2.7, an electron beam is generated by field emission effect from a cathode (shaped as a small tip) and it is accelerated towards an annular anode by a negative potential of $1 - 30\,kV$.

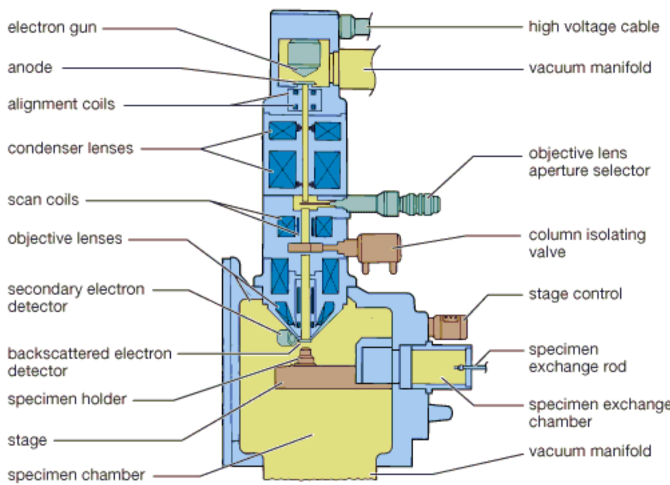

Figure 2.7: Schematic of the typical SEM setup.

Then the beam is aligned by specific coils at the center of a complex electro-magnetic lens column: a first system of lenses condensates the beam to a narrow diameter of few nanometers; after, a second system of lenses, called objective lenses, takes care of the magnification, focus and aberrations correction. Between these two sets, a couple of coils has the key role to quickly move in a raster way the beam, thus the specimen is scanned pixel by pixel. Different types of detectors collect respectively secondary electrons and backscattered electrons produced by the beam-sample interaction. An analysis system, triggered with the scan speed, brings to the for-

mation of an image using the amplitude of the collected signals. The full system is kept under high vacuum by a turbo-molecular pump in order to have electrons reach the surface without being obstructed.

With its working principle, it is clear that the SEM resolution is not limited by the wavelength of the incident electrons, instead it is mainly related both to the properties of the incident beam and to the nature of electron-matter interaction. Regarding the incident beam properties, its diameter is the most important factor limiting the resolution[2]. In particular, beam size depends partially on the source but mainly to three aberrations:

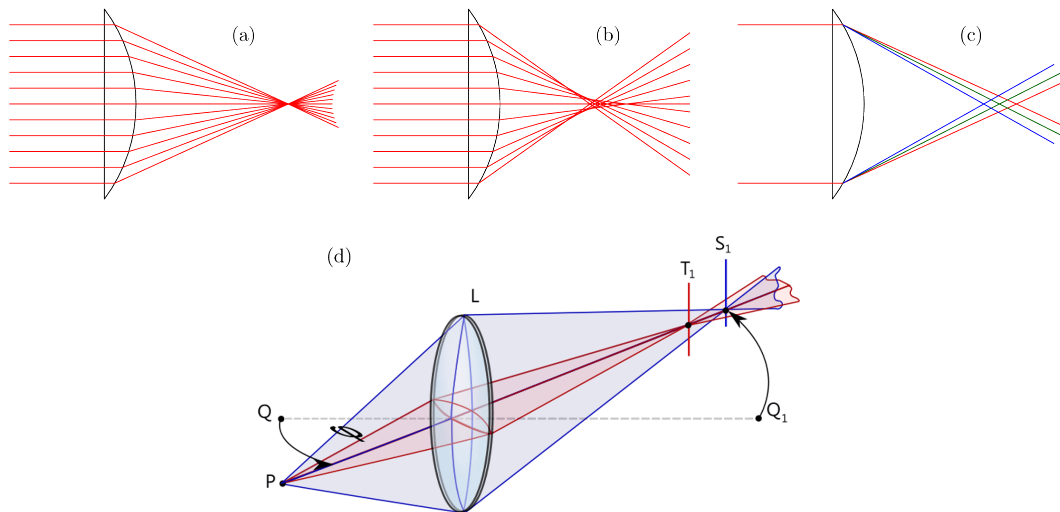

Figure 2.8: Aberrations schematic: (a) ideal lens; (b) sperical aberration; (c) chromatic aberration; (d) astigmatism.

- *Spherical aberration* (Fig. 2.8 b) occurs when the lens field behaves differently for off-axis rays. The further off the axis the electron is, the more strongly it is bent back towards it. As a result, a point object is imaged as a disk of finite size and this limits our ability to magnify because the detail is degraded by the imaging process. The "spherical" name comes from the fact that in normal optics spherical lenses are commonly used because they are easier to fabricate even if they are not the ideal lens. In principle this aberration can not be corrected and it is an intrinsic feature of the lens.

- *Chromatic aberration* (Fig. 2.8 c) occurs if the electrons in the beam are not perfectly mono-energetic. Because the beam has an energy distribution, there is always a small spread in the energy and this causes the electrons to respond differently to the lenses field. The "chromatic" name comes from the fact the energy spread corresponds to a wavelength

[2]Actually the beam has a spatial intensity distribution that for simplicity can be reduced to consider only its diameter because the dimensions in the running.

spread, and in the visible light spectrum we associate colors to each wavelength. It has to be said that with modern electron source, such as cold Field Emission Gun, this aberration is totally negligible compared to the others ($\Delta E < 1\, eV$ over $\sim 10\, KeV$).

- *Astigmatism* (Fig. 2.8 d) occurs when the electrons interact with a non-uniform magnetic field as they spiral around the optic axis. This can be caused by several small factors like non perfectly cylindrical lenses, micro-structural defects in the lenses material, charging or contamination of surfaces and many others. Fortunately, astigmatism is easily corrected using stigmators, which are small octupoles that introduce a compensating field to balance the inhomogeneities.

In second place, affecting the SEM resolution, there is the nature of electron-matter interaction: the electrons interact not only at the immediate surface of the sample but penetrate down to a depth that depends on the electron energy and the sample material. The overall result is a pear shaped interaction volume from which both backscattered and secondary electrons emerge. Therefore, the measured result is always an average of the signal that reaches the detectors from this volume. In the end, the resolution of a typical SEM, intended as the effective distance between two details that can experimentally been distinguished, varies from 1 to $20\, nm$ according to the instrument.

In this work of thesis two SEM have been used:

- Hitachi S-4800 equipped with a cold FEG (declared resolution of $1\, nm$ at $15\, kV$).
- FEI Helios Double Beam 600i equipped with a Schottky FEG (declared resolution of $0.9\, nm$ at $15\, kV$) and with a LMIS Gallium source to perform Focused Ion Beam processes.

Figure 2.9: Pictures of the the Hitachi S-4800 (left) and of the Helios 600i (right).

2.2.2 Transmission Electron Microscope

As already mentioned, because in TEM the electrons have to travel across the whole sample, special preparations are required to reduce sample thickness under 100 nm. The two procedures used in this work are described in Appendix B, instead here we will just briefly describe the working principle of a classic TEM and some of its signal manipulation modes.

The TEM can be considered as being composed of two strictly dependent parts, the illumination system above the sample and the imaging system under the sample. The illumination system is composed by a source, similar to the SEM ones, and a set of lenses, diaphragms and coils that allow to select between several working modes. For our purposes, we used only the *traditional TEM* techniques with a static beam (Fig. 2.10 a) and the *Scanning TEM* techniques (STEM) with a dynamic beam (Fig. 2.10 b). In the former the specimen is totally illuminated by a parallel beam of electrons whereas in the latter a convergent beam is moved across the surface. As in the SEM, in order to obtain a dynamic beam, four coils have the role to raster the sample by tilting and translating the beam itself.

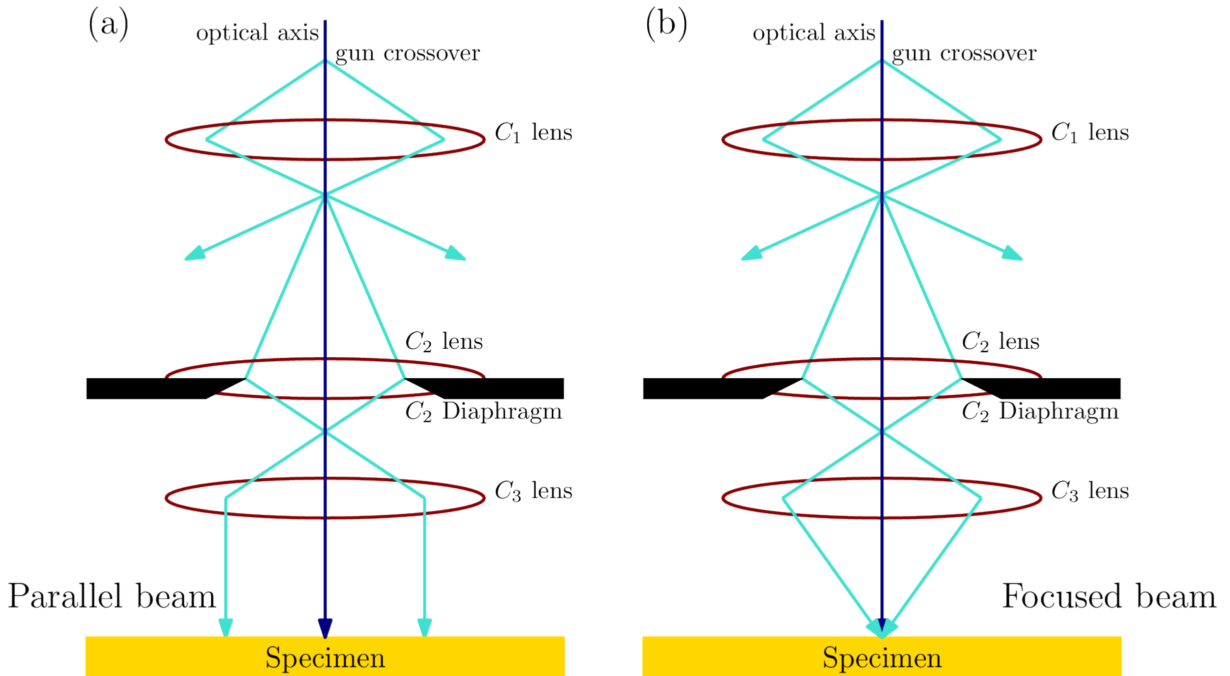

Figure 2.10: Schematic of possible lenses configuration to generate: (a) a parallel electron beam; (b) a focused electron beam.

The imaging system below the sample is composed by the objective, the intermediate and the projector lenses and several diaphragms that allow to switch between the possible imaging modes. As show in Fig.2.11, in the traditional TEM mode, by changing the strength of the

intermediate lens, it is possible to project on the screen a diffraction pattern or an image of the sample. More in detail:

- We are in *Diffraction mode* (Fig. 2.11 a) if the back focal plane of the objective lens acts as the object plane for the intermediate lens. Then a diffraction pattern (DP) is projected on the viewing screen/CCD camera. A Selected Area Diffraction aperture is usually inserted to reduce the investigated area from where DP forms.

- We are in *Imaging mode* (Fig. 2.11 b) if the intermediate lens is adjusted so that its object plane is the image plane of the objective lens. Then an image is projected on the viewing screen/CCD.

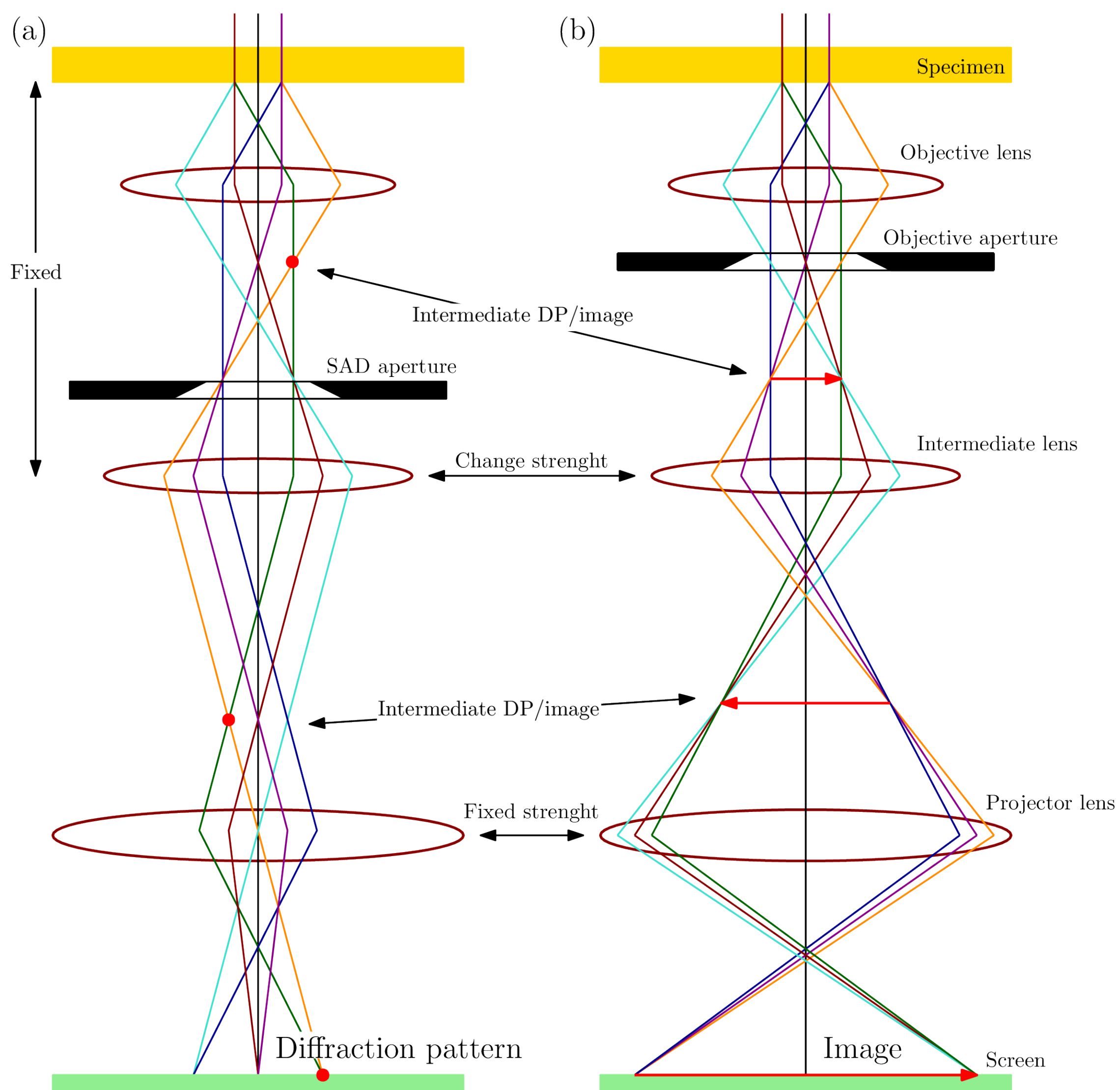

Figure 2.11: Schematic of possible lenses configuration to obtain: (a) a Diffraction Pattern; (b) an Image.

The *diffraction mode* covers a key role in all imaging modes because it allows to align the sample with the optical axis and to select which electrons are used to form an image. The alignment is done by rotating and tilting the sample while looking at the changes on the diffraction pattern. In fact, the diffraction pattern is the result of separation of the electrons in spots that are associated to the scattering from a well defined family of crystal planes in the sample. The brightest spot at the center of a DP corresponds to the direct unscattered beam, while all the other points are generated by diffracted electrons from a certain family of crystal planes. By inserting an objective aperture, it is possible to reduce the beam down to only a defined set of diffracted electrons which then form a peculiar image on the screen. According to the inserted objective aperture and the orientation of the sample, different imaging modes are defined:

- A *Bright Field* (BF, Fig. 2.12 a) image is formed if a small objective aperture is used to select only the directly transmitted beam.
- A *Dark Field* (DF, Fig. 2.12 b) image is formed if the small objective aperture is used to select only one of the spots formed by scattered electrons.
- In a *High Resolution TEM* (HRTEM, Fig. 2.12 c) image no objective aperture is used so that all the diffracted beams interfere in the screen creating lattice fringes that are a phase-contrast image of the sample with a high resolution that can reach sub-angstrom scale.

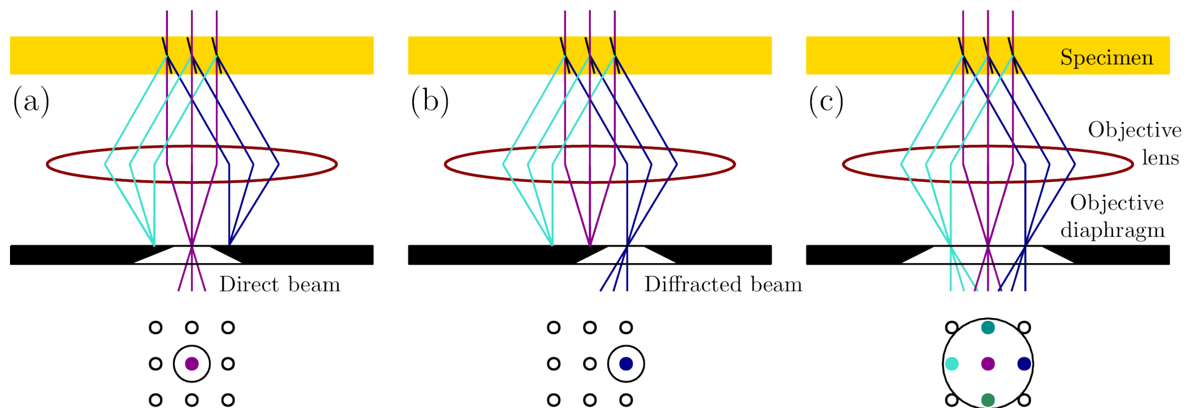

Figure 2.12: Three possible imaging methods in traditional TEM according to objective diaphragm position: (a) Bright Field with direct beam; (b) Dark Field with single diffracted beam; (c) High Resolution with multi-beams.

Several imaging techniques are also available in STEM mode. They are differentiated according to the detector type and position[3]. Without going too much in details we will just list the

[3]Actually the detector position is never changed. It is enough to change the angle at which electrons impinge

most common configurations used to perform STEM images:

- *Bright Field STEM* is obtained using the transmitted beam and a small detector centered with the optic axis. The image formation is based on the same principle as in SEM: as the beam rasters the surface, an image is slowly acquired pixel by pixel using only the transmitted beam. If the beam encounters an atom, it is deviated, thus the corresponding pixel turns darker in the image.
- *Annular Dark Field* is obtained using an annular detector around the BF-STEM detector. The contrast in this mode is given by the fact that atoms with higher atomic number scatter electrons at higher angles.

Finally, nowadays, all TEM setups are equipped with an X-ray detector that is used to obtain Energy Dispersive X-ray spectra. With this spectra, as with every characteristic X-ray spectrum, it is possible to clearly identify the elements contained in the specimen. If the sample is illuminated with the parallel electron beam from the *traditional TEM*, a simple spectrum is obtained. Instead, if the acquisition is done while in STEM mode, a chemical map of the specimen is acquired. Indeed, once the pixel map is defined, a spectrum is acquired for each pixel while the raster scan is performed several times. The analysis of all these spectra with a quantification software allows to reconstruct a chemical map of the specimen.

It has to be said that TEM is affected by aberrations as SEM and even more perturbing effects have to be considered, however we will not discuss them in this work. More detailed information about TEM and all its working modes can be found in the comprehensive guide "Transmission Electron Microscopy" by D. B. Williams and C. B. Carter. In this thesis two TEM setup have been used: JEOL JEM-2100F with a declared resolution of 2.3 Å at 200 kV and a JEOL JEM-ARM200F with a decleared resolution of less than 1.9 Å at 200 kV.

on in to have a result that emulates the distance change between it and the sample.

2.3 Ellipsometry

Ellipsometry is a powerful optical technique for characterizing thin film materials and surfaces. It is used to investigate their optical constant, film thickness (of single or multiple layers), doping concentration, roughness, crystallinity and other physical quantities with sub-monolayer resolution. Actually, ellipsometry only probes how the polarization of an incident light changes after the interaction with a surface. Then specific models, based on a partial knowledge of the sample, have to be used to extract the sought information from the acquired data.

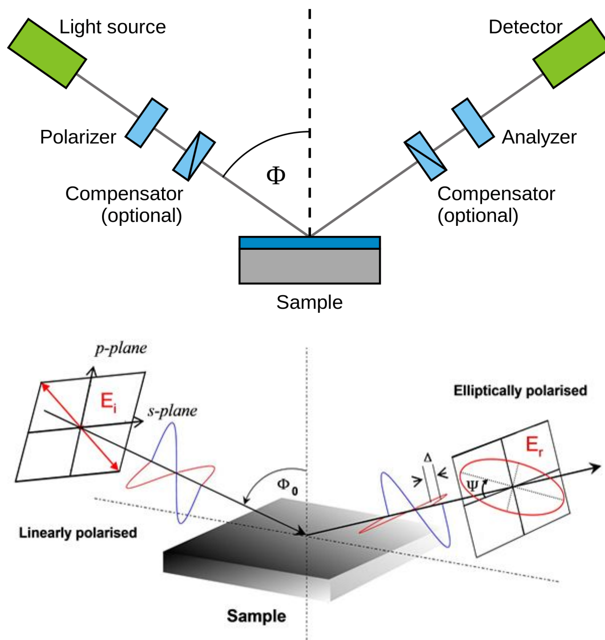

Figure 2.13: On top the schematic of a typical ellipsometer apparatus; on bottom the state of the wave before and after the interaction with the surface. In bottom figure it's possible to see the relation of Ψ and Δ with the ellipse.

More in details, in a spectroscopic ellipsometer (Fig. 2.13), a light source emits an unpolarized beam that usually spans from infrared to ultraviolet. The emitted light beam is linearly polarized (by passing through a polarizer) and then it interacts with the sample surface. The reflected beam has an elliptical polarization that is analyzed combining a continuously rotating polarizer, namely the analyzer, and a detector. With this setup, the light beam is converted in an electric signal from which the full ellipsoidal behavior of polarization can be recorded. In the spectroscopic ellipsometer the acquired data are a couple of spectrum that describes how the polarization changes at different wavelength. Indeed, the light signal can be considered composed by two components, one parallel and one perpendicular to the sample surface. Their amplitude ratio Ψ and their phase difference Δ are related to the complex perpendicular and parallel reflex coefficients, $\tilde{r}_p$ and $\tilde{r}_s$, respectively, by the relations:

$$\rho = \frac{\tilde{r}_p}{\tilde{r}_s} = \left|\frac{r_p}{r_s}\right| e^{i(\delta_{rs}-\delta_{rp})} = \tan\Psi e^{i\Delta}$$

$$\tan(\Psi) = \left|\frac{r_p}{r_s}\right| \qquad \text{and} \qquad \Delta = \delta_{rs} - \delta_{rp}$$

As previously explained, the spectra of the two angles Δ and Ψ are fitted with specific models

to indirectly find unknown characteristics of the sample. In our case we are interested only in the measurement of the thickness of a small layer of silicon oxide on a silicon substrate. The model to solve this problem is well know and can be found elsewhere [33], however it is useful to know that the model is based on nine parameters. These are the real and imaginary part of the complex refractive index $\tilde{n}_{air}$, $\tilde{n}_{film}$, $\tilde{n}_{substrate}$, the beam angle of incidence θ, the light wavelength λ and the film thickness d. Using the tabulated data for the refractive indexes, only the film thickness remains as a free parameter. Because the final equation is transcendent, an iterative fitting routine based on χ^2 minimization is used. As result, only one value of d, with the associated error and reduced χ^2, is obtained.

2.4 Atomic Force Microscope

Atomic Force Microscopy is a widely used technique to characterize surface morphology by realizing high resolution images with an atomic precision. As can be seen from Fig. 2.14, an AFM utilizes a cantilever with a sharp tip mounted at its extremity to probe the surface. This tip, made of silicon or silicon nitride, is like an atomic needle that transfers a force to the cantilever proportional to its distance from the surface. In order to monitor and calibrate the cantilever deflection, we have used the optical lever method which combines a laser and a quadrant photodiode. Moreover a piezoelectric scanner move the tip around the surface in an accurate pattern; in this way a digital system creates a map by associating at each probed spot the height measured by the cantilever.

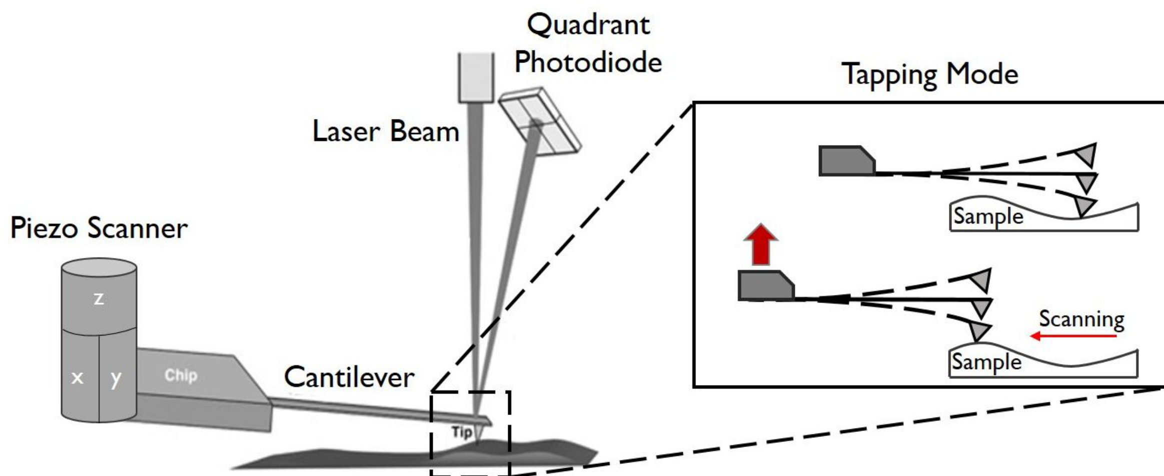

Figure 2.14: Schematic of a typical AFM.

Actually, in this work we have operated the AFM in tapping mode in which the tip is not kept in contact with the surface. Instead, the cantilever is oscillated at its resonance frequency with constant amplitude by a piezoelectric oscillator on the holder. If during the scan the surface gets further or closer, the oscillation amplitude changes due to tip-sample interactions. Therefore with a feedback system it is possible to adjust the vertical position of the cantilever so that the amplitude remains constant. The holder position, referred to the starting one, corresponds to the change in height of the surface.

The AFM operated in this work, a BRUKER Dimension Icon, with the employed tip and in tapping mode, has a pixel area resolution of $1\,nm$, whereas, the vertical resolution is below $0.3\,nm$ so that single atomic plane steps can clearly be seen.

Chapter 3

Growth on unpatterned Si(111) surface

In this chapter I will report about the influence of surface pre-treatments on the growth of *InAs* NWs over an unpatterned Si(111) substrate. The study of the influence of each MBE parameter (growth temperature, growth time and III-V fluxes) on the morphological properties of the NWs has already been carried out in details by other groups ([24],[25],[26]). However, it is important to underline that a systematic investigation of all the parameters is impossible due to their number and strong correlation. Indeed, what should be expected is that, with different surface treatments, the set of growth parameters giving the best NWs should change every time and the phase space should be scanned again and again. It is clear that this is way too long and expensive because of all the possibilities: HF treatment (yes or not = at least 2), plasma treatment (substrate temperature, H flux, RF power = at least 9), thermal annealing (different temperatures or not = at least 3), growth temperature (at least 3), III/V flux ratio (at least 3) and total flux (at least 3). With only this few adjustments, the possible combinations are around one thousand and many other possibilities and aspects are not being taken into account (as for example plasma processing time, growth duration time, HF type of rinsing, substrate pre-wetting *in-situ*, etc.). Having a limited amount of time and resources, the investigation has been carried out by interpreting the results of each recipe just after the end of its manipulation. Then the next recipes were decided thanks to feedback and ideas obtained by the previous ones so that also more then one parameter was changed at the same time.

This said, in the following I will not go through the space parameter scanning in details, but more attention will be given to the role of the applied surface pre-treatments. Then a full section will be dedicated to the structural and chemical characterization of the sample which had NWs with the best aspect ratio and density. In conclusion a section will be fully dedicated to the role of the H plasma treatment, being it the really innovative part of the treatments.

3.1 Surface treatments and growth parameters

The research of a good set of growing parameters has proceeded together with the combination of three main surface pre-treatments: *ex-situ* hydrofluoric acid etching (**HF**), low energy hydrogen plasma treatment (**H2**) and high temperature thermal annealing (**HT**)[1]. Along with this procedures, it is always mandatory to degas at low temperature the specimen before moving it inside the growth chamber. Actually, in the case the plasma treatment is used, the degasing is incorporated in the very same process because they are performed in the same chamber at the same time[2]. Eventually, a pre-wetting of the surface is often performed by evaporating In for $5\,min$ before starting the proper deposition. This is done in order to form droplets with which we believed that nucleation would have been easier.

One of the first result that we obtained is that applying a simple hydrofluoric acid etching is not enough to trigger the grow of NWs at all. The HF etching is the most used wet chemical cleaning procedure and we used it to remove the native oxide and any contaminants from the silicon surface. The applied routine is really standard: the specimen is immersed for $1\,min$ in a diluted bath of HF (5%), then rinsed for $30\,s$ two times in two different pots filled with deionized water (DIW) and finally dried with a pure air nitrogen stream. The result of this process for the silicon has been for long a source of debate, whether if the silicon were H-terminated or if it were F-terminated. Now several experiments and physical model totally confirm that the surface is H-terminated. This is really important because it grants that, during the time required to load the sample in high vacuum after the etching, the surface can not significantly re-oxidize, nor for the DIW rinsing, nor for the air all around. In Fig. 3.1 we can clearly see the difference between a sample where only HF has been applied (a) and one that still has the native oxide (b). These growths have been performed together, at the same time, with a triple wafer holder and the set parameters were $T_g = 525\,°C$, $V/III = 100$, $t = 1.5\,h$ with In pre-wetting. In the first sample we can see that no NWs are present but just random shapeless islands are formed with sizes from $10\,nm$ to $500\,nm$. Instead, in the second sample, where the oxide was not removed, few NWs with diameter around $60\,nm$ and length up to $1.5\,\mu m$ are present among many shapeless islands with diameter of $200\,nm$. As expected the NWs are not vertical nor following any preferential direction because in this case the growth is not epitaxially starting from the silicon crystal lattice.

[1] In this context *high temperature* and *low temperature* are referred in relation to the principle temperature in the process, i.e. the growth temperature. The thermal annealing is performed at a temperature $\sim 200\,°C$ higher than the growth one (around $750\,°C$), whereas the degasing is performed at $\sim 200\,°C$ less (around $500\,°C$).

[2] The sample is heated during the plasma treatment and we will report between bracket the relative temperature in Celsius degree.

Furthermore, it has to be noticed that the result of a deposition strongly depends on how the incoming adatoms interacts on the surface. The diffusion lengths and the adsorption rates of adatoms on each surface (silicon and silicon oxide) are different and this reflects on the grown structures and the amount of deposited material.

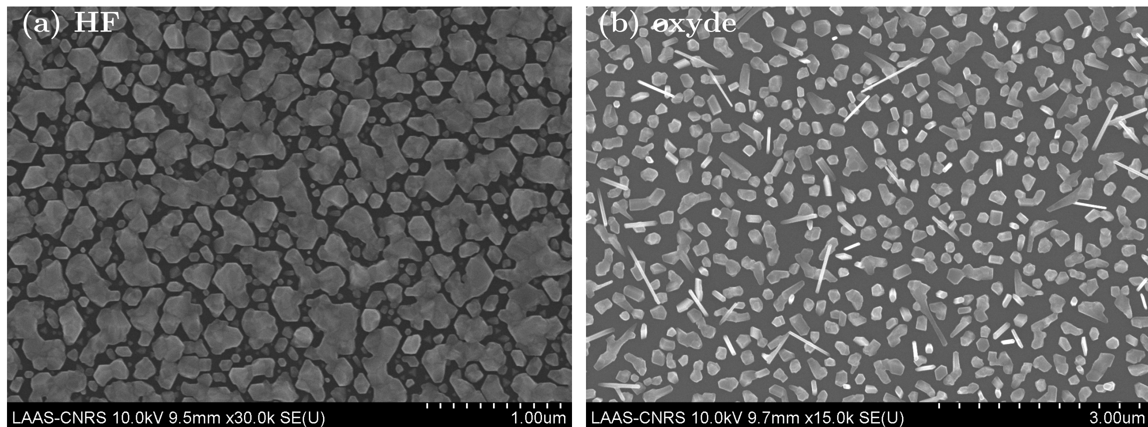

Figure 3.1: SEM top view of two sample grown together: (a) with simple HF treatment; (b) with native oxyde (not at same scale).

Also using only one treatment between plasma or thermal annealing does not give any better result towards vertical NWs. What happens in the case of a low energy hydrogen plasma treatment is shown in Fig. 3.2 (a). The surface is clean from any island but only few tilted NWs are present. As we will see later, the H plasma is not expected to have any etching effect on the silicon oxide, thus the tilt of the NWs has the same explanation as before. In comparison to the two specimen of Fig. 3.1, the growth recipe here is slightly changed by cutting to half the In flux, thus here the V/III is 200. This does not allow us to immediately conclude that the H plasma is reducing the amount of material that sticks to the oxided surface, however it is very unlikely that such a big change is related only to V/III ratio alteration. Indeed, a confirmation of this can be found in the specimen where only the high temperature annealing was applied with the same growth parameters. The performed annealing was a $20\,min$ treatment at $750\,^{\circ}C$ and the result of this recipe is shown in Fig. 3.2 (b). Although the growth parameters are the same, many islands are again visible and many non-vertical NWs are present. The situation is somewhat close to the sample with normal native oxide, and the increase in the aspect ratio of NWs, as well as the island dimension reduction, is probably related to V/III ratio modification. Indeed, a normal thermal annealing at only $750\,^{\circ}C$ is expected to have a very limited effect on the native oxide[3].

[3] According to Wang et al. in [23], the thermal annealing can open small holes on thin film of silicon oxide, however the reported temperature are slightly higher than $750\,^{\circ}C$

Overall we can already conclude that both the H plasma treatment and the thermal annealing do not remove the native oxide, thus only non vertical NWs are observed. However, at the same time, it is clear that both treatments have an effect on the diffusion length of the adatoms because of the different densities and dimensions of islands and NWs. To proceed further a combination of more than one technique is required and for sure the HF etching has always to be applied in order to trigger the sought epitaxial growth of vertical NWs.

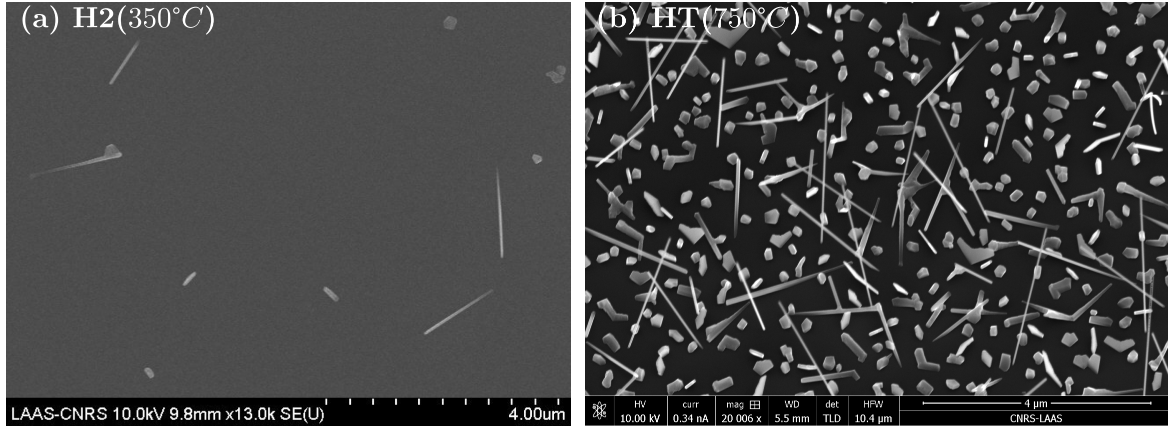

Figure 3.2: SEM top view of two sample with same recipe but different treatments: (a) with plasma treatment; (b) with thermal annealing.

Always with the same growth recipe ($T_g = 525\,°C$, V/III = 200, $BEP_{In} = 4 \cdot 10^{-4}\,Pa$, In droplet pre-deposition), the first positive results are obtained if the plasma treatment is applied after the HF etching. Some short and large but vertical NWs are formed as shown inFig. 3.3 (a). The surface, that can be supposed oxide-free due to the uprightness of NWs, presents less islands than the speciment with simple HF etching, however, still big crystalline islands are easily found. Again the H plasma treatment seems to heavily modify the sticking probability of the adatoms to the surface but also their diffusion lengths (change of grown structures). Instead, when the thermal annealing is applied after the HF etching, NWs with smaller diameters and higher density are grown (Fig. 3.3 (b)). In this case, both the diameters and the heights of the NWs change in a big range: the previous variation is strictly related to the In droplets diameter distribution, instead the former can be attributed both to the competitive collection of material from the surface and to the diameter itself.

Consequently, in both cases the epitaxy is successfully triggered and the best result is obtained for the thermal annealed specimen. Despite this, up to now the grown NWs are far from the objective of diameter around $20 - 30\,nm$. Indeed, in the HF+plasma specimen they have a diameter over $200\,nm$ while in the HF+annealing sample they largely spans in the $150 - 600\,nm$

range. To conclude the two pre-treatment combination, if plasma treatment and thermal annealing are combined, thin but still tilted NWs are obtained as show in Fig. 3.3 (c). Of course this is expected because the deposition is taking place with the native oxide still intact.

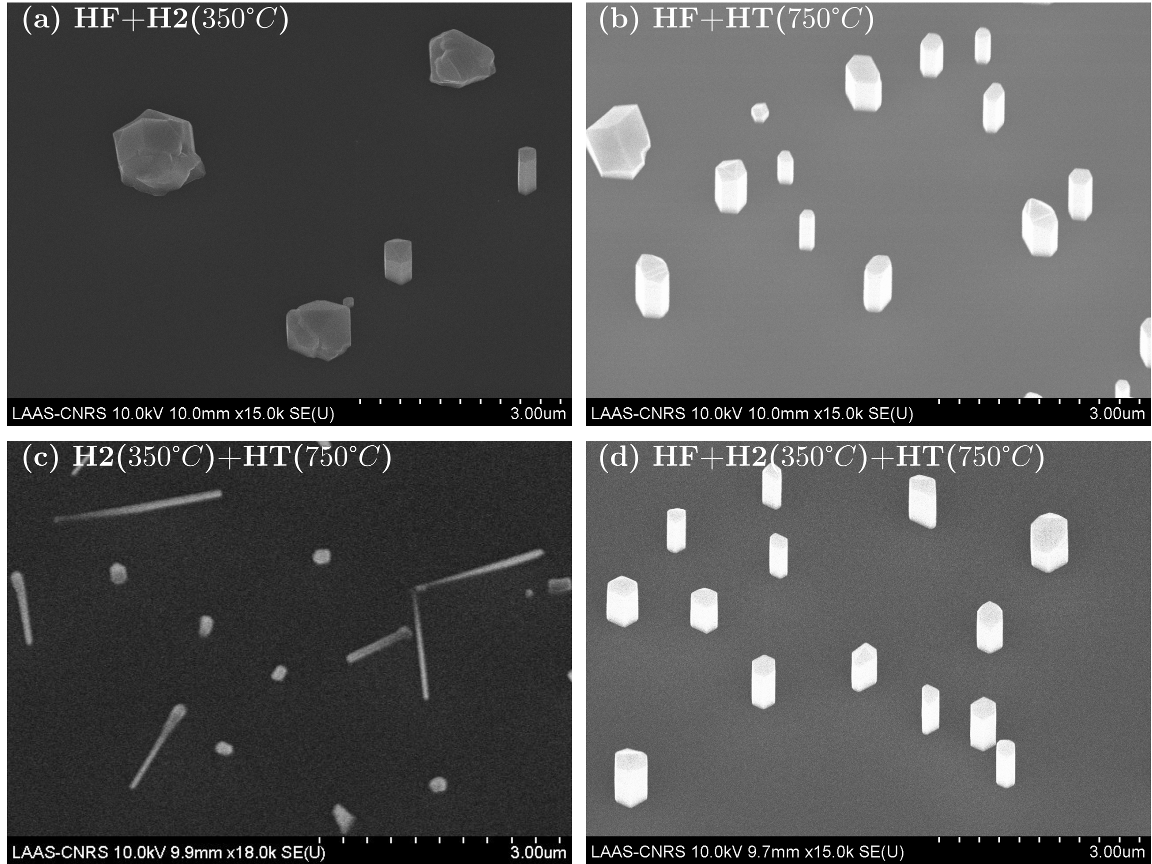

Figure 3.3: SEM tilted view of three sample with same recipe ($T_g = 525\,°C$, V/III = 200, $BEP_{In} = 4 \cdot 10^{-4}\,Pa$, In droplet pre-deposition) but different treatments: (a) with HF + plasma treatment; (b) with HF + thermal annealing; (c) with plasma treatment + thermal annealing; (d) with HF + plasma treatment + thermal annealing.

The best result in terms of surface cleanliness and NWs uprightness is obtained combining all three pre-treatments. The outcome, always using the same growth parameters and In droplets pre-deposition, is shown in Fig. 3.3 (d). At first glance the result seems so close to the one with only HF and thermal annealing that is licit to inquire if the H plasma is having any effect at all; or better, if applying the high temperature annealing after the H plasma exposure is removing the influence of the previous treatment. To give an answer to this question a specific series of samples has been grown and the related investigation is reported in Section 3.3.

Now the role of each pre-treatment is quite, but not totally, clear and the necessity to combine all of them is experimentally evident. At the same time, it is true that the growth parameters are not optimized case by case and that they have been only slightly explored in their possible

ranges. Despite of this, we realized that growing only short and large NWs is not caused by the chosen growth parameters but by the pre-deposited In droplets. Indeed, what is obtained after removing them is shown in the images of Fig. 3.4: the NWs density spikes to $10\,NWs/\mu^2$ while their diameter shrinks to $20-35\,nm$. Although this two good achievements, several islands are still crowding the surface and, due to material competitive collection, they are limiting the number of NWs growing around them. Moreover, there is still a big issue for NWs applications: with the *catalyst free* process no control is held on the time at which a NW growth starts, thus the length of the NWs varies from few decades of nanometers to over one micrometer. This partially affects also their diameter that varies between $20\,nm$ and $100\,nm$ and such a big variation would be detrimental for devices applications.

Because we were quite satisfied with this last sample results in term of NWs diameter, uprightness and density, it has been analyzed more in depth to characterize structural and chemical properties of its NWs.

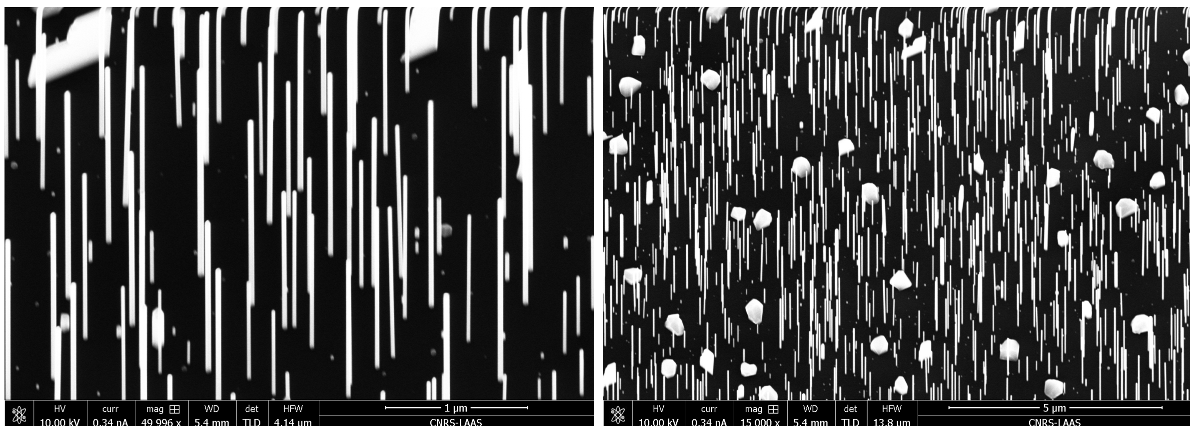

Figure 3.4: SEM tilted view of the best unpatterned sample: HF etching + Plasma treatment + Thermal annealing and $T_g = 525\,°C$, V/III = 300, no In droplets.

3.2 TEM and EDX characterization of the best NWs

The TEM investigation has been carried out using both the preparations described in Appendix B. With the holey carbon grid method we find out that at the base and at the top of the NWs the crystal phase is not the same. As can be seen from Fig. 3.5, at the base of the NW the crystal phase is purely Zincblende (left image), whereas at the top there is an alternation of Zincblende and Wurtizite phases (right image). This conclusion comes from the analysis of the atom patterns: when looking from the <110> direction, it is possible to distinguish between the ABCABC stacking of the ZB phase and the ABAB stacking of the WZ phase. Also, the NW

growth direction is confirmed to be along the <111> because the NW axis is perpendicular both to <110> and <112> directions. The switch between the two regimes happens gradually along the length of the NW and several stacking faults and twin planes make difficult to establish a precise turning point. The physical reason behind this phenomena is found in the different diffusion length of In and As and on their adsorption rate. Indeed, the most validated model predicts that the materials that contribute to the growth change during the process: at the beginning the material collection takes place only from the surface and thus depends on adatoms diffusion on it; instead, once the NWs grows, an always increasing contribution is given by the material collected from the NWs facets and here the adsorption rates and diffusion lengths are different. Of course the phases alternation is mainly possible because the energy discrepancy between the two crystal structures is small enough to be influenced by such phenomena.

Moreover, from Fig. 3.5 we can notice the presence of an amorphous material all around the NW that, as we will see, is the native oxide. Finally, we can confirm that the NW diameter is around $20\,nm$.

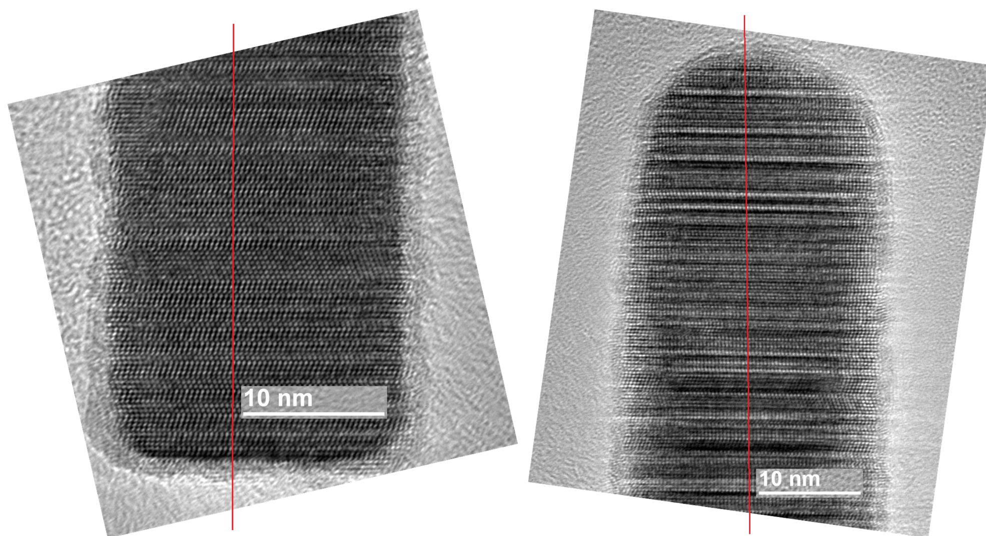

Figure 3.5: High Resolution TEM images of NWs scratched from best sample: left image the base, right image the top termination. The red line is just to guide the eye across the visible crystal bi-planes.

The FIB lamella preparation (see Appendix B) has been used on the very same sample in order to study the interface of the NWs with the substrate and to obtain their chemical composition map via EDX. However, few particular notions have to be pointed out on this preparation because the used procedure was not perfectly conventional: in order to do the sample carbon coating, an external evaporator has been used because a huge amount of carbon was required to fully surround the long NWs (and this would have required too much time using only the FIB

e-beam). In the process, the carbon deposition was not perfectly homogeneous and this induced a strain on NWs that, compared to how they appeared in Fig. 3.4, were bent, as it can be seen in Fig. 3.6. Moreover, two opposite factors contributed to the lamella sharpening: on one hand, to obtain a TEM image with low background noise, the lamella has to be sharpened down to as much as possible; on the other had, with our NWs density and taking into consideration that their position is random, the probability of obtaining more than one NW fully inside a small section was quite low. This said, it was necessary for the operator to make the sharpening while looking for possible interesting observation spots. The result is shown in the right image of Fig. 3.6 where we can see that part of the shielding Pt film collapsed and also that some holes are present inside the carbon deposition because of NWs shadowing. Despite all this, in both the two extracted lamella there where more than two observable NWs[4].

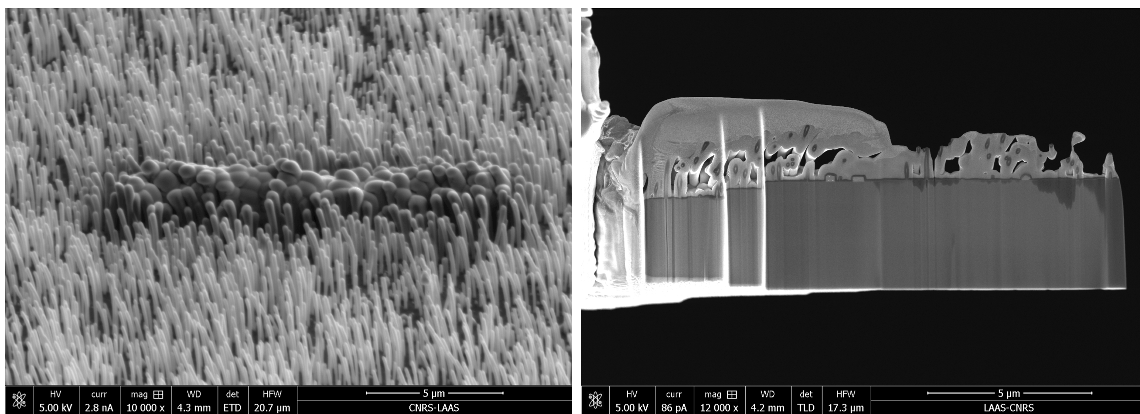

Figure 3.6: On the left, SEM image during Pt deposition that shows how the NWs had became bent during the previous carbon coating. On the right, SEM image of the lamella after the sharpening step.

An example of how NWs look inside the FIB lamella is reported in Fig. 3.7 (TEM high resolution mode). In the left image we can see how the NW is well coated with carbon (white halo around the NW) and that its thickness is not homogeneous around the NW so that a bending stress was induced. In the magnified image we can see a thin grey film over the silicon substrate that actually is the native oxide that formed after exposing the sample to air once the epitaxy had been finished. What might seem strange is that, from this image, the NW appears to be "attached" to the oxide and not directly to the silicon substrate. As we will see later this is just an artifact due to the fact that electrons are passing through a thickness around $100\,nm$ while the NWs have a diameter of only $20\,nm$. In other words this means that there are around $80\,nm$ of silicon oxide contributing to the image in the very same zone where the NW interface

[4]We had to make two lamella because the first had been taken along the wrong <112> direction due to inattention at the moment its manufacturing was ordered.

with the silicon is located. Moreover, from this image we can see a circular white shadow in the Si under the NW and a black shadow stripe on the very top of the surface. The first is an indication that a strain is induced in the Si by the presence of the NW, whereas the latter is a Fresnel fringe.

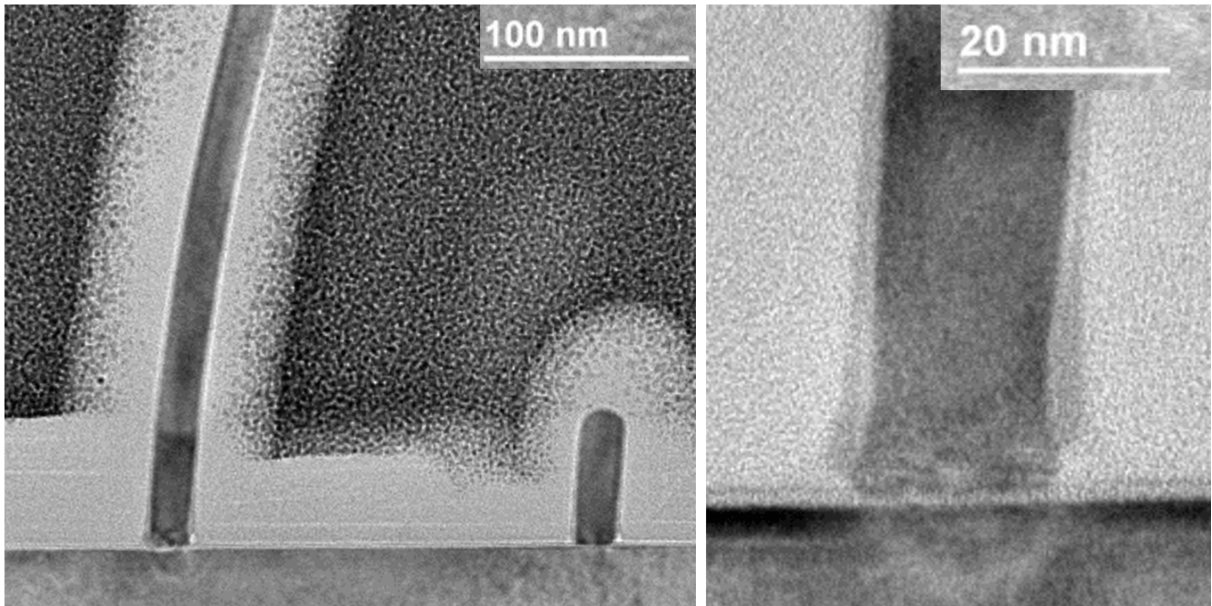

Figure 3.7: Global TEM images of NWs inside the <112> oriented lamella.

A more close look at the interface characteristics is given by the High Resolution TEM image reported in Fig. 3.8. The picture is taken at the base of the long NW and we can immediately notice how its crystal planes are tilted in comparison to the substrate ones (green lines). If the tilt has not been caused by the carbon deposition induced strain, a relationship must exist with the dislocations and defects that are present in this zone. For example, dislocations are probably present in this zone, as highlighted by the two yellow lines on the magnified image. These defects might therefore be then the ultimate consequence of the lattice mismatch between $InAs$ and Si. Indeed they are not observed on the upper parts of the NW: beyond $2\,nm$ from the base, only twin planes, stacking fault and crystal phase changes can be found, but no dislocations. Furthermore, all the crystal planes piling up from the Si substrate to the $InAs$ NW can be identified (i.e. without any “gap”), proving that the oxide had been totally removed before the deposition and that the epitaxy takes place starting from the silicon substrate. At this point, it is worth noting that what have been called crystal planes up to now are actually bi-layers formed by two following monolayers and that each white “point” on these images is not a single atom but a pair of them.

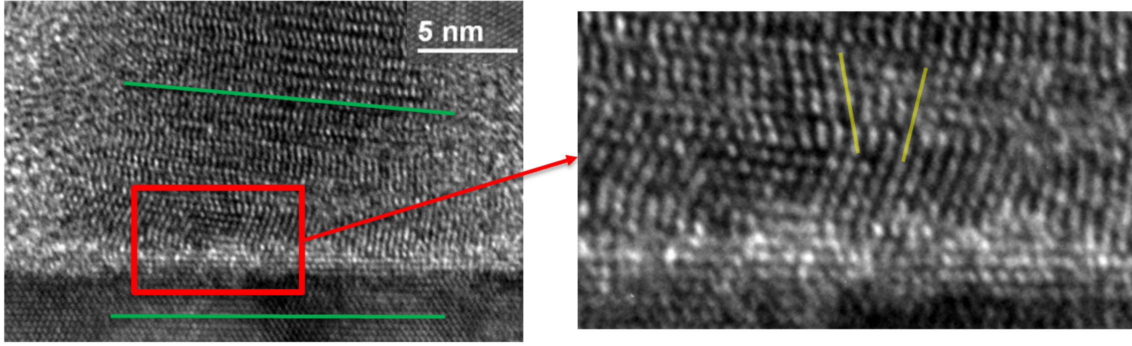

Figure 3.8: High Resolution TEM images of NW base and interface with silicon substrate.

To resolve the single atoms, some pictures were taken in STEM mode with the Jeol ARM200f microscope. We recollect that, in this mode, the image is not generated by a phase contrast interference as in HRTEM mode, but each image pixel corresponds to a singly illuminated small spot on the sample that can deviate or not the beam. In the *dark field* mode, a white pixel is recorded if the beam is deflected by the electron-matter interaction and it is the brighter the heavier the targeted atom is. Instead, the opposite happens for the *bright field* mode where atoms appear as dark spots[5]. Even if the STEM technique is much harder to perform, single atom rows can clearly be distinguished as shown in Fig. 3.9. To obtain images of this quality, the sample has been cleaned with a low energy argon-hydrogen plasma prior to being inserted in the TEM and then it was irradiated with a defocused electron beam for $20\,min$[6]. The images reported hereby are from the lamella oriented in the <110> direction (the correct one to see ZB-WZ differences) because the previous one was irradiated to much during other imaging sessions, thus NWs are different but belong to the very same sample.

From 3.9, we find again confirmation that the NWs are epitaxially growing from the Si substrate througthout the entire NW section (i.e. growth does not occur only from some holes opened in the native silicon oxide). This confirms that the surface has been completely cleaned and does not reoxide before growth. Moreover, the resolution is pushed to such an extent that In and As rows can be recognized from their atomic number (Z): the smaller dots are associated to the As rows, whereas the bigger ones to the In rows. Simply from this, we can see that the In planes are always under the paired As one, so $InAs$ NWs grow vertically along the (111)B on Si(111) (as proposed in [3]). Unfortunately, at the interface the image becomes once again blurred due to the influence of the silicon oxide all around the NW. Therefore it is impossible,

[5] The two images are not the perfect negative one another, but the distinction is made by the used detectors and so on the type of detected atoms (scattered or non scattered).

[6] This procedure, called "beam shower", is used to reduce the contamination of the sample during high magnification imaging.

from these images, to determine if the NW starts the nucleation with an As or an In plane. Finally, in this images we can not find any dislocation but only twin planes, suggesting that the previously observed dislocations on long NWs are consequence of the strain induced from the heterogeneous carbon deposition.

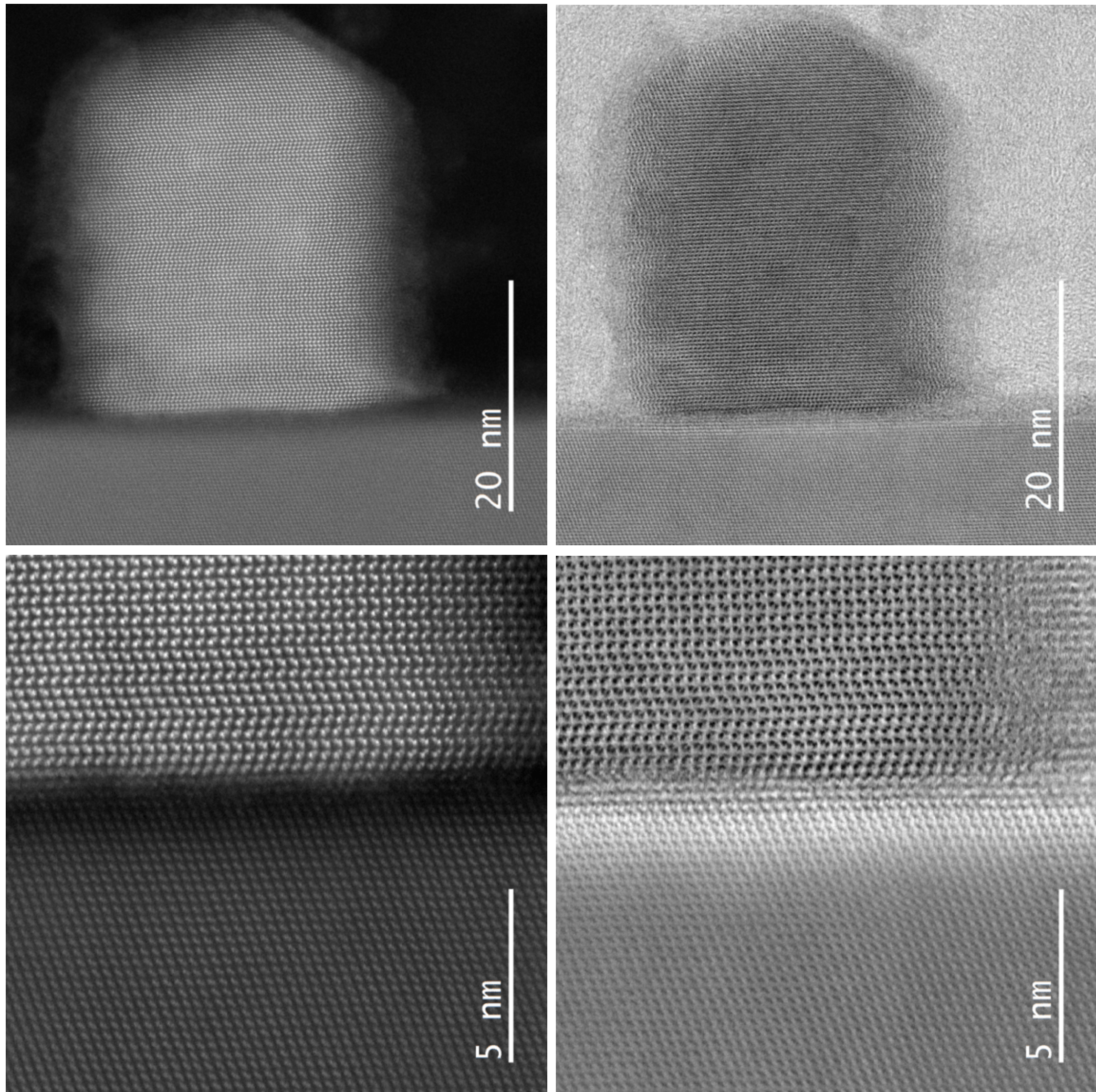

Figure 3.9: STEM images from bright and dark field detectors. First global image of a NW from sample in <110> direction, then magnification at the bottom right border of its base.

In order to answer to this question and to confirm the oxide nature of the thin grey film all around the NW, an EDX analysis has been performed. For such investigation, we wisely chose to go back to the lamella with the <112> orientation. This was done because the NWs have an hexagonal shape with facets defined by <110> planes, thus, if the <112> direction is chosen, the borders of the NW are more defined in the TEM projected image and a thicker layer of

the surrounding oxide can be analyzed. The EDX acquisition was run in STEM mode so that a chemical composition map of the sample could be obtained. For this purpose the resolution, namely the pixel dimension, had to be fixed to $1\,nm^2$ because a sufficient statistic has to be acquired in a relatively short time ($5\,min$). Indeed, if a smaller pixel dimension were to be chosen, the recording time would have to be increased. At the same time this would have caused an extreme exposure of the sample, bringing to accumulation of damage and charges which then would have degraded the effective resolution[7].

A first EDX map has been taken near the edge of the long NW base. Then, specific areas of the acquired map were integrated and the resulting spectra were quantified with a dedicated software as shown in the following images and tables:

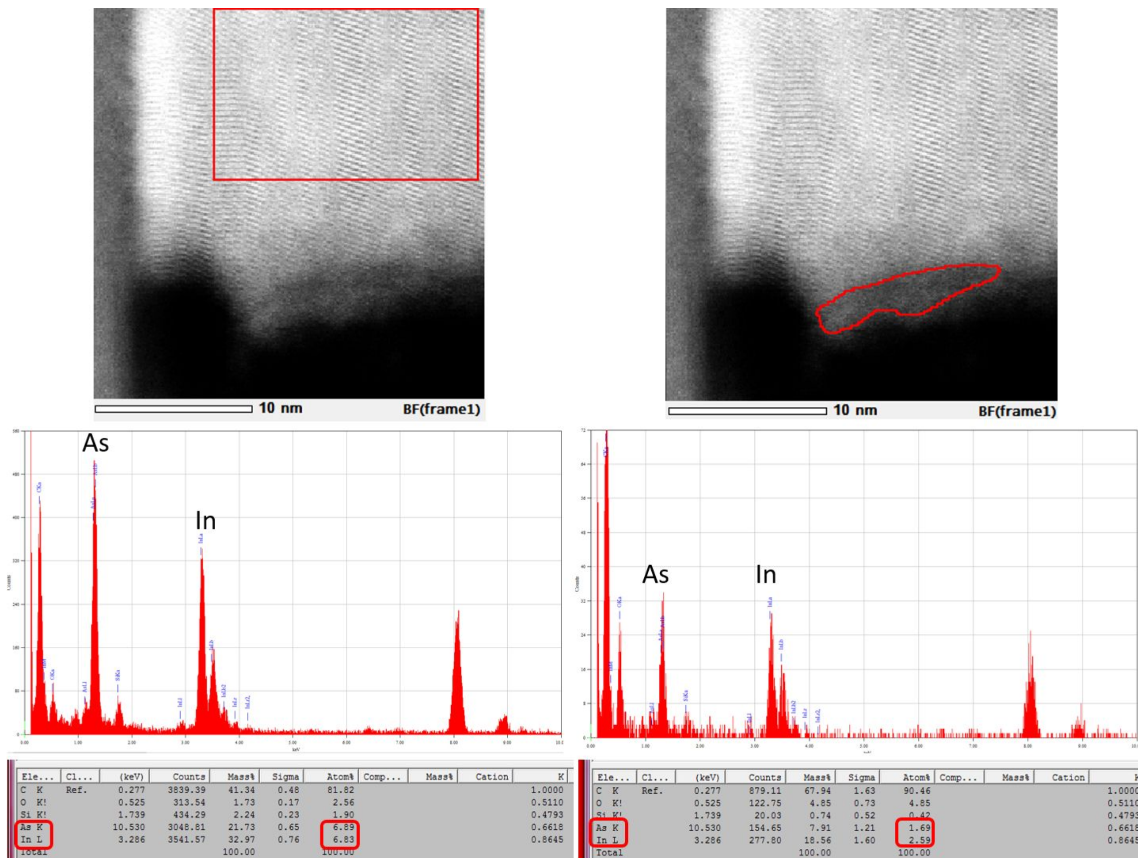

Ele...	Cl...	(keV)	Counts	Mass%	Sigma	Atom%	Comp...	Mass%	Cation	K
C K	Ref.	0.277	3839.39	41.34	0.48	81.82				1.0000
O K!		0.525	313.54	1.73	0.17	2.56				0.5110
Si K!		1.739	434.29	2.24	0.23	1.90				0.4793
As K		10.530	3048.81	21.73	0.65	6.89				0.6618
In L		3.286	3541.57	32.97	0.76	6.83				0.8645
Total				100.00		100.00				

Ele...	Cl...	(keV)	Counts	Mass%	Sigma	Atom%	Comp...	Mass%	Cation	K
C K	Ref.	0.277	879.11	67.94	1.63	90.46				1.0000
O K!		0.525	122.75	4.85	0.73	4.85				0.5110
Si K!		1.739	20.03	0.74	0.52	0.42				0.4793
As K		10.530	154.65	7.91	1.21	1.69				0.6618
In L		3.286	277.80	18.56	1.60	2.59				0.8645
Total				100.00		100.00				

Figure 3.10: EDX analysis of the chemical composition of the NW center and border.

The result is that at the NW center In and As have the same atomic concentration, instead at the border, where the amorphous oxide is located, the ratio is $In_{\%}/As_{\%} \sim 1.5$. This tell us that the oxide is mainly, but not only, constituted by group III element.

Furthermore, if the map is divided in small zones along the NW vertical direction, the As/In

[7]Moreover, at such scales, the sample is always slightly and randomly drifting so that a long acquisition time would have the same effect of taking a picture of an object in motion without a short enough exposure time.

ratio exhibits the clear trend shown if Fig. 3.11[8]. The As is more abundant than the In in the very first nanometers of NW, but, above $4\,nm$ they are quite equal (oscillations are related to low statistic in the defined integration areas).

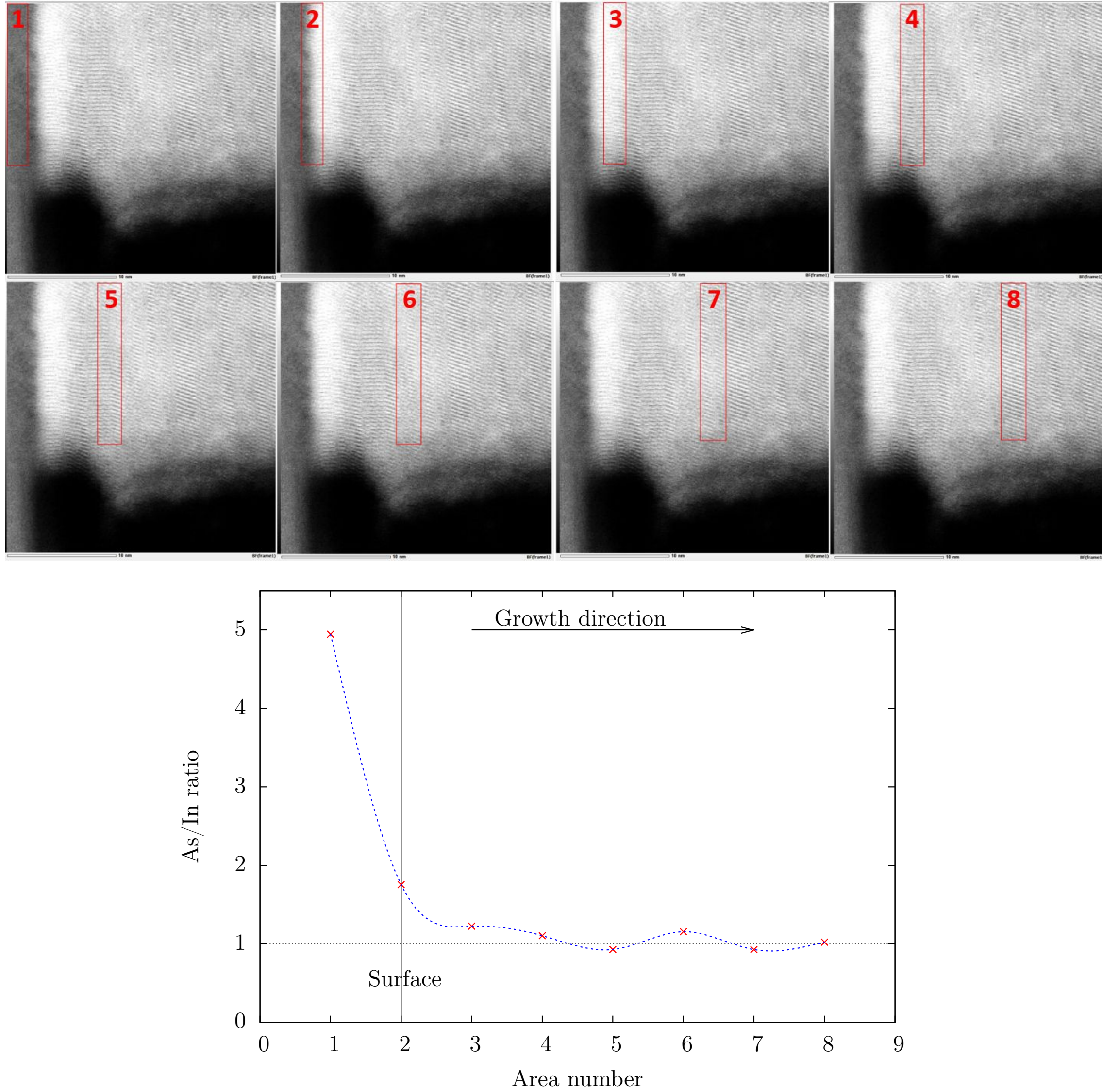

Figure 3.11: EDX analysis of As/In ratio along NW vertical direction using finite integration areas.

Finally, it is possible to use the EDX map to obtain a continuous profile of the atomic concentrations by integrating the map along a line for a given width. The result of the data manipulation along the vertical direction is reported in Fig. 3.12: the oxigen peak identifies the position of the surface oxide so that the interface is clearly located. Once again it is clear that there is systematically more As than In at the base of the NW. This confirms that the growth

[8]The x axis of the graph could be converted approximately in distances from the first integration box knowing that each box is $2\,nm$ tall. However they were defined manually, so the boxes are not perfectly contiguous.

starts with the As as had already been explained in [3] and [34].

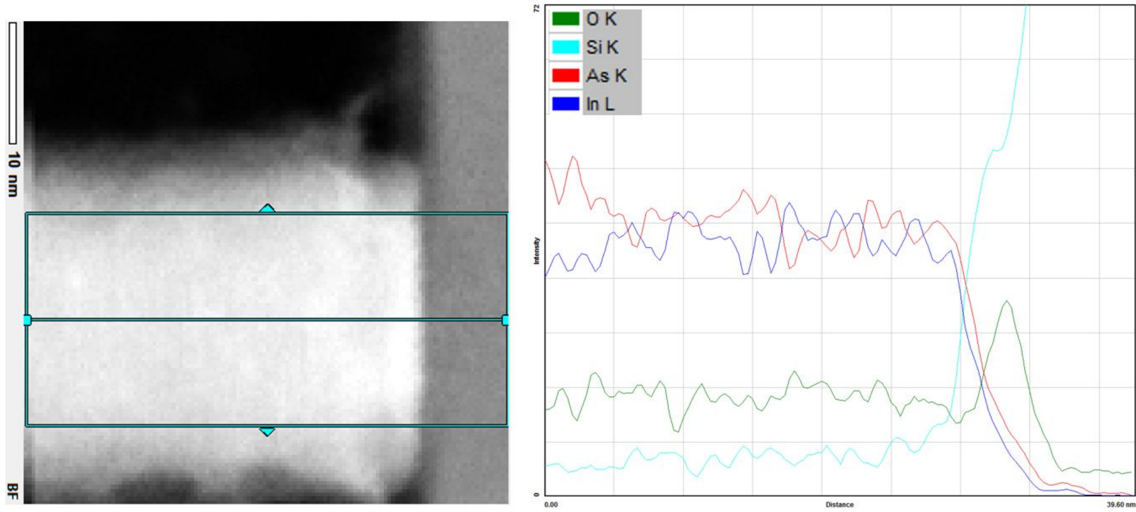

Figure 3.12: EDX analysis of NW chemical composition along vertical direction using a continuos integral method.

This kind of concentration profile can be obtained also along an horizontal section of the NW. However, no further information are obtained compared to the ones already reported and the oxide is not easily identified as in Fig. 3.10, probably because the NW is not a perfect cylinder.

3.3 H plasma effect

Going back to the surface treatments, we showed that the H plasma has a strong effect on the formation of islands both on the native oxide (compare Fig. 3.1 right and 3.2 left) and on HF etched one (compare Fig. 3.1 left and 3.3 top left). However , not a very big difference emerges when comparing the NWs in the sample with all the treatments and the one just without plasma (compare Fig. 3.3 top right and bottom right). Three interconnected questions are stimulated from this observation: (1) is the plasma treatment having any important influence if a thermal annealing process follows it? (2) is the temperature of the substrate during the plasma treatment influencing the result? (3) how does a low energy H plasma affect the Si surface?

Before going on, it has to be precised that in Fig. 3.3 the recipe included the pre-deposition of In droplets, however our attention now is focused on good NWs, so the answers for the listed questions will be searched in absence of In droplets, i.e. same recipe used in Fig. 3.4. Three more sample were grown making different adjustments to the plasma stage:

(a) the plasma step is removed and only 1 hour of degasing at $350\,^{\circ}C$ is applied;

(b) the plasma is applied with the usual parameters of $2\,SCCM$ flux and $250\,W$ power for one hour with sample at $350\,°C$;

(c) the plasma is applied with the usual parameters of $2\,SCCM$ flux and $250\,W$ power for one hour but with sample at $770\,°C$.

The following pictures illustrates the results for each recipe:

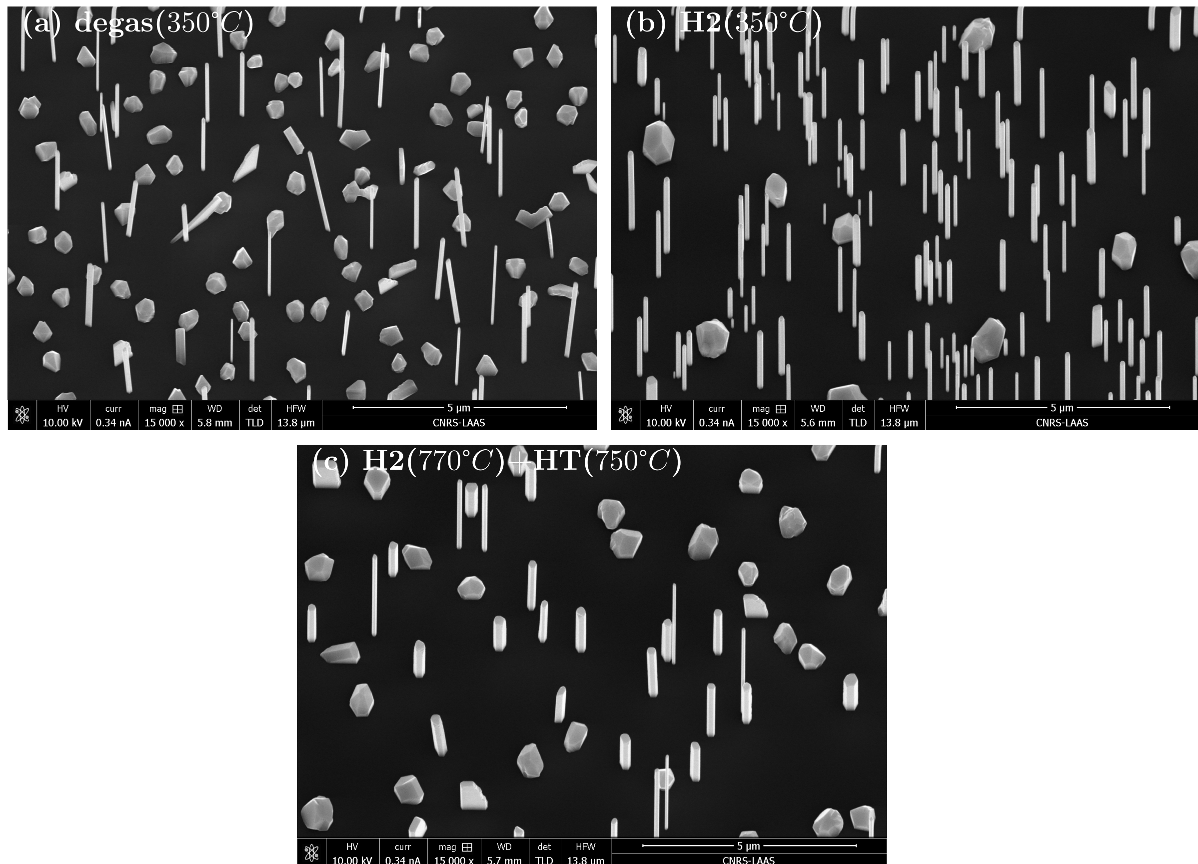

Figure 3.13: Series of samples to analyze the effect of H plasma on NWs growth: (a) simple degasing at $350\,°C$; (b) H plasma at $350\,°C$; (c) H plasma at $770\,°C$.

The comparison between the specimen without plasma (pic. (a)) and the one with a low substrate temperature plasma treatment (pic. (b)) clarifies that plasma has at least two effects: first it reduces the number of islands even if the ones still present are bigger, then it raises the vertical yield of the NW to 100%. In fact not a single tilted NW was found in this sample. To cause such consequences, we can predicts that the plasma is probably removing any contaminants and/or small reoxidation patches, and, at the same time, it is also having a chemical influence on the following growth steps. Indeed, to reduce the number of nucleating island, the adatoms diffusion lengths have to be altered and this can be caused or by surface roughness modification

or by a different chemical reconstruction of the surface.

One more evidence that makes us believe that a chemical modification is happening comes from the comparison of what happens with a plasma performed while the sample is at low temperature ($T = 350\,°C$, pic (b)) or at high temperature ($T = 770\,°C$, pic (c)). In the latter the NWs density strongly decreases in favor of the islands one. If the effect of the plasma were only to remove contaminants and/or reoxidized patches, the results should be even better because a higher substrate temperature is expected to enhance mobility and desorption of atoms from the substrate. Instead, something else, like a surface reconstruction or a chemical effect on the surface, must be acting so that it does not takes place anymore at a too high temperature. However, it is quite surprising the fact that a high temperature annealing step ($20\,min$ at $750\,°C$) is always following in our recipes: making a low temperature plasma followed by a high temperature annealing leads to a strongly different result from a high temperature plasma followed by a high temperature annealing. Thus, the after coming high temperature annealing does not ruin the previously applied plasma treatment as a simultaneous high temperature does. The explanation for this is that the thermal annealing in the growth chamber is performed under As atmosphere, causing the substitution of the H-terminated Si(111):1x1 reconstruction with the As-terminated Si(111):1x1 surface [35][36]. This means that the two high temperature treatments are different and, in the case of the plasma treatment, it requires a lower temperature to be effective.

To test the hypothesis about the influence of the plasma on surface roughness, we inspected some specific samples with an Atomic Force Microscope (AFM). After etching with the usual HF procedure three silicon substrates, they were treated with the three possible plasma procedures listed before skipping the thermal annealing and growth steps. The samples were etched, loaded under UHV and removed from it at the same time so that the reoxidation time was the same for all of them. The measurements, which results can be seen from Fig. 3.14 and Tab. 3.1, do not highlight any substantial difference regarding the roughness: the R_q varies around $0.2\,nm$ by some tenth of Angstrom that is well below the technique sensibility[9]. It is worth noting that, even if the images were processed to remove measurement artifacts, the important information were not lost in the process. Indeed, for example, the transverse line observable in the third image is the border of an incomplete Si bilayer. The height of this step is around $0.3\,nm$ that corresponds to the distance along [111] direction of two overlapping Si bilayer. The presence of such clear feature gives us a feedback both about the high sensibility of the technique as about the good image artifact filtering.

[9] R_q is the root mean squared of the surface height.

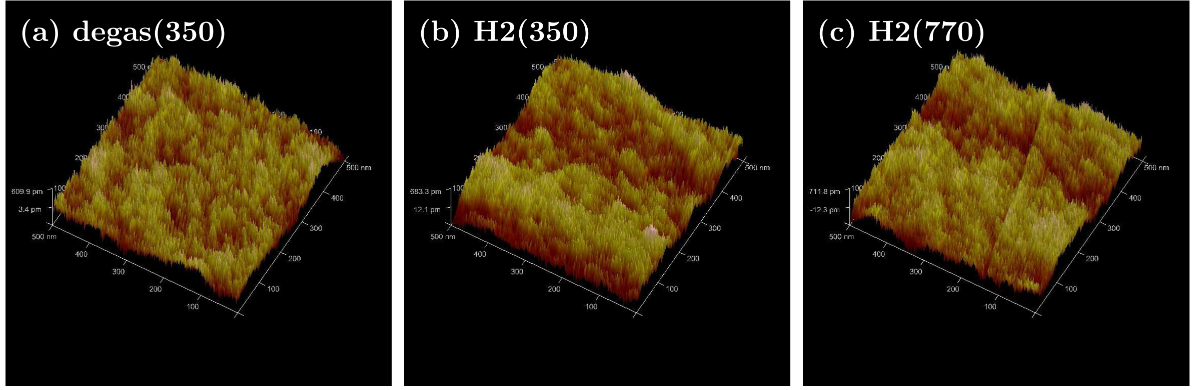

Figure 3.14: Series of samples to investegate the influence of H plasma on roughness: (a) simple degasing at 350 °C; (b) H plasma at 350 °C; (c) H plasma at 770 °C. All acquisiton scans have been done on a squared surface of $500x500\,nm^2$.

Sample	R_q (plane)	R_q (flat)
350 °C degasing	0.19 nm	0.18 nm
350 °C plasma	0.25 nm	0.20 nm
770 °C plasma	0.22 nm	0.21 nm

Table 3.1: AFM measured roughness, reported as root mean squared after using a light image processing (plane) and after using a strong image processing (flat).

From this evidences we conclude that the H plasma is not affecting the surface roughness in any substantial way on a scale bigger then Angstrom one. However, this does not exclude the possibility that the chemistry of the surface is changing through a surface reconstruction or H incorporation. Instead, to analyze the possibility that a low energy H plasma can etch the silicon oxide, we analyzed another special sample with the spectroscopy ellipsometry. A silicon oxide film was thermally grown on a silicon substrate and it was probed with the ellipsometer. The acquired spectrum was fitted using a model with all parameters fixed but the oxide thickness. This resulted to be $d = 17.03 \pm 0.05\,nm$ with a reduced chi squared of $\chi^2 = 0.46$. The associated error is calculated only from the variance of the fit, thus it is not representative of the real technique resolution that is strongly related to the correspondence between fitting model and real sample configuration[10]. The sample was measured again after applying a $1\,h$ plasma treatment with the usual conditions ($250\,W$, $2\,SCCM$, $T_{sub} = 350\,°C$). The result in this case was $d = 16.49 \pm 0.05\,nm$ with a reduced chi squared of $\chi^2 = 0.45$. These measurements suggest that the plasma has etched half nm of oxide but we must be cautious with such a conclusion for few reasons. The first one is that the associated error is underestimated and we are very close to the technique resolution limit. Moreover, a slight alteration of the probing angle can affect the measurement

[10] Debates still exist on ellipsometry resolution limit but it is commonly set at 1 Å.

outcome. Beside these measurement limitations, another hypotesis is that the plasma might have affected the oxide thickness by changing the $Si - SiO_2$ interface thickness. Such physical phenomena is described by Paneva et al. in [37] where they show how the RF H plasma cause a variation in the chemical composition of the interface. They claim that a thermally grown oxide is not perfectly abrupt with the underlying Si matrix and that $Si-O$ stoichiometry is not balanced at the interface. Applying an H plasma treatment causes a recombination and variation of the stoichiometry and this is seen from the ellipsometry, causing a difference in the oxide thickness fitting of $0.5\,nm$. To determine with ease which is the real explanation, one more experiment is mandatory: we plan to measure again the same sample before and after applying another plasma treatment. If the thickness will decrease, the oxide is really been etched; instead, if it remains unaltered, the previously observed reduction can be related to the Paneva's observations that can not happen again.

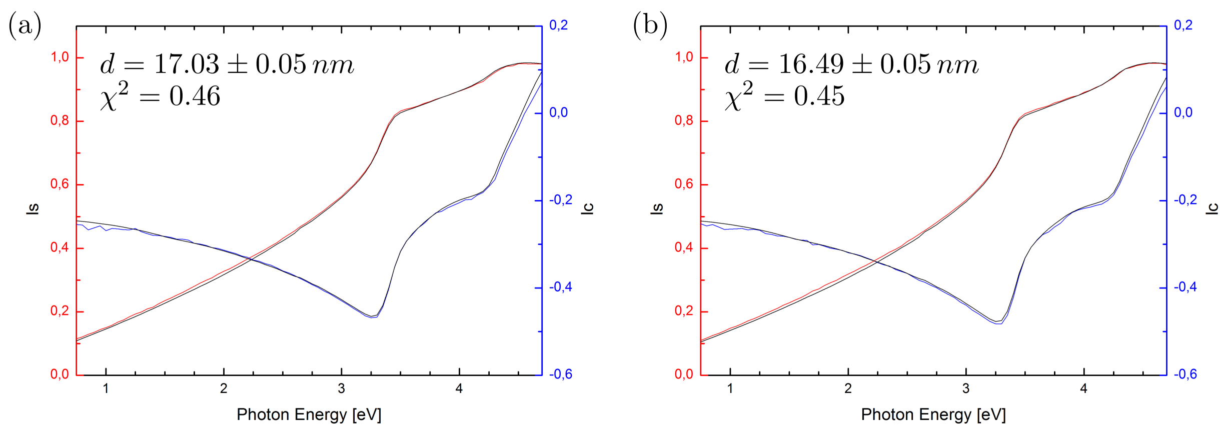

Figure 3.15: Spectroscopy ellipsometry measures and fits of $I_s = sin(\Psi)sin(\Delta)$ and $I_c = sin(\Psi)cos(\Delta)$. (a) Before plasma treatment; (b) after plasma treatment.

In conclusion, we learned that the H plasma treatment is necessary to obtain the best result in term of surface cleanliness and NW density. The physical justification for this improvement is not related to a substantial modification of the surface roughness and the oxide etching effect can not be confirmed yet and, in any case, it is very limited. Thus, considering our hypothesis, the plasma treatment should have predominantly a chemical or reconstruction effect that enhances the NWs growth. Still, the substrate temperature interval in which this phenomena happens has to be determined and studied with more experiments.

Chapter 4

Growth on patterned Si(111) surface

The acquired knowledge about surface preparation is transferred from the unpatterned substrates to those with a patterned silicon oxide mask. The aim is to obtain organized arrays of thin NWs while nullifying the formation of islands thanks to the surface protection offered by the oxide. In these conditions the *selective area* epitaxy takes place and the investigated surface treatments come in handy to clean and prepare the bottom of the holes carved into the oxide film. However, the space of growth parameters has to be scanned again because the adatoms behave differently on the oxide with respect to the bare silicon. This part of the work has still to be completed, but we will report hereby the results and observations obtained with the few realized experiments.

The specific procedure followed by one of our collaborators to create the mask is reported in Appendix C. What is important to us is that the designed schematic has three areas:

1. A planar and totally cleaned surface which mimics the unpatterned surface, thus it gives us a link with the previous part of the work.
2. A series of holes arrays organized in a chessboard-like disposition. Along one direction of the chessboard the holes diameter increases while along the other the holes pitch increases[1]. This is the proper patterned zone from which we want to obtain localized and arranged NWs.
3. A series of lines carved with different orientations, width and spacing.

Overall, the chessboard is made by 32 patterns: all the possible combinations of 8 diameters $(20, 40, 60, 80, 100, 120, 150, 200\,nm)$ with 4 pitches $(100, 250, 500, 1000\,nm)$. In the following we will refer to a given holes array using its diameter and pitch from the design $(d\#\,p\#)$. In

[1] The holes pitch is the distance between two adjacent holes.

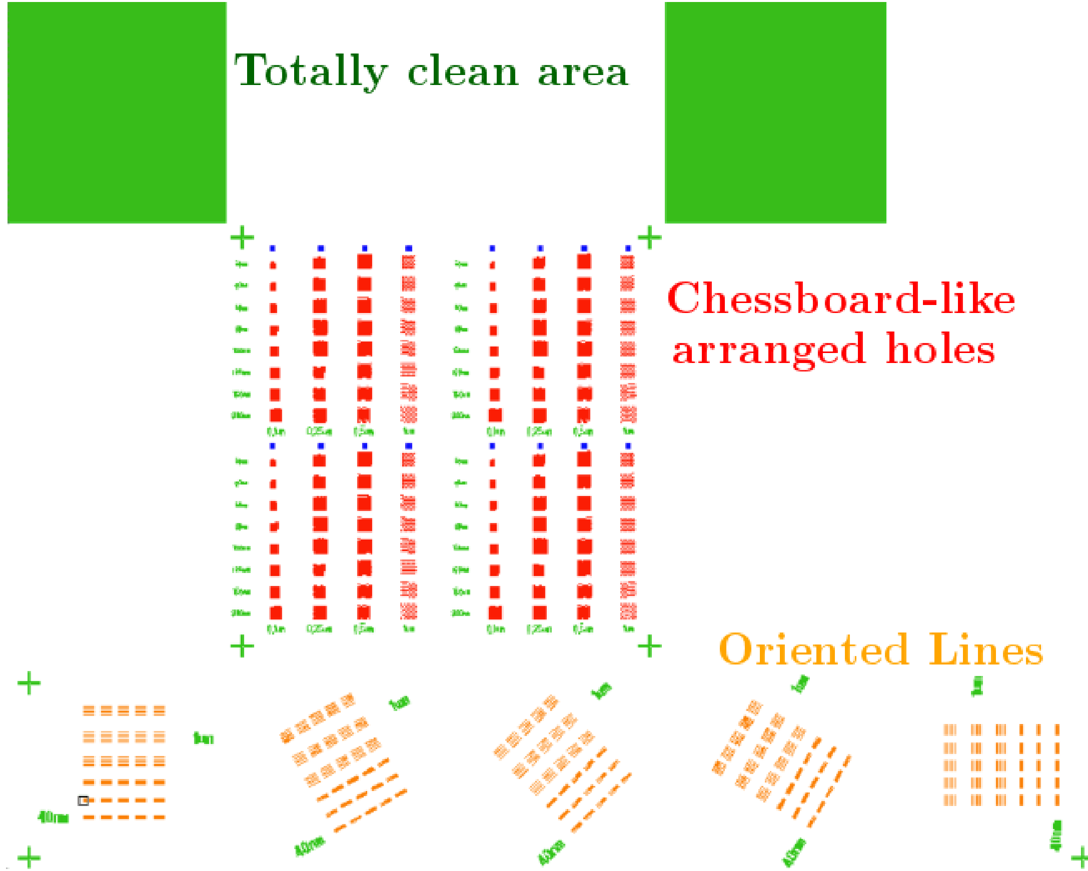

Figure 4.1: Schematic of the pattern followed for the exposition of the PMMA during mask creation.

practice, these holes can have slightly different geometric properties because the development of the photoresist and the HF etching are done manually (mainly the holes diameter can be bigger). Instead, a good control is held on the thickness of the oxide that can not vary more than half a nanometer around 17 nm because the procedure is calibrated so that it has the smallest variation as possible.

We started our investigation on patterned substrate without using the H plasma treatment. All other parameters are the same as those used for the sample in Fig. 3.4 (HF + thermal annealing at 750 $^{\circ}C$, $T_g = 525\,^{\circ}C$, $V/III = 200$, no In droplets) and the result of such a recipe is partially shown in the left image of Fig. 4.2. It is clear that only some NWs are vertical and that some holes are even empty. Furthermore, islands and other structures are nucleating outside the holes, denying our intention to have a perfectly clean silicon oxide. This problem is immediately overcame by raising the growth temperature to $T_g = 540\,^{\circ}C$ (see right image of Fig. 4.2), that means increasing the adatoms desorption rate and diffusion length on the oxide surface. It is important to notice that, as we will see soon, the growth outcome strongly depends at which slot

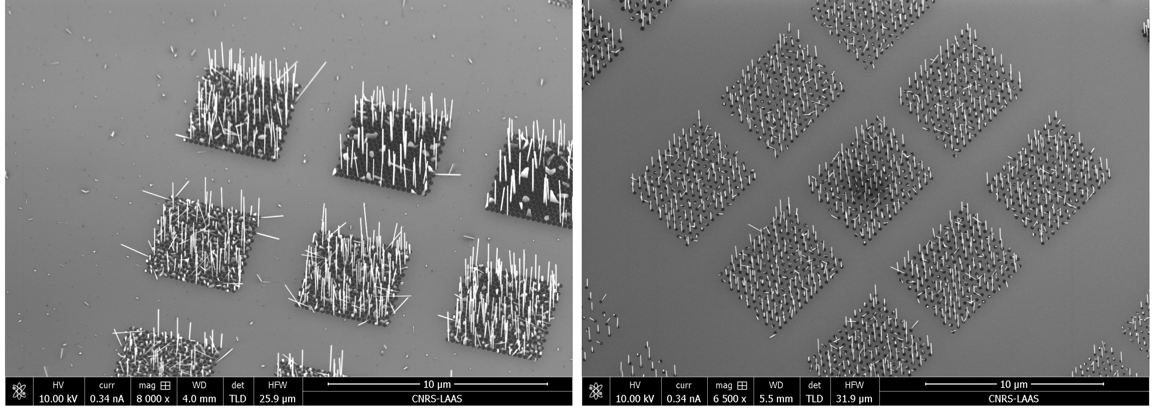

Figure 4.2: SEM top global view of two patterned samples: on the left the sample grown with usual parameter; on the right sample grown at $T_g = 540\,°C$.

we look among those present in the chessboard array. Indeed, our quality estimators, the total nucleation yield and the vertical yield, which we define as:

$$N_{yield} = \text{Nucleation yield} = \frac{\#\text{ of holes filled with whatever structure}}{\text{total number of holes}}$$

$$V_{yield} = \text{Vertical yield} = \frac{\#\text{ of holes with vertical NWs}}{\text{total number of holes}}$$

are both strongly dependent from the diameter of the holes.

Introducing the H plasma treatment while keeping $T_g = 540\,°C$, brings to our best result this far. In Fig. 4.3 it is possible to see a series of patterns with the same pitch ($100\,nm$) and increasing holes diameters. Few features can be recognized at first glance:

- vertical NWs nucleate more easily at bigger holes;
- the smaller the holes the higher the number of those that remain empty;
- NWs are not filling the whole diameter of the holes, instead they tend to nucleate at their border. The phenomena can be explained using a triple phase model like the one proposed in [38].

These observations teach us that the NWs diameter is not limited by the one of the holes, but, at the same time, the latter strongly influences N_{yield} and V_{yield}. Our explanation is based on the holes aspect ratio: the holes with a small diameter have a shadow effect on their bottom, thus adatoms have smaller probability to reach it and nucleate a NW. Moreover, it is possible that the limitation of the holes aperture prevents a good cleaning during the HF etching[2] and, eventually,

[2] As explained in C, a small oxide layer of $3\,nm$ is left at the bottom of the holes during mask fabrication

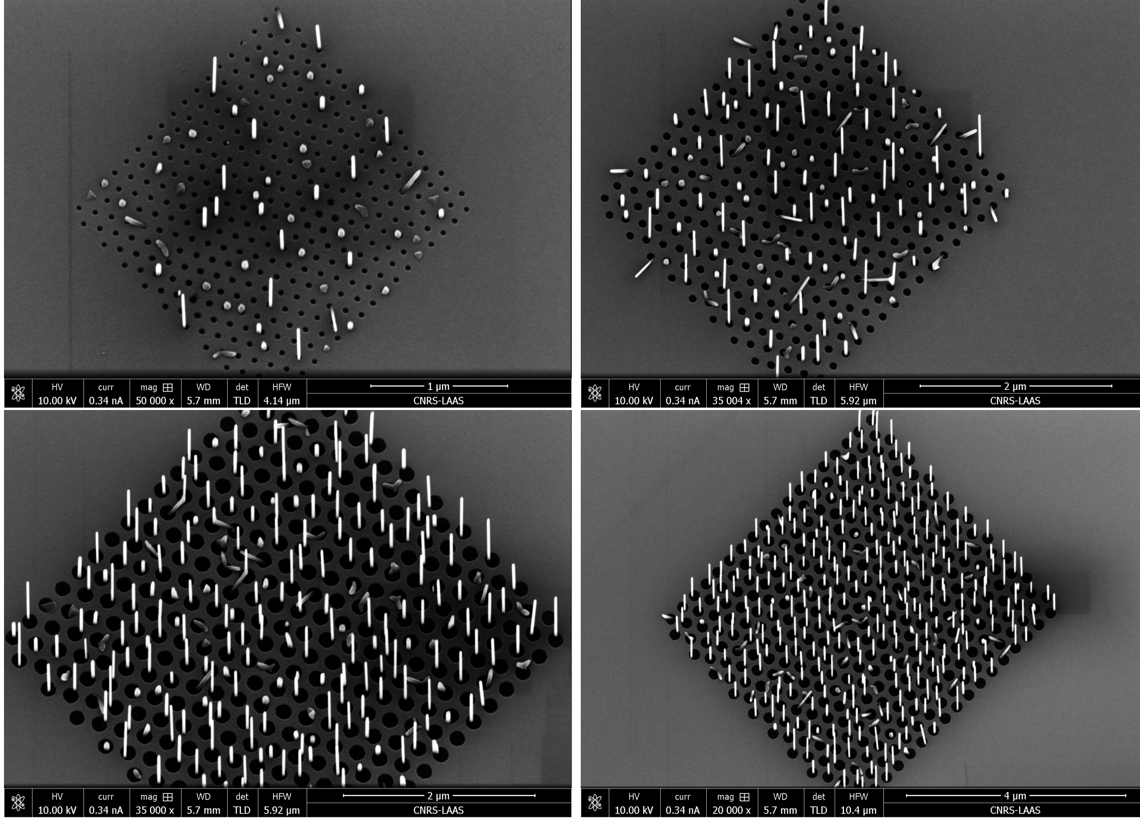

Figure 4.3: Four patterns from the chessboard with fixed pitch of $100\,nm$ and different holas diameter, in order: $d = 20\,nm$, $d = 80\,nm$, $d = 150\,nm$, $d = 200\,nm$. Image scales are different because of the different pattern dimension.

the remaining oxide could obstruct NWs nucleation and keep the holes empty. Furthermore, it is evident that in the case of big holes the NWs are much more homogeneous in length. This is explained by combining two phenomena: firstly bigger holes favor the nucleation, thus it is more probable that NWs nucleate at the same time and have same time to grow; secondly, there is a critical density (i.e. pitch) under which the growth regime is driven by competitive material recollection and, if some of the NW nucleated before the other, it could dominate recollection and induce shadowing on other holes around itself[3].

Thanks to the script developed by one of the member of our group, we analyzed the SEM images extracting N_{yield} and V_{yield} for all the 32 patterns of the sample discussed in the last paragraph. The obtained values, reported in Fig. 4.4, are in good agreement with the observations drawn out of Fig. 4.3, thus are valid for all the pitches. In particular, we can see that for pitches of 100 and $250\,nm$ the trends are very regular both in N_{yield} and V_{yield}. Instead,

in order to protect them from uncontrolled re-oxidation. The layer is removed with a quick HF etching before loading the specimen in the MBE system.

[3]Growth regime are explained by Hertenberger in [24].

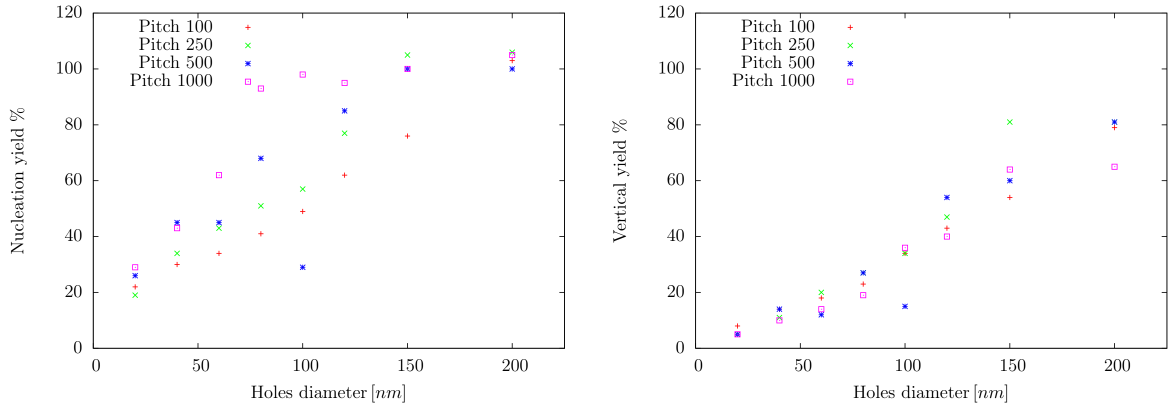

Figure 4.4: Nucleation and vertical yield of all the patterns in function of their holes diameter.

for the larger ones, 500 and 1000 nm the N_{yield} dispersion is much bigger and some outliers are present. It is important to underline that these data are affected by the inability of the script to distinguish between two overlapped structures and by to detect very small NWs. In the case of N_{yield}, sometimes two structures that grow from the same hole are counted twice, thus the yield can go beyond 100% (overestimated); whereas, in the case of N_{yield}, sometimes small NWs are not counted and in other case they overlap, contributing as one (underestimated). By manual checking on a couple of the more critical patterns (the higher the density, the higher the miscalculation), the overestimation (or underestimation) never exceeds 5%.

A preliminary statistic has also been done on length and diameter of the NWs. Despite both of them have big variance (especially the length, as can be guessed from Fig. 4.3), a clear trend of their mean value emerges: lengths and diameters grow monotonically with respect to the holes diameter with a correlation always higher than 0.95. Instead, in first analysis, the pitch does not play a relevant role. It is worth noting that it is difficult to say with this single evidence which is the exact physical phenomena that causes this correlation. Indeed, on one hand it could again be easily related to the fact that big holes favor the fast nucleation of NWs, thus they have more time to grow. On the other hand bigger holes mean also more space between single NW, thus less competitive growth. Overall, we can attribute a mean diameter of $45 \pm 5\, nm$ to all the patterns with 200 nm pitch that are those with the highest vertical yield.

Chapter 5

Ab-initio simulations

In this chapter I will report about the simulation activity that I have carried out using an *ab-initio* approach. For this calculations the Vienna Ab-initio Simulation Package (VASP) was used, combining its potential with other scripts when necessary[1]. The calculation algorithm of VASP will not be explained here, but in Appendix D it is possible to find the physical theory on which it is based. To understand the following sections, it is sufficient to know that the program takes in input an arbitrary disposition of atoms and it searches for the configuration in which the total energy of the system and the internal forces are minimized down to a dictated threshold (convergence criteria). The out coming disposition is necessarily related to the starting one and can also be consequence of the code stopping at a local minimum of the total energy. The key point of the *ab-initio* method is that the calculation is based only on atom species and does not require any other information or experimental data. It is important to underline that here the effect of the temperature is not taken into account, thus the results are not directly connected to the experimental outcome. However, we will get an insight at how adatoms can interact on different surfaces and, in the coming days, these data will be employed to develop a kinetic Monte Carlo simulation of the nucleation/growth process where the temperature plays a key role.

5.1 Substrate construction and approximations

VASP is basically a powerful mathematical tool that solves the Hamiltonian of a many-body system by combining the Density Functional Theory with other approximations to make the problem resolvable. Still, an obstacle remains: the code has parts that are not scaling linearly with the number of considered atoms, thus the sample must be reduced to a much simpler one

[1] Like the Nudged Elastic Band from University of Texas

(built out of $10^2 - 10^3$ atoms) without losing in physical meaning. The strategy is to identify how few atoms interact at the atomic scale with a DFT approach and then use the acquired data in a bigger scale model like the kinetic Monte Carlo.

In our calculations we decided to reduce the sample to a 4x4 (or 8x8) surface, that means having 16 (or 84) atoms of Si on the topmost layer. More in details, the structure is build as follows:

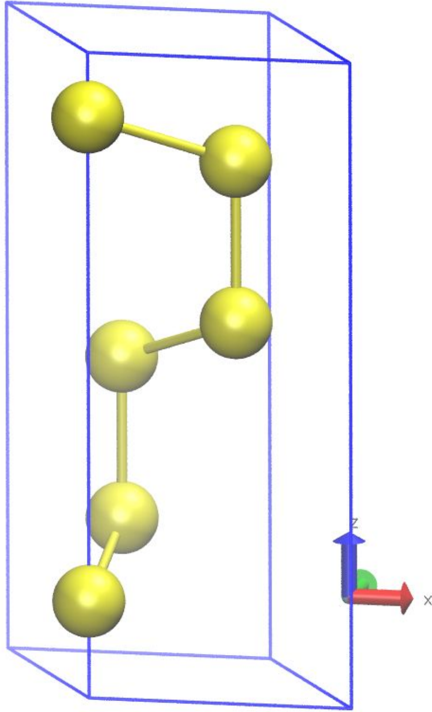

Figure 5.1: Starting Si base cell with z direction corresponding to <111>.

- A base cell composed by 6 Si atoms is the starting building block (see Fig. 5.1): it is already aligned in the <111> direction along the z axis and has the vertical facets in the <112> direction. The blue box represents the periodic boundary conditions (PBC) that are already correctly set to make of this small structure a virtually infinite Si crystal.

- The cell is conveniently repeated along its crystal axes in order to build a bigger structure. In our case we cloned the cell by translating it along each facet directions 4 (or 8) times and 2 times along the z direction.

- The outcome is a perfect silicon crystal with 192 (or 768) atoms, enclosed in perfect periodic boundary conditions.

- To virtually generate a surface, the PBC along the Z axis are changed by moving both the bottom border 5 Å deeper and the top border 15 Å higher. This generates 20 Å of empty space and, at the same time, creates unbounded electrons at bottom and top surfaces.

- The bottom charges are saturated with a layer of 16 H atoms and the result is shown in Fig. 5.2 (a). Instead, the top charges are left unpaired for now.

- Then the structure is relaxed two times (i.e. VASP calculates the lowest energy configuration). Firstly, all atoms are forcefully kept fix but the bottom H layer. The H atoms get to 1.5 Å from the above Si layer keeping their perfect alignment to the substrate (see Fig. 5.2 (b)). Next, the six topmost layers of Si are relaxed, keeping all the other fixed (see Fig. 5.2 (c)-(d)).

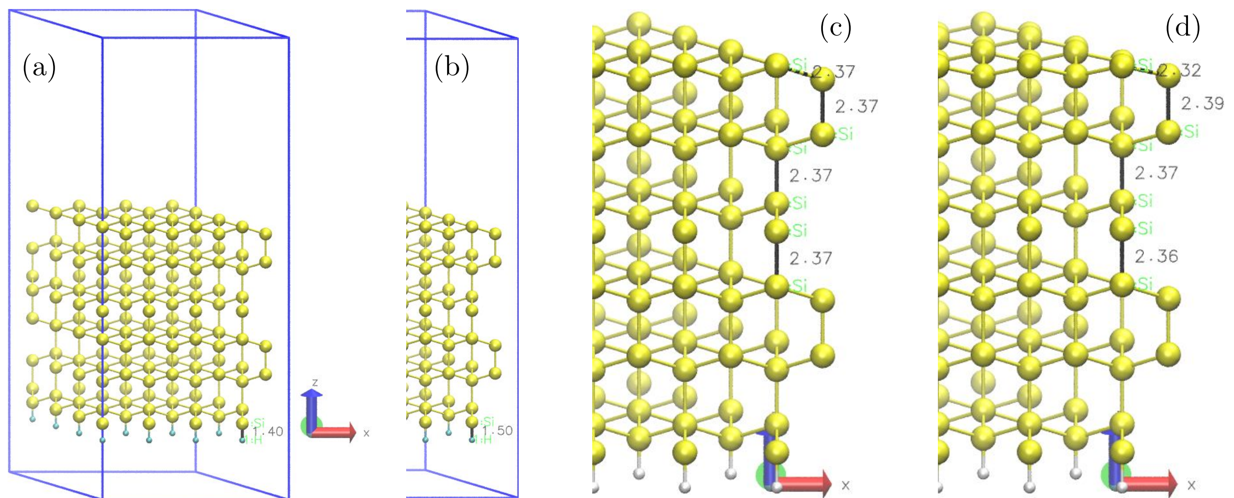

Figure 5.2: Yellow balls are silicon atoms, white balls are hydrogen atoms, the lines help the eye follow the crystal structure, numbers are distances between atoms in Å. (a) Final atoms configuration with blue box of PBC. (b) Section with distance of H bottom layer in evidence after its relaxation. (c) and (d) highligh how the 6 topmost layers of Si relax.

All these steps were performed using a program realized by me that allows to build such structures with whichever desired dimensions and in a format that is ready as input for VASP. Furthermore, the program allows to find specific layers of atoms, freeze or free them, add or eliminate atoms and find specific positions like "near neighbor of..." or "centered regard to...". In conlcusion, our starting surface is composed by 6 relaxed Si layers laid on 6 unaltered and fixed Si layers and one terminating layer of H. However, such a surface does not actually exist because Si atoms at the surface have only three bonds, thus for each atom there is an unpaired electron. Therefore the first step is to understand which are the possible surface configurations that really exist in our experimental samples.

Initally, we supposed three possible configurations as consequence of the applied pre-treatments. From the literature we know that an HF etching leaves the surface mainly covered with hydrogen, so an H-terminated $Si(111)$ 1x1 surface could be an obvious starting point (see Fig. 5.3 (a)). Moreover, from our experiments, we confirmed that the H plasma treatment does not have any big structural effect, but it has some chemical/reconstruction effect on the surface. Thus the associated surface configuration is the same and the real effect of the H plasma could be indeed to enhance the H-termination or/and remove impurities and re-oxidation patches. Then, we know that the indium pre-wetting does not facilitate the growth of small vertical NWs, so a related surface was not even considered. Instead, for the thermal annealing under arsenic atmosphere two configuration were taken into consideration. The first predicts a layer of As that vertically

terminates the silicon dangling bonds, as shown in Fig. 5.3 (b). However, such a configuration generates a heavy reconstruction of the layer itself because it has to reduce its own dangling bonds. Furthermore, it facilitates the (111)A growth direction, which gives non-vertical NWs (go back to Fig. 1.5,) and so it was discarded after a short investigation. Instead, the most interesting surface is given by an *As* layer that substitute to the topmost layer of *Si* and which is commonly called As-terminated *Si*(111):1x1 reconstruction (see Fig. 5.3 (c)). On one hand this structure is licit because it directly promotes the (111)B growth direction, but, on the other hand, it was not clear to us how it could form. Actually, the matter has already been studied in depth and many articles already exist on this specific situation. Experimentally, it has been confirmed using the surface-sensitive core-level spectroscopy [39], the scanning tunneling microscopy [40] and the x-ray standing waves [41] that, if a thermal annealing is applied on a H-terminate *Si*(111):1x1 (Fig. 5.3 (a)) under an *As* atmosphere, the *As* forms the already described structure (Fig. 5.3 (c)) preventing the formation of the *Si* 7x7 reconstruction. Moreover, *ab-initio* calculations about the precise *As* position with respect to the silicon matrix have already been performed, even if the considered structures were much smaller than ours [36],[35]. The outcome of this calculation can be resumed by the $Si - As$ bond length that in our calculations results 2.46 Å and it is perfectly compatible with the results of all previously cited articles. It is worth noting that this structure, that we will call As-term for shortness, is so stable that it is often considered as an effective passivation of the silicon surface. The explanation is that the two free electrons of each *As* form a stable electron pair thus reducing dangling bonds to zero.

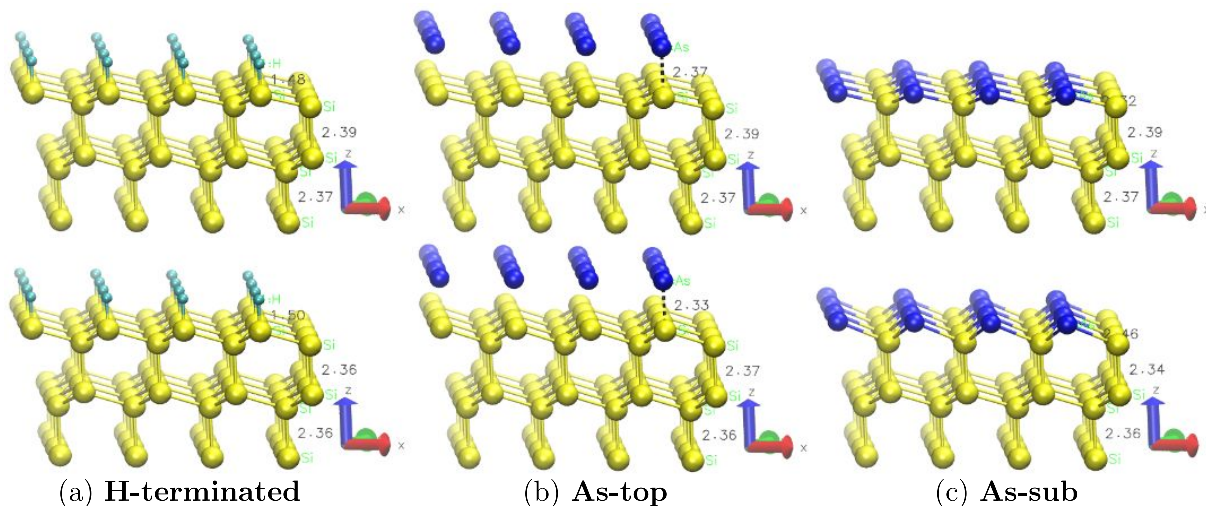

(a) **H-terminated** (b) **As-top** (c) **As-sub**

Figure 5.3: Yellow balls = *Si*, cyan balls = *H*, blue balls = *As*. These are the three starting surface configurations with camera near <110> direction: (a) H-terminated *Si*(111):1x1 surface; (b) top As-terminated *Si*(111):1x1 surface; (c) As-terminated *Si*(111):1x1 surface. The configurations above are the arbitrary ones, instead the ones below are relaxed.

In the following sections we will analyze in details the behavior of In and As both on the H-term surface and on the As-sub surface. We will start in both cases with the study of the adsorption energy of a single atom, and then we will make a step further considering specific situations like research of energy barriers, possible chemical reactions and interactions between two or more atoms.

5.2 The H-terminated $Si(111)$:1x1 surface

The first objective of the investigation is to find the stationary positions of In and As on the surface and, at the same time, calculate their adsorption energy. To do this, I proceeded taking advantage of the symmetry of our substrate. In particular, if we take a look at our surface from the top, i.e. along the <111> direction, the surface seems to be composed by hexagons (see third column of Fig. 5.4). Actually, there are two types of hexagons: those that have H vertexes (cyan balls) an those that have Si vertexes (yellow balls). The previous are really existent flat hexagons and are all equivalent with respect to translation; instead, the former are just apparent hexagons that we can see because of the projection direction. Indeed, they are formed by Si atoms at different depths. All this is to say that we can regroup the Si atoms visible from the <111> direction in three sets:

- (**top**) Si atoms which are under an H. These Si atoms belong to the topmost Si layer;
- (**b3A**) Si atoms in the middle between three H which form a triangle with a vertex heading towards positive y. These belong to the second Si layer from the top;
- (**b3B**) Si atoms in the middle between three H which form a triangle with a vertex heading towards negative y. These belong to the fourth Si layer from the top.

The three sets have in common that each point is the center of a C_3 symmetry with respect to the <111> direction [2] and we will focus our study on positions related to them. In the following, an atom vertically aligned with the first, second or third type of Si atom will be said to be in **top**, **b3A** or **b3B** position, respectively. One more interesting starting position is when an ad-atom is aligned between 2 Si atoms of the topmost layer; in this case it will be said to be in **b2** position. Finally, to efficaciously show the results of calculations, I will report in order the starting configuration from a point of view close to the <110> direction and then the relaxed configuration along the exact <110> and <111> direction (as in Fig. 5.4).

[2] C_n is the discrete rotational symmetry of the nth order, with respect to a particular point in 2D or axis in 3D, and it means that a rotation by an angle of $360°/n$ map each points of the object in an equivalent one.

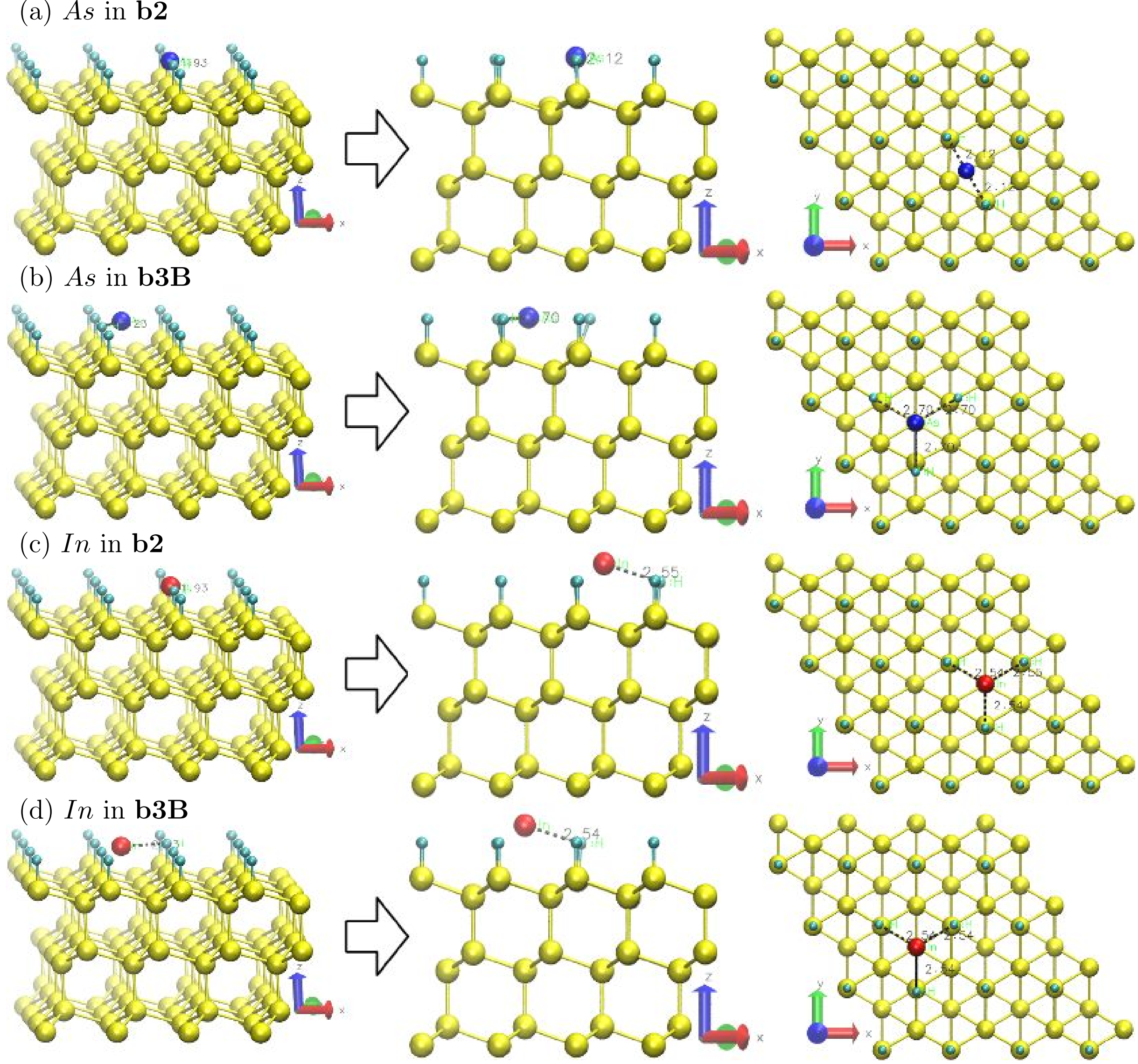

Figure 5.4: Yellow balls = Si, cyan balls = H, blue balls = As, red balls = In. Investigation of the stable configurations of a single atoms on **H-term** surface. On the left the starting configurations, on the right the relaxed ones looked from <110> and <111> directions.

Config. I	$As-H$[Å]	$In-H$[Å]
b2	2.12	2.55
b3B & b3A	2.70	2.54
Ref. calc.	1.54	1.74
Tabulated	1.52	1.68

Table 5.1: Bond lengths of $In-H$ and $As-H$ comparison between calculations on substrate (b2, b3B & b3A) and references.

From Fig. 5.4 we can immediately see how As and In behave differently on the H-term surface: the previous stays close to the starting position whereas former is heavily displaced. This can be related to their different size ($R_{In} \sim 1.6\,\text{Å}$, $R_{As} \sim 1.2\,\text{Å}$), but it has to be noticed that, in all cases, the final distance between them and the surrounding H atoms is bigger than the expected covalent bond length. The actual values can be compared in Tab. 5.1 where I reported the distances obtained from the surface

simulations, from references calculations on simple molecules (like InH_3 and AsH_3) and from tabulated experimental data. Thus, the H atoms prefers to maintain a strong bond with the Si substrate and keep the adatoms far from the surface.

More in details, the As causes a slight displacement of the surrounding H atoms and it totally stays in its position, not getting closer of further from the substrate both in the **b2** and in the **b3B** positions. Instead, the In exits the surface while the H atoms stay close to their original positions. It is interesting to notice that the In goes from **b2** to **b3B** position, with the exact same configuration as the one obtained starting from **b3B**. This tells us that the In is unstable in the **b2** position and that the **b3B** final configuration is really stable. What happens for the **b3A** position (not reported in images) is really similar to the **b3B** case and the distances with the H atoms are the same. However, the substrate is much more affected by the adatoms presence because the underlying Si atom is closer to it and so they have a stronger interaction. To evaluate which configuration is more stable we make use of the adsorption energy E_{Ads} that, if negative, represents the energy necessary to free the adatom from the surface:

$$E_{Ads} = E_{\text{1 adatom config.}} - E_{\text{Relaxed surf.}} - E_{\text{Adatom ref.}}$$

The first contribution is the total energy of the relaxed system with 1 adatom, the second one is the total energy of the system before the adatom was introduced and the last one is the energy that the adatom has in a vacuum with the predefined PBC. Actually, in the case of As, we decided to estimated the last contribute taking one fourth of the energy of AS_4 in vacuum because this is the molecule that is being evaporated from the As cell in our MBE setup. The same problem does not stand for In because it is evaporated in the elemental form.

Config. I	$E_{Ads}(As_4)\,[eV]$	$E_{Ads}(As)\,[eV]$	$E_{Ads}(In)\,[eV]$
b2	2.38	−0.41	−0.83
b3B	3.13	0.33	−0.83
b3A	3.52	0.73	−0.85

Table 5.2: Adsorption energy for single As (from an As_4 or monoatomic As) and In on H-term surface.

The adsorption energies found for an As coming from an As_4 (see Tab. 5.2) are positive and higher than $2\,eV$. These values tells us that is strongly unfavorable for the system to split an incoming As_4 in 4 atoms and place them in the identified stable positions. Moreover, there is quite a relevant difference in energy between the position **b3B** and **b3A** because the surface deformation induced by the adatom is stronger in the second case. It has to be noticed that such a process is really unlikely to happen in our experimental setup so it is better

to ideally consider the $E_{\text{Adatom ref.}}$ as the one associated with a single As in vacuum. If this is the case, the **b2** position becomes energetically favorable. Instead, for In the situation is easier: it has just one stable final configuration and there is not a big difference between the **b3** positions because the Si matrix is quite unaffected in both cases.

To further study the stability of the In final position, I made use of the *drag method*. This technique consists in forcefully dragging one atom from one position to another in order to verify if there is a potential barrier between the two of them. The atom is moved by a small amount from its previous position and it is kept fix only along the translation direction. The procedure is iterated up to when a path is obtained. Here the aim is to check if there is a stable position for the In between the H layer and the Si topmost one on **b3B** spot. The calculation was done by translating the In along the z axis by steps of 0.25 Å starting from the stable position (see Fig. 5.5 (a)). As shown in Fig. 5.5 (b), pushing in or pulling out the In from the surface only increases the total energy (red line) while an opposing force develops to bring back the system to its stable position (blue line). Thus no metastable state exists in the explored range.

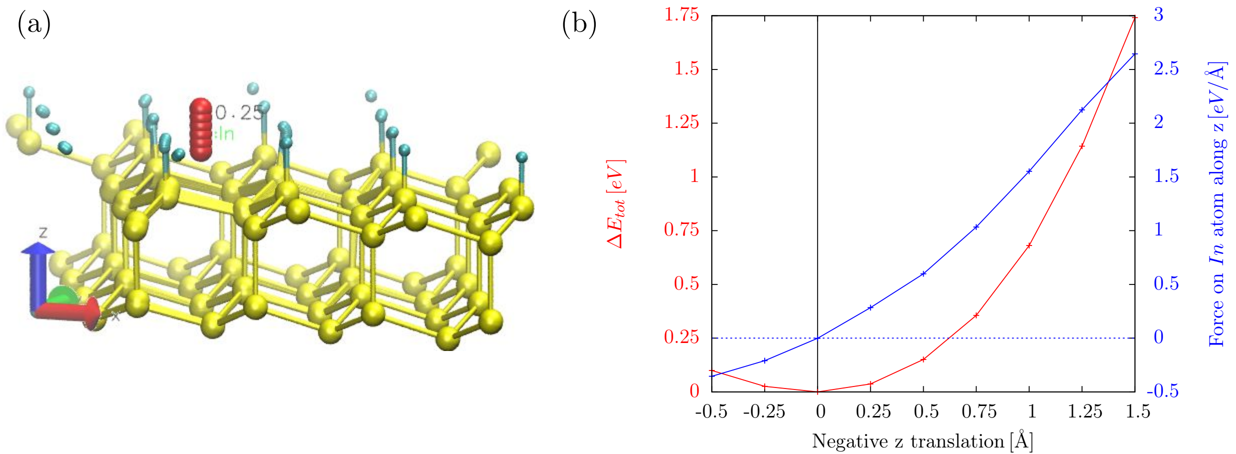

Figure 5.5: (a) Overlapped results of drag method for In on H-term surface at **b3B** position; (b) Red line represents the difference in total energy in function of the translation along z axis from the stable position; blue line represent the z component of the force acting on the In atom.

From what we have seen up to now the In is not forming any bond, nor with the H nor with the underlying Si. Thus, to have $In - Si$ bonds it is necessary to remove H from the surface. The possibility that the In substitutes to the H atoms is interesting because, once the H has been removed, the In can take its **top** position and favor the (111)B growth direction. The leading idea is that some chemical reactions might take place and we want to see if they are favorable or not. In particular we studied two cases:

- if two H atoms get closer thanks to one or two incoming In, an hydrogen molecule could form and leave space for the In to bond with the silicon matrix. The reactions are:

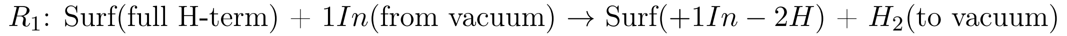
R_1: Surf(full H-term) + $1In$(from vacuum) $\rightarrow$ Surf($+1In - 2H$) + H_2(to vacuum)

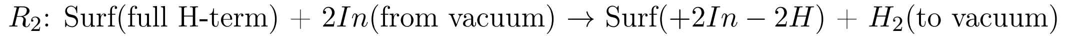
R_2: Surf(full H-term) + $2In$(from vacuum) $\rightarrow$ Surf($+2In - 2H$) + H_2(to vacuum)

- alternatively, if three H atoms bonds with one In, forming InH_3, another In, that might have helped the reaction, can take their place:

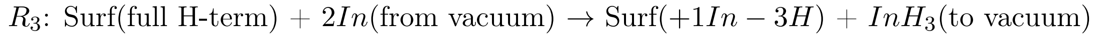
R_3: Surf(full H-term) + $2In$(from vacuum) $\rightarrow$ Surf($+1In - 3H$) + InH_3(to vacuum)

To evaluate if the reactions are favorable or not it is sufficient to compute the energy difference between their final and starting states, taking into account also the energy in vacuum of the incoming (or leaving) atoms (or molecules). It is worth noting that this approach does not tell us which is the energy barrier that has to be overcome in order for a reaction to take place. Thus, it is possible that, even if a reaction brings to a lower energy configuration than another one, it might be more improbable due to the higher energy barrier associated. Furthermore, as before, there is more than one final stable configuration and several have been investigated. Eventually, only the one with the lowest final energy will be reported in details.

Config. I	$\Delta E(R_1)\,[eV]$	notes
b3Amid	4.07	Config. F: close to b2
b3Bmid	4.07	Config. F: close to b2
top	4.07	Config. F: close to b2
b3Alat1	4.64	One unbound e^-
b3Blat1	4.66	One unbound e^-
b3Alat2	4.62	One unbound e^-
b3Blat2	4.63	One unbound e^-

Table 5.3: Energy differences for $R1$.

For reaction $R1$, once two near neighbor H are removed, one In atom has to be introduced on the surface. In the freed area, there are 3 possible **b3B** positions, 3 possible **b3A** positions and one possible **top** position, where symmetric spots have already been grouped (12 positions in total, 7 independent). As it is reported in Tab. 5.3, ΔE for reaction $R1$ is always positive and bigger than $4\,eV$. In particular, the first three configurations relax to the very same position that is close to a **b2** spot. These are reported in details in Fig. 5.6: images (a) and (d) show how R1 should take place (projection along <110> direction); instead, image (b) and (c) are both the result of overlapping, respectively, the starting configurations and the relaxed ones for those three cases that get to the same final configuration (projection along <111> direction). Actually, the three superimposed final configurations differ in the atoms position by an amount inferior 10^{-3}Å that is related to the energy and forces convergence criteria. The other four initial configurations relax to a final state that is similar among them: the In moves towards the closest **top** position

left by one of the removed H and it is not able to reach the **b2** position by itself. Therefore, one Si remains exposed with one unbound electron. In fact, such final configurations are metastable, and their energy barrier has to be low and narrow: translating by 0.25 Å the In towards the **b2** position makes all the configurations collapse on it. In conclusion, for reaction $R1$, the **b2** position reported in Fig. 5.6 (c) really is the only stable one with a $Si-In$ bond length of 2.88 Å and an energy cost of $\Delta E \sim 4.1\, eV$.

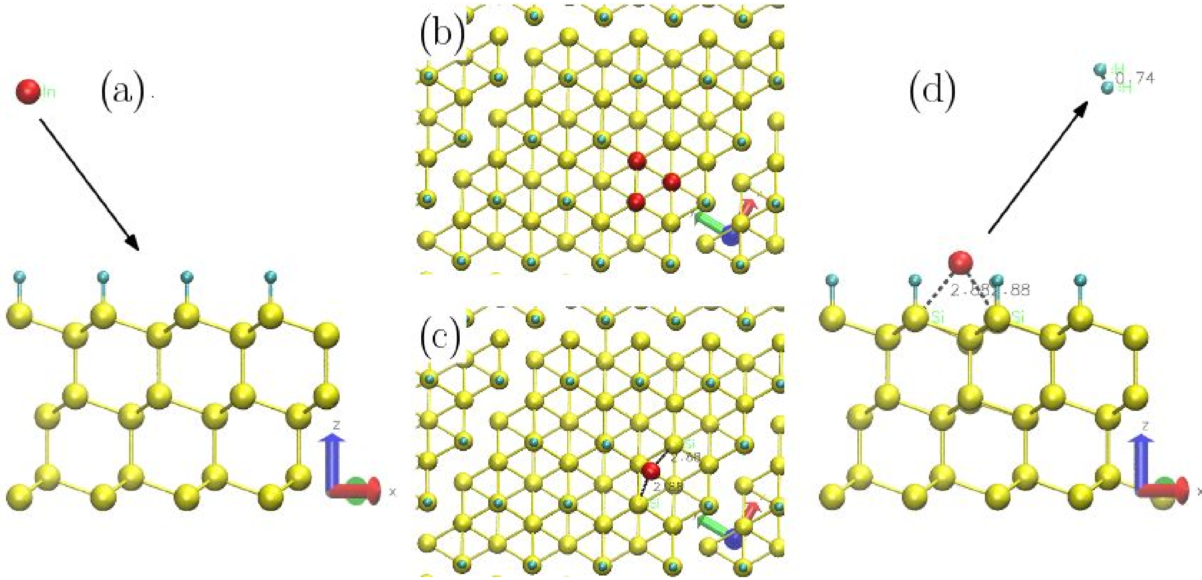

Figure 5.6: (a) and (d) represent the initial and final stages of reaction $R1$ (projection along <111>); (b) is the overlapping of three starting configurations while looking for the In stable positions inside the area freed from H; (c) is the overlapping of the three relaxed configurations corresponding to the three states shown in image (b).

Config. I	$\Delta E(R_2)\,[eV]$	notes
topx2	2.09	two In bound together
b3Ax2	2.07	two In bound together
b3Bx2	2.67	In remain separated

Table 5.4: Energy differences for $R2$.

For reaction $R2$ the situation is a bit more complicated because many configuration should be tested in order to explore all the possible way in which the two In atoms could be placed on the surface. However, within the tried ones, the phenomenology is quite the same as $R1$: if the two In are placed close to the center of the freed area they get close and bound to each other and to silicon matrix (Tab. 5.4, case 1 and 2); instead, if they are a further that 5 angstrom, near the edges of the freed area, they bound only to the closest Si atom and are not able to join each other toward the center (Tab. 5.4, case 3). This highlights once again the presence of a weak potential barrier that allows the existence of metastable states at the freed area border. In particular, for the two more stable cases, the final configurations are slightly different in the In dispositions, but both the $In - Si$ bond length (2.78 Å) and the $In - In$ bond length (3.38 Å)

are the same. Still, the reaction is not energetically favorable for the system.

Config. I	$\Delta E(R_3)\,[eV]$	notes
b3Bmid	-0.44	stays at b3Bmid
topmid	-0.44	goes to B3Bmid

Table 5.5: Energy differences for $R3$.

Regarding the last of our supposed reactions, $R3$, the two considered In configurations relax to the very same final one (Fig. 5.7 (b) and (c)). Moreover, we can see from Tab. 5.5 that the ΔE is negative, thus the reaction brings to a lower energy state compared to starting one. This is probably related to two reasons: the first is that the In that attaches to the surface has the possibility to form three bonds with the underlying Si atoms, thus being in the natural oxidation state $+3$; the second is that also the other In, leaving as an InH_3, has three stable bonds of $-2.38\,eV$ each, thus the molecule brings a heavy favorable factor to the ΔE computation. The $In - Si$ bond length results 2.80 Å that is close to the values obtained for the stable positions of other reactions ($R1 \rightarrow 2.88$ Å, $R2 \rightarrow 2.78$ Å). To totally exhaust the $R3$ investigation, also the other three possible configurations at the freed area border should be explored. However, with the acquired knowledge from the other reactions, we can assume that these, once relaxed, bring to metastable states that, if perturbed towards the minimum energy one, fall there too. Moreover, if such metastable configurations exist they leave at least one Si atoms with unbound electrons, as happens for $R1$.

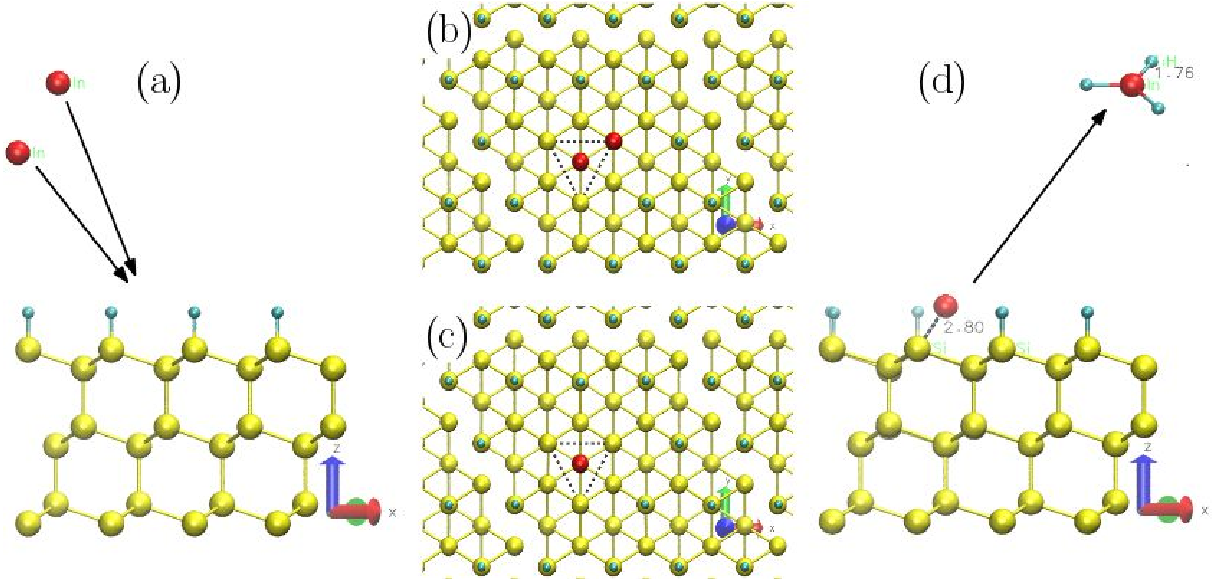

Figure 5.7: (a) and (d) represent the initial and final stages of reaction $R3$ (projection along <111>); (b) is the overlapping of two starting configurations while looking for the In stable positions inside the area freed from H; (c) is the overlapping of the two relaxed configurations corresponding to the two states shown in image (b). Dotted lines are just an help for the eye to visualize the three Si from which H atoms have be removed.

5.3 The As-terminated $Si(111)$:1x1 surface

The As-term surface has been investigated with the same approach used for the H-term surface: the first step is to find the adatoms stable positions and the associated adsorption energy E_{Ads}. In this case, the only adatom studied for now is the In. The interesting starting position are the same as before (**b2**, **b3A**, **b3B**, **top**) with the only difference that their definitions are now referred to the As positions instead of the H ones[3].

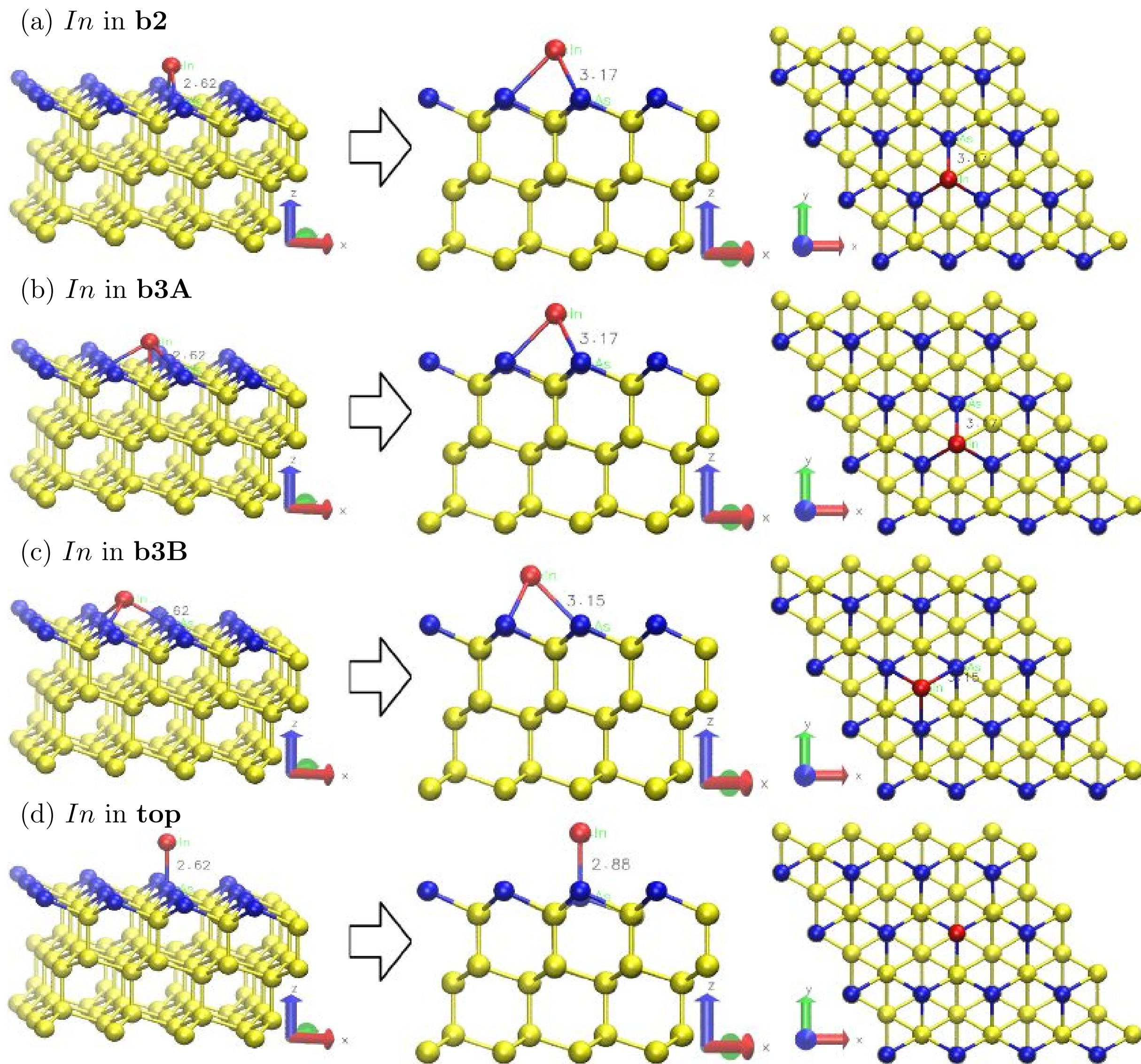

Figure 5.8: Yellow balls = Si, blue balls = As, red balls = In. Investigation of the stable configurations of a single In atom on **As-term** surface. On the left the starting configurations, on the right the relaxed ones looked from <110> and <111> directions. Numbers are the $In-As$ bond lengths in Å.

[3]This is just a trivial difference that concerns only the definition: the As positions are axially the same as before with respect to the Si lattice

Config. I	$E_{Ads}(In)\,[eV]$	$In - As$ dist. [Å]	note
b2	-1.60	3.17	goes to b3A
b3A	-1.60	3.17	stays in b3A
b3B	-1.58	3.15	stays in b3B
top	-1.24	2.88	stays in top

Table 5.6: Adsorption energy for single In on As-term surface and $In - As$ interatomic distance.

By looking at Fig. 5.8 it is clear that, among the four explored configurations, only the **b2** is unstable and relaxes to **b3A**. In all the other cases, the In only adjust its bond length with the underlying As by changing its z coordinate. Furthermore, as it is reported in Tab. 5.6, in each case the In interaction with the As surface is favorable and offers a negative adsorption energy, while the interatomic distance is always bigger then the one in bulk $InAs$ (2.62 Å). This big discrepancy is for sure related to the fact that there are too many electrons in each configuration: in **b3**, three As tend to share their electron pair with a single In, therefore there are 6 electrons for a single In; in **top**, the In can not share its electrons with the three other As that there would be in a bulk $InAs$. The minimum energy is obtained in the **b3A** configuration, however just a small gap separates it from the **b3B** one. At this point, because so many stationary positions are found, it is interesting to study the energy barriers that separates them. In order to do this, we used the Nudged Elastic Band (NEB) that is a script developed for VASP by the University of Texas. In simply words, NEB is a method for finding saddle points and minimum energy paths between two known stable or metastable states. The method works by optimizing the energy of an arbitrary number of intermediate states (images) which form a path in the parameters space between the initial state and final one. The calculation has the characteristic that each image has the same distance in the parameters space from the neighboring ones. This is granted by adding spring forces along the band between images and by projecting out the component of the force due to the potential perpendicular to the band. In our case we want to find such paths between the positions **b3A**, textbfb3B and **top**. Furthermore, because in first approximation only the In is moving, we can visualize the calculated paths by superimposing all the intermediate images found by NEB. This is indeed what is shown in Fig. 5.9 where the paths are like photos taken with a long exposition time. By taking the energy calculated for each image, it is possible to represent the energy barrier between the starting and final configurations as reported in Fig. 5.10. Before commentating them, it has to be noticed that in such graphs in x axis there is only the number of image, and not the distance of the In relatively to the starting position. This is because the path drawn by the In is not perfectly straight, but it slightly bends. Despite this, the In has an approximate distance with itself in the neighbor images of 0.24 Å and each image can be thought to be as much far from the previous

and the next one. Therefore, a rough estimation of this barriers thickness is $2.2 - 2.4\,\text{Å}$. From these curves we can conclude that the **top** position is an unstable stationary state. Instead, positions **b3A** and **b3B** are separated by a small barrier around $0.08\,eV$ that is so small that thermal excitation can make the In travel from one spot to the other without huge hindrance.

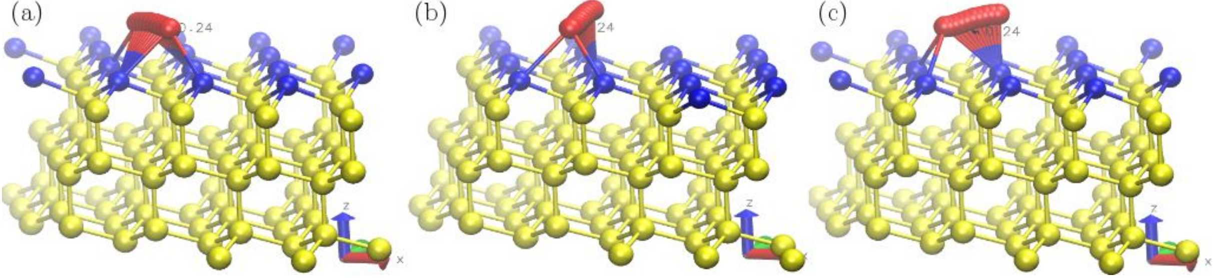

Figure 5.9: Superimpositions of the images calculated by NEB between: (a) **b3A-b3B**; (b) **b3A-top**; (c) **b3B-top**.

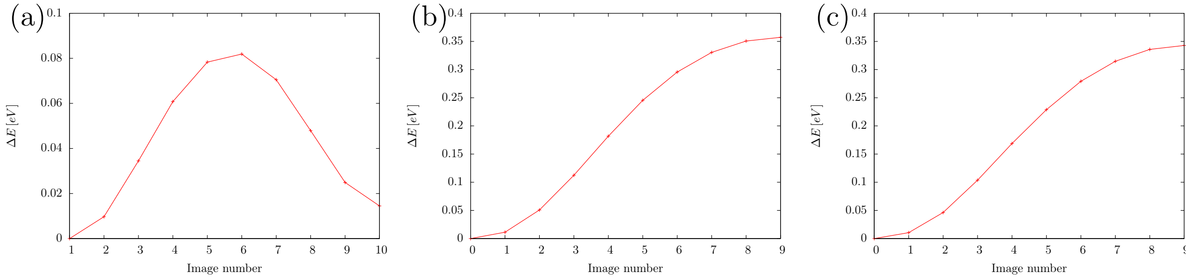

Figure 5.10: Energy barrier between two position found by collecting NEB images energies between: (a) **b3A-b3B**; (b) **b3A-top**; (c) **b3B-top**. The ΔE is calculated by subtracting the energy of the most stable state.

Having acquired a full knowledge about the behavior of a single In on the As-surf, we proceeded our investigation by considering how two or more In interact within different dispositions. The objective is to study how the interaction energy (E_{int}) of two In varies in function of the their distance. Before getting into the quantitative details, a clarification has to be made upon the definition and meaning of such quantity. In vacuum, the interaction energy between two particles is defined as the amount of energy necessary to separate with infinite distance the two bodies, thus it is related only to their atomic potential and distance. Instead, if the bodies are located on a surface, it is defined as the energy that is necessary to spend to bring them at infinite distance while keeping them on the surface. If we define the general formula for the adsorption energy of a given number N of atoms like:

$$E_{adsXN} = E_{\text{N adatom config.}} - E_{\text{Relaxed surf.}} - N \cdot E_{\text{Adatom ref.}} \tag{5.1}$$

where $E_{\text{N adatom config.}}$ is the total energy associate to the configuration with N adatom on the sur-

face, $E_{\text{Relaxed surf.}}$ the total energy of the surface before introducing the adatoms and $E_{\text{Adatom ref.}}$ the energy in vacuum of the single adatoms, the formula associated with the definition of interaction energy for two adatoms is:

$$\mathbf{M1}: E_{int} = E_{adsX2} - 2 \cdot E_{adsX1} \tag{5.2}$$

$$= E_{\text{2 adatom config.}} + E_{\text{Relaxed surf.}} - 2 \cdot E_{\text{1 adatom config.}} \tag{5.3}$$

We can see that the formula on the second line perfectly mirrors the given definition of interaction energy because:

$$E_{\text{Final state}} = E_{\text{2 adatom config.}} + E_{\text{Relaxed surf.}}$$

$$E_{\text{Starting state}} = 2 \cdot E_{\text{2 adatom config.}}$$

With this calculation method, that we will call $M1$, the interaction energy not only includes the contribution that comes from the interaction between the two adatoms in presence of the surface, but also the contribution that comes from the deformation of the surface due to their presence and the contribution that comes from the change of their position (different adsorption energy compared to one adatom config.). Although this scheme is perfectly licit and correct, if the deformation energy and the change in the single adatom adsorption energy have the same order of magnitude of the interaction energy between the adatoms, they can also dominate and give apparently inexplicable trends for the quantity defined by $M1$. Because of this, we will give now another different definition to the interaction energy in order to extract the contribution that involve only the adatoms. With another point of view, the total energy of the final configuration with two adatoms has several contributions that, in first approximation, can be summarized in: cost of the perfect surface ($E_{\text{Relaxed surf.}}$), cost of the interaction between single adatoms and substrate (E'_{ads})[4], cost of the surface deformation ($E_{\text{Deformation}}$) and cost of the adatoms interaction (E'_{int}). To extract only the last term we can freeze the system in the final configuration ($E_{\text{2 adatoms config.}}$), not allowing any atom to relax, and remove adatoms to define new states:

$$\text{Remove only one adatom}: E_{rem1} = E_{\text{2 adatoms config.}} - E'_{int} - E'_{ads}$$
$$= E_{\text{Relaxed sur.}} + E_{\text{Deformation}} + E'_{ads}$$
$$\text{Remove both adatoms}: E_{\text{Deform. surf.}} = E_{\text{2 adatoms config.}} - E'_{int} - 2 \cdot E'_{Eads}$$
$$= E_{\text{Relaxed surf.}} + E_{\text{Deformation}}$$

It easy to see that, if we define E_{rem1} and E_{rem2} respectively as the energies of the frozen states in which one In or the other are removed, then we can obtain an estimation of the interaction

[4]The apex $'$ underlines that now the definition is different from before: it does not take into account the deformation cost of the surface and it is referred to the relaxed position after two bodies interaction.

energy using:

$$\mathbf{M2}: E'_{int} = E_{2\text{ adatoms config}} + E_{\text{Defom. surf.}} - E_{rem1} - E_{rem2}$$

It is interesting to notice that, if the surface deformation induced by the presence of two adatoms is small and if the two adatom do not change significantly their single adsorption energy, then the two models give exactly the same interaction energy estimation. Finally, it is worth noting that the small surface 4x4 used for the single In calculations was not enough for this part of the work because In where reacting to each other presence multiple times due to limited PBC. Therefore, we used the 8x8 substrate that keeps a minimum distance of 24 Å between one In and the "replica" of the other in the closest periodic box.

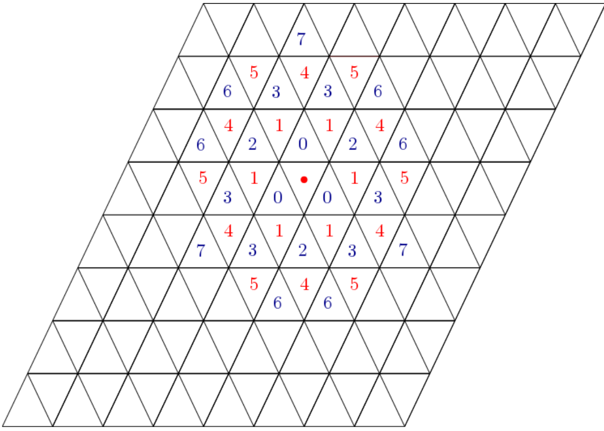

Figure 5.11: The schematic represents how the **b3** position closest to a starting point (red dot) can be grouped in term of progressive distance (the number) and position type (color related to **b3A** or **b3B**).

The investigation was carried out by placing the two In in all the closest combinations of the two possible stable configurations, **b3A** and **b3B**. With reference to Fig. 5.11, given a starting **b3** position (that can be of type **A** or **B**), all the other position can be grouped according to their progressive distance (increasing number) and their type (red if the same, blue if different). In the considered range of less than 9 Å, this approach give us a total of eleven combinations, 5 **AB**, 3 **AA** and 3 **BB**[5]. In all these cases, not a single time the relaxation causes one of the In to exit from the minimum valley in which it is placed. Instead, they only move closer or further from each other in function of their distance while staying inside of their minimum valley. The situation is clearly shown if Fig. 5.12 and is quite predictable: in first near neighbor position they are too close and get further; in second near neighbor position they are able to establish a bond and they get closer; in all the other cases they are slightly repulsed by an amount that decreases with increasing distance. In particular, in this graph not a significant difference can be found between type **AA** and **BB** combinations because the final distance is mainly related to the potential barrier that defines the minimum valley and a very small difference exist between the two cases (Fig. 5.10). The opposite happens when looking at the interaction energy reported in Fig. 5.13: green and blue points (**AA** and **BB** combinations)

[5] For symmetry, **AA** and **BB** combinations are at the same distance.

that are at the same distance, differ in the interaction energy for even more that $0.05\,eV$ which is an important quantity if compared to the range in which it varies ($0.3\,eV$). Aside from this discrepancy in the behavior of **AA** and **BB** combinations, we can also notice how methods $M1$ and $M2$ give strongly different values for In at close range, whereas they differs for less than $0.02\,eV$ when the two In are further than $4\,\text{Å}$. As previously explained, this is related to the influence on method $M1$ of surface deformation and adsorption energy change of the single In: these two contributions become lesser and lesser important the further the two In are.

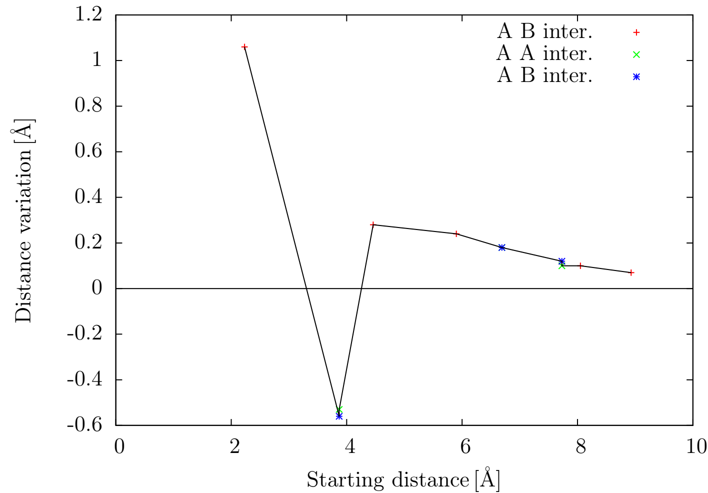

Figure 5.12: Variation of distance between two In in function of their starting distance on As-term surface. Points have different colors according to the position type combination; the line is plotted to help the eye follow points along increasing starting distance.

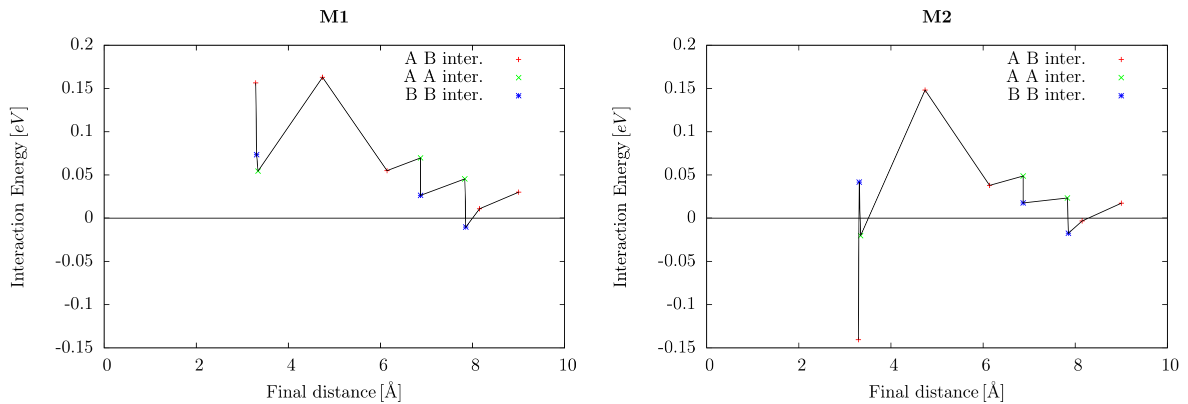

Figure 5.13: Graphs of interaction energy vs final distance of two In atoms on As-term surf: on the left method $M1$, on the right method $M2$. Points have different colors according to the position type combination; the line is plotted to help the eye follow points along increasing final distance.

Going back to the physical meaning of the value estimated with $M1$, because it represents the energy difference between a final configuration in which In are interacting and a starting

configuration where they are separated, it tells us which of the two states is less energy expensive for the system. Aside from one **BB** configuration, E_{int} in the $M1$ graph is always positive, thus the system requires energy to form a bonded pair of In (around $0.05\,eV$).

Config. I	$E_{int}\,[eV]$	$In - In$ dist. [Å]	$In : In : In$ angle
a1	-0.12	$3.22 - 3.27$	138°
topl	-0.20	$3.26 - 3.26$	165°

Table 5.7: Data of the favorable configurations with three In reported in Fig. 5.14.

Instead, when a third In is introduced on the surface in a position neighbor to the others two, some configurations that are energetically favorable exist, as those shown in Fig. 5.14. The interesting data relative to these configurations are reported in Tab 5.7. In particular, the associated E_{int} is calculated with the immediate extension to N adatoms of method $M1$:

$$E_{int} = E_{adsXN} - N \cdot E_{AdsX1} \tag{5.4}$$

It is sufficient to substitute formula 5.1 in it to verify that it is coherent with every definition and interpretation given to $M1$ up to now. It is interesting to notice that both these configurations have In closer to **b2** position, more than to the **b3** one, whereas the opposite happens for all others that are not energetically favorable (and which are not reported in details here). The conclusion is that the **b3** position is progressively losing its importance as an energy minimum as the In interactions and bonding become more relevant.

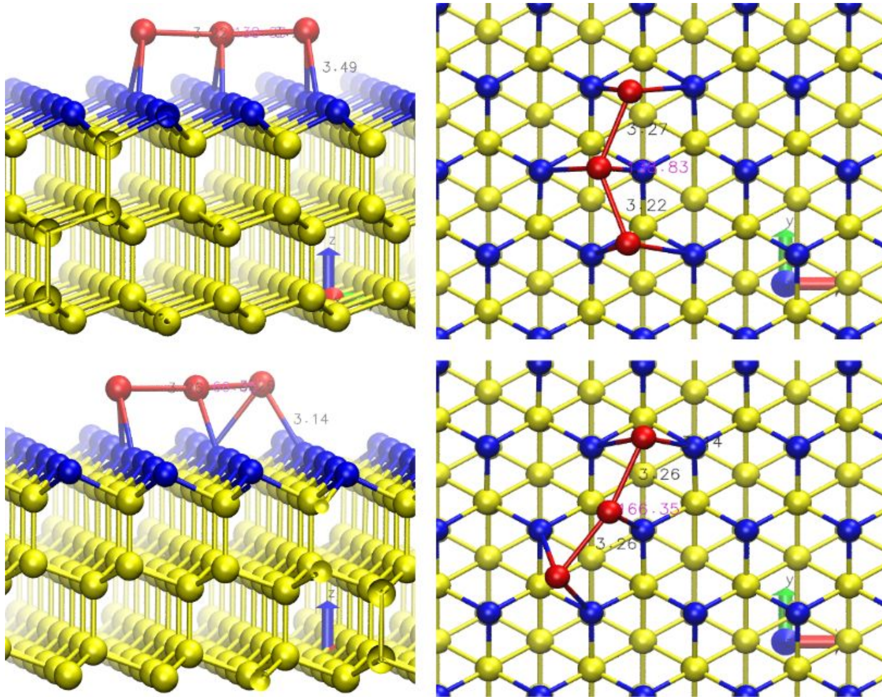

Figure 5.14: Relaxed configurations with three In which are energetically favorable: left and right images are the same configuration seen from near <110> and from <111> respectively.

Chapter 6

Conclusions and prospectives

Overall, with the experiments carried on up to now, we got few remarkable achievements. First of all, the vertical yield for NWs grown on unpatterned substrates exceeds 95%, although big crystalline islands still form on the surface hindering higher NWs density. To obtain this result we showed that it is necessary to combine all the pre-treatments and that the H plasma has an enhancing effect on NWs density if it is applied with the substrate at low temperature. During this analysis, we also clarified that the H plasma must have a chemical/reconstruction effect on the surface, but a further investigation is required to establish if it has, or not, a limited effect on oxide/contaminants removal. In order to ascertain the matter, a single experiment with another H plasma treatment will be performed on the very same sample with $17\,nm$ of thermal oxide on it. Instead, another series of samples will be grown to identify the temperature interval in which the H plasma gives positive effects. With this two further information, it will be more clear which is the exact effect of the plasma on the surface. Then, we have seen that the NWs obtained within the best sample have diameters that largely span between $20\,nm$ and $100\,nm$ and also that their length is totally heterogeneous. The reason for this is linked to the nucleation time that, in absence of a catalyst, is random and can happen at any time during the deposition stage. Moreover, competitive growth of random positioned structures with random nucleating time helps to maintain discrepancies. To overcome this obstacle, I propose to modulate In and As fluxes at the begin of the deposition in order to slow down the growth of already existing NWs, and give more time to the system to nucleate others. I strongly believe that an initial transient exists in which the majority of NWs nucleate and, if this transient is somehow controlled, as with the technique proposed, then the NWs geometrical properties would be more homogeneous. It is also worth noting that the length of the NWs is directly proportional to the growth time and also the diameter has a slight dependence from it; thus it is possible to obtain even smaller

NWs by reducing the deposition duration. Aside from this investigations, to conclude this part of the work, the growth parameters could be explored more in details, for example by verifying if the islands density can be reduce by variation of the V-III ratio, or by increasing the growth temperature.

A second achievement is constituted by the answers obtained through the TEM characterization. We successfully verified that the NWs do not have dislocations if they are short enough to not be affected by the strain induced by the carbon deposition. Instead, the upper part of the NWs presents twin planes and crystal phase alternation. Moreover, we have seen that the NWs have crystal planes that orderly stack from the Si ones across all their section, confirming that no oxide is remaining on the surface after the pre-treatments. At the same time, it was not possible through the STEM technique to distinguish whether if the first layer of the NW is constituted by In or As. However, the EDX analysis strongly suggests that the nucleation starts with the latter, thus an As reconstruction of the surface is needed to yield vertical NWs. Because the main obstacle for this part of the analysis was the presence of the Si oxide layer all around the NW base, I propose that, after the growth and before taking out the sample from the MBE, a coating layer could be deposited in order to protect the first nanometers of the NW and the surface from re-oxidation. This strategy would allow to have a better look at the substrate-NW interface if an appropriate material like carbon could be evaporated *in-situ*. Such approach would be even more valuable if the patterned sample were going to be characterized with TEM: coating the holes bottom would allow to verify the proper and homogeneous removal of the oxide.

Regarding the study of the growth on the patterned surface, still a lot of work has to be done. So far we got evidences that the used cleaning procedure yields vertical NWs and that holes are better spots for NWs nucleation the bigger their diameter is. Further experiments are required to find the best growth parameters and these could also show how to decrease the NWs diameter that, for now, has resulted to be around $45\,nm$. Once this has been done, a precise statistic analysis has to be carried out about diameter and length of the NW in function of holes diameter and pitch. In particular, we already confirmed a clear monotonic dependence of the firsts with the holes diameter, but the real physical reason behind it has not been exposed yet. As already explained, this could be related to the fact the big holes favor an early nucleation, thus giving more time to the NWs to grow taller and larger, or it could be that the bigger the holes the more material is available for each NW. To understand which of these two phenomena is more relevant, I suggest to design a pattern with more pitches and just one holes diameter and study

how the competitive growth changes in function of them. In particular, this series of samples would allow to study the critical NW density that I define with the following reasoning: on the unpatterned surface, after a transition time needed to reach equilibrium, the number of nucleated NWs must remain constant, thus yielding a precise density of NWs. In the case of the patterned substrate, a similar quantity must exist, but it is hidden by the presence of the oxide: NWs can nucleated only in the holes, thus they can have at maximum the same density (aside from the trivial case where two NWs nucleate in the same holes, that is not of our interest). However, when the holes are too close, the competitive growth and material recollection dominates, leaving some holes empty and this would define an intrinsic and critical NWs density under which can not be surpassed the B-U approach due to the formation mechanism itself.

To conclude, the simulation part has provided us many useful information, although it is not sufficient yet for our purpose of developing a kinetic Monte Carlo of nucleation. Firstly, we learned that the In has a favorable interaction with the H-term surface and that a chemical reaction can happen with the terminating hydrogens without any cost for the system. However, the possibility for such a reaction to happen has not been established and it could be interesting to apply the NEB method to calculate the associated barrier. Instead, the As interaction with such surface was not analyzed in depth for two reason: the first is that the As arrives on the surface as an As_4 (and in this case the single atom interaction is highly unfavorable); the second is that we experimentally know that the outcome of such interaction is a complicated transition between H-term Si(111):1x1 to Si(111):7x7 to As-term Si(111):1x1. Instead, great attention is posed on the latter configuration: a detailed analysis has been carried out about the In behavior on the As-term surface because this is the most probable configuration from which nucleation is starting. We found the equilibrium positions of a single In and we saw that it alone is not stable in the direction of epitaxial growth. Adding another In gave us the possibility to study the interaction energy with two different approaches which told us that the In are bonding at small distances, but the system has to pay an energy toll in the process. Adding one more In proved that with only three or less In it is not possible to obtain the $InAs$ growth direction, however the structure that are forming are not strongly related to the original stable positions anymore. Therefore, the formation of a crystal layer by epitaxial deposition is the result of a complex collective interaction between atoms and further simulations are required to find a configuration in which the top position is stable. After finding the minimum structure which favors the epitaxial direction, it will be interesting to study the behavior of a single As on itself and eventually the $In - As$ interaction on it. Adding this data to the ones already collected

will allow to implement an efficient kinetic Monte Carlo simulation that then could be enhanced including the facets effect.

Appendix A

H plasma cell starting procedure

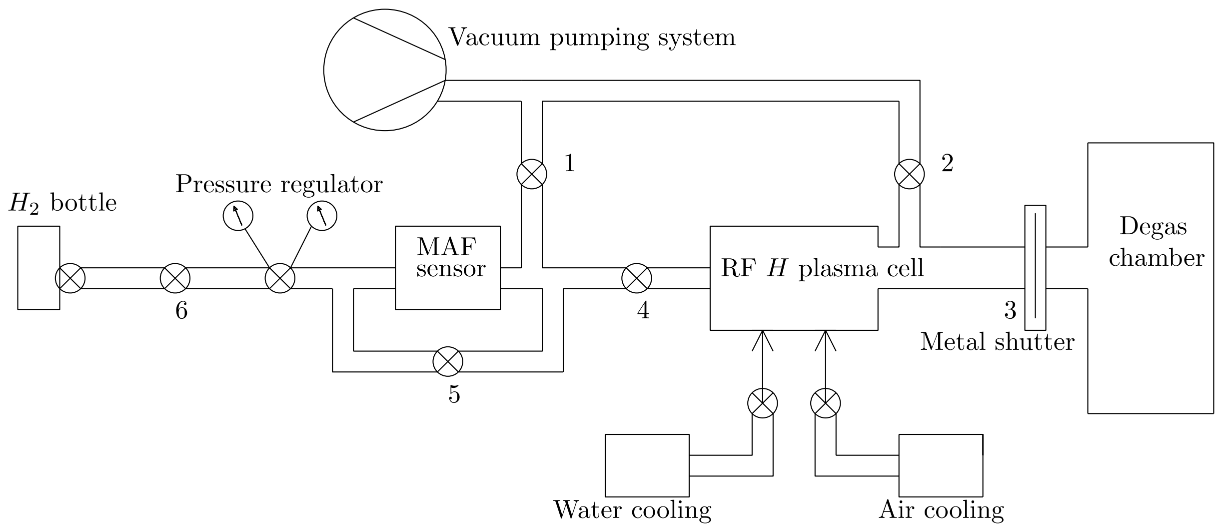

Figure A.1: Radio Frequency H plasma cell schematic.

To start the plasma cell a precise procedure has to be followed (ref. to A.1). Two hours before ignition, the vacuum system has to be turned on to pump all the pipelines and the cell, opening all valves but the metal shutter 3 and the H_2 bottle. When the system reaches a pressure below $10^{-3}\,Pa$, it can be fed with hydrogen: first, the bypass 5 and the pressure regulator have to be closed and the two cooling systems have to be started; then Mass Air Flow control unit has to be started and set to $1\,SCCM$; at this point the H_2 can be relased from the bottle up to the pressure regulator carefully reaching a pressure of $30\,bar$. The pressure regulator valve has to be manually set so that the pressure before the MAF is around $0.5\,bar$. Closing valve 1 will now allow the hydrogen to flow trough the RF cell. At this point the Radio Frequency generator and the plasma optic sensor control unit can be started. The power delivered by the generator has to be slowly risen to $225\,W$ and the valve 2 has to be closed to let the plasma accumulate inside

the cell while absorbing the radiated power. When the optic sensor reveals that the luminosity inside the cell changes, the plasma is turned on and the valve 2 has to be opened again to get to a steady H plasma flux. To start the treatment it is enough to open the metal shutter 3 so that the plasma will flood inside the degas chamber.

When the treatment is finished, metal shutter 3 has to be closed and the radiated power has to be slowly reduced to $0\,W$. After the plasma luminosity drops to 0, valve 4 can be closed and valve 1 opened again. At this point hydrogen can be still present in significant quantity between the closed bottle and the pressure regulator. This hydrogen has to be carefully pumped away leaving the line empty and clean. To do this, the bypass 5 has to be opened checking that the pumping system is not flooded with too much hydrogen. When the full setup reaches again a pressure of $10^{-3}\,Pa$, all valves might be closed and the pumping and cooling systems shut down, thus leaving the system in a safe state.

Appendix B

TEM sample preparations

B.1 Holey carbon grid

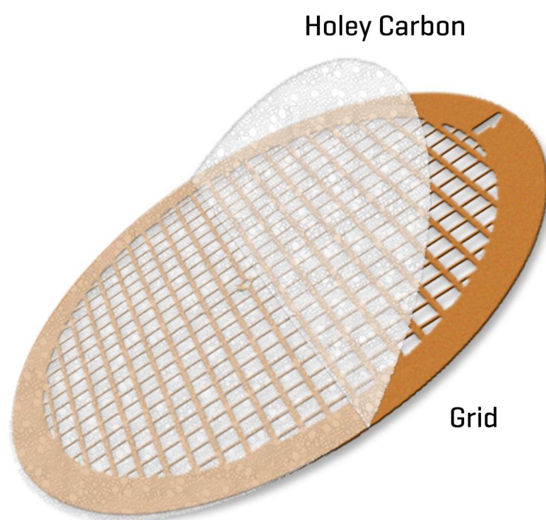

Figure B.1: Holey carbon grid schematic.

A simple, fast and cheap preparation to observe NWs at TEM consists in scratching them on a specialized support called holey carbon grid. With reference to Fig. B.1, this grid is made out of copper and a ultra thin film of carbon is used as a net trap to keep the wires in place once scratched. The carbon film is covered with random holes, from which the name "holey", and this allows to observe the NWs as suspended in nothing, thus eliminating the background electron scattering that would be present if a solid support were used. However the drawbacks of this technique are at least two: in first place the NWs tend to bend on the grid, thus the focusing procedure is more complicated and some strong contrasts can emerge on the image due to the local strain and deformation; then the NWs are removed from the surface so that the interface with the surface can not be investigated.

B.2 Focused Ion Beam Lamellae

In this procedure a SEM equipped with a Focused Ion Beam (FIB) and a peculiar manipulator is used to coat, dig and extract from the sample a thin blade called Lamella that is than fixed to a dedicated holder to perform TEM. Compared to the previous preparation, this is expensive, time consuming and requires a specialist to be performed.

The preparation requires several steps that are shown in Fig. B.2 and can be summarized in the following procedure:

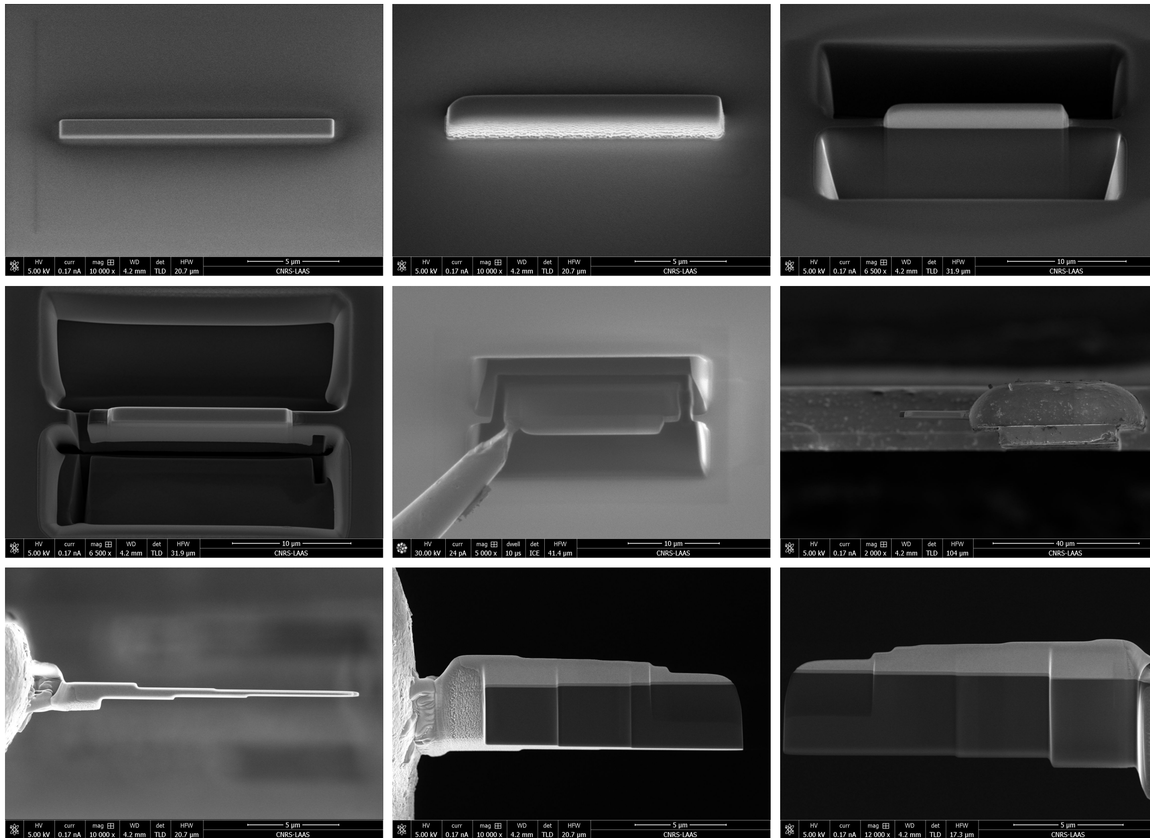

Figure B.2: FIB lamella preparation procedure.

1. A thin carbon film (some tenths of nm) is deposited using and electron beam to protect a selected area of the surface from the film deposited at step 2 that would alter the TEM investigation;

2. Then around one micrometer of platinum is deposited using the ion beam over the carbon film to shield the sample from the after coming digging;

3. Gallium is used to dig by physical sputtering two big holes that start to define the lamella;

4. More precise cut are performed to quite totally detach the lamella from the substrate; just

a small bridge is left to connect it to the substrate;

5. A micrometric manipulator is weld on top of the lamella to hold it while the remaining bridge connecting it to the substrate is cutted;

6. The lamella is transfered and weld again on a specific TEM sample holder;

7. The lamella is sharpened in an iterative procedure using the ion beam taking care that the protective Pt is not completely removed otherwise the surface itself would be altered and eroded;

8. In the end, picture of the lamella from both sided are taken to define the best zones in which is favourable to work with the TEM.

With this procedure the unaffected surface can be analyzed at the TEM (film thickness, strain and uniformity characterization). Moreover, if some structures are present on the surface, their interface can be studied in details. However, in the case the structures are really high, particular attention has to be paid in the carbon and platinum deposition. Indeed, the platinum has absolutely to not cover the sides of the structures, otherwise the electrons would be heavily affected by it and a poor or and incomplete image could be taken afterward.

In our case, with quite tall NWs (over $1\,\mu m$), before the FIB carbon deposition, a supplementary carbon deposition has been performed with an external evaporator because it would have required too much time to deposit a significant amount of carbon with the electron beam.

Appendix C

Silicon oxide patterning

The procedure used to created the oxide patterned mask on the Silicon wafer is a standard one based on Electron Beam Lithography (EBL):

1. An oxide layer of $20\,nm$ is thermally grown on a brand new Si(111) wafer.

2. The wafer is coated using a spinning rotor with $40\,nm$ of Poly Methyl Methacrylate (PMMA) that is a positive photoresit.

3. The PMMA is impressed using an EBL system which moves the beam according to a planned schematic and at a speed that depends on the set electron flux and dose.

4. The PMMA is developed immersing the wafer for $12\,s$ in a pot filled with Methyl Isobutyl Ketone (MIBK). This is the hardest step to reproduce because it is done manually. The sample is then cleaned with Isopropyl Alcohol.

5. The sample is etched with a plasma composed by $50\,SCCM$ of CHF_3 and $3\,SCCM$ of O_2 which leaves holes and cleaned patches on the silicon oxide according to the zones exposed by the impression-developing steps. The PMMA leftovers are removed using acetone.

6. All the procedure is calibrated so that the opened holes still have a $3\,nm$ oxide at their bottom in order to protect the surface from random and not controlled reoxidation. Thus, before introducing the sample in the MBE chamber, it is etched with a calibrated dose of HF. In the end the result is a patterned oxide with a thickness of $17\,nm$ and holes perfectly cleaned from any oxide.

Appendix D

Simulation theory and approximations

In this appendix I present the basic knowledge about the quantum theory that is used by VASP to perform its calculations. The aim is to give just a general idea about the approximations that are required to solve the system hamiltonians, therefore almost all the mathematical steps needed to reach a certain result will be skipped. If the reader is interested in going deeper in the calculus, a good reference is found in [42] by Haynes.

If we neglect the spin, the system is simply composed by nuclei and electrons that interact via Coulomb force. The associated hamiltonian is made by three contributions: the nuclei kinetic and self interaction term ($\hat{H}_n$), the electrons kinetic and self interaction term ($\hat{H}_e$), an the nuclei-electron mutual interaction term (V_{ne}):

$$\begin{aligned}
\hat{H} =& \hat{H}_n + \hat{H}_e + V_{ne} \\
\hat{H}_n =& \sum_{I=1}^{N_n} -\frac{\hbar^2}{2M_I}\nabla^2_{R_I} + \frac{1}{2}\sum_{\substack{I,J=1\\ I\neq J}}^{N_n} \frac{Z_I Z_J e^2}{4\pi\epsilon_0}\frac{1}{|\mathbf{R}_I - \mathbf{R}_J|} \\
\hat{H}_e =& \sum_{i=1}^{N_e} -\frac{\hbar^2}{2m_e}\nabla^2_{r_i} + \frac{1}{2}\sum_{\substack{i,j=1\\ i\neq j}}^{N_e} \frac{e^2}{4\pi\epsilon_0}\frac{1}{|\mathbf{r}_i - \mathbf{r}_j|} \\
V_{ne} =& -\frac{1}{2}\sum_{I,i=1}^{N_n,N_e} \frac{Z_I e^2}{4\pi\epsilon_0}\frac{1}{|\mathbf{R}_I - \mathbf{r}_i|}
\end{aligned}$$

In a non relativistic framework, the well known final postulate of quantum mechanics states that the state vector $\Psi(\{\mathbf{R}_I\},\{\mathbf{r}_i\},t)$ of the system evolves according to the time-dependent Schrödinger equation:

$$\hat{H}|\Psi\rangle = i\frac{\partial}{\partial t}|\Psi\rangle$$

However, if we are interested only in the stationary states, the following separation of the variables

is made by introducing the separating variable E:

$$\begin{aligned}\Psi(\{\mathbf{R}_I\},\{\mathbf{r}_i\},t) &= \tilde{\Psi}(\{\mathbf{R}_I\},\{\mathbf{r}_i\})\Phi(t)\\ \hat{H}\tilde{\Psi}(\{\mathbf{R}_I\},\{\mathbf{r}_i\}) &= E\tilde{\Psi}(\{\mathbf{R}_I\},\{\mathbf{r}_i\})\\ i\frac{\mathrm{d}}{\mathrm{d}t}\Phi(t) &= E\Phi(t)\end{aligned}$$

To find the eigenfunction of the hamiltonian $\tilde{\Psi}(\{\mathbf{R}_I\},\{\mathbf{r}_i\})$, the problem is further separated using the Born-Oppenheimer approximation. Physically speaking, the reasoning behind this approximation is that the forces on both electrons and nuclei due to their electric charge are of the same order of magnitude, and so the changes which occur in their momenta as a result of these forces must also be the same. Therefore, one might assume that the actual momenta of the electrons and nuclei were of similar magnitude. Thus, because of the highly different mass between nuclei and electrons, on the typical time-scale of the nuclear motion, the electrons will very rapidly relax to their instantaneous ground-state configuration. This means that we can assume that the nuclei are stationary, find the electronic ground state in a given nuclei configuration and then solve the nuclear motion after calculating the system energy. All the argument can be confirmed by substituting into the hamiltonian stationary equation the following form for its eigenfunction:

$$\tilde{\Psi}(\{\mathbf{R}_I\},\{\mathbf{r}_i\}) = \Psi(\{\mathbf{r}_i\};\{\mathbf{R}_I\})\,\Phi(\{\mathbf{R}_I\})$$

where $\Psi(\{\mathbf{r}_i\};\{\mathbf{R}_I\})$ is a wafe-function only in the $\{\mathbf{r}_i\}$ that satisfies the time-independent Schrödinger equation for the electrons in a static array of nuclei in position $\{\mathbf{R}_I\}$. Neglecting the non-adiabatic terms, the problem is reduced to solve the system[1]:

$$\left[-\frac{1}{2}\sum_j \nabla_j^2 - \sum_j\sum_J \frac{Z_J}{|\mathbf{r}_j-\mathbf{R}_J|} + \frac{1}{2}\sum_{j,k;\,j\neq k}\frac{1}{|\mathbf{r}_j-\mathbf{r}_k|}\right]\Psi(\{\mathbf{r}_i\};\{\mathbf{R}_I\}) = \varepsilon_e(\{\mathbf{R}_I\})\Psi(\{\mathbf{r}_i\};\{\mathbf{R}_I\})$$

$$\left[-\sum_J \frac{1}{2m_J}\nabla_J^2 + \varepsilon e(\{\mathbf{R}_I\}) + \frac{1}{2}\sum_{J,K;\,J\neq K}\frac{Z_J Z_K}{|\mathbf{R}_J-\mathbf{R}_K|}\right]\Phi(\{\mathbf{R}_I\}) = \varepsilon\Phi(\{\mathbf{R}_I\})$$

From this point on, it is assumed that the electrons respond instantaneously to the nuclear motion and always occupy the ground-state of that nuclear configuration. Varying the nuclear positions maps out a multi-dimensional ground-state potential energy surface, and the motion of the nuclei in this potential can then be solved. In practice Newtonian mechanics generally sufices for this part of the problem, and relaxation of the nuclear positions to the minimum-energy configuration can be performed. Instead, to solve the first equation the variational principle is

[1] Atomic units are used throughout: $\hbar = m_e = e = 4\pi\epsilon_0 = 1$.

used. This states that the expectation value of the Hamiltonian $\langle E \rangle = E| [\Psi]$ is a functional of the wave-function and it is stationary ($\delta E [\Psi] = 0$) when $|\Psi\rangle$ is an eigenstate of $\hat{H}$ of eigenvalue $E [\Psi]$. To calculate the ground state E_0, we can minimize the function $E [\Psi]$ with respect to all the states $|\Psi\rangle$ which are antisymmetric under exchange of particles.

Becuase the $|\Psi\rangle$ is not known, it is has to be guessed and this is what has been done firstly by Hartee-Fock. Their approximation is based on the Slater determinant that grants that the wave-function $|\Psi\rangle$ is antisymmetric, while its single wave-functions have to be determined by the variational principle. However, this method has a bad scaling with the number of the electrons and one of the terms that appears in the final equation, called exchange-correlation, can bring to singularity during the computation. A different resolution method, which consistency is demonstrated by Hohenberg and Khon theorems, is the Density Functional Theory (DFT). If we have an hamiltonian of the generic form:

$$\hat{H} = \hat{T} + \hat{U} + \hat{V}$$

$$\hat{T} = \sum_{i=1}^{N} -\frac{1}{2}\nabla_i^2 , \qquad \hat{U} = \sum_{i=1}^{N} U(\mathbf{r}_i) , \qquad \hat{V} = \frac{1}{2} \sum_{\substack{i,j=1 \\ i \neq j}}^{N} V(\mathbf{r}_i, \mathbf{r}_j)$$

and if we define from the many-body wave-function $\Psi(\{\mathbf{r}_i\})$ the one-body density:

$$\rho(\mathbf{r}) = \langle\Psi| \sum_{i=1}^{N} \delta(\mathbf{r} - \mathbf{r}_i) |\Psi\rangle$$

then the external energy $\langle\Psi|\hat{U}|\Psi\rangle$ and the internal energy $\langle\hat{F}\rangle = \langle\Psi|\hat{T}+\hat{V}|\Psi\rangle$ are both functionals of the local density $\rho(\mathbf{r})$. The immediate consequence is that the ground-state energy of a many-body system is uniquely a functional of the particle density $E_0 = E[\rho(\mathbf{r})]$ and it has its minimum relative to the variation $\delta\rho(\mathbf{r})$ at the equilibrium density $n_0(\mathbf{r})$. The remarkable results of DFT are the existence of the universal functional $F[\rho]$, which is independent of the external potential, and that instead of dealing with a function of 3N variables (the many-body wave-function) we can deal with a function of only three variables (the density). Thus, the complexity of the problem has been much reduced and we note that it now scales linearly with the system-size. The variational problem for Hohenberg-Khon density functional can be summarized in the following formula where we introduce μ as a Lagrangian multiplier to constrain the number of electron to be N:

$$\delta \left[F[\rho] + \int \mathrm{d}\mathbf{r} V_{ext}(\mathbf{r})\rho(\mathbf{r}) - \mu \left(\int \mathrm{d}\mathbf{r}\rho(\mathbf{r}) - N \right) \right]$$

Despite these results, the theorems do not explain how to find the right expression of $F[\rho]$ and

several theories with different types of approximations exist. One of the most used approach is the one suggested by Khon and Sham that map the problem of the interacting electrons system onto a fictitious system of non-interacting "electrons". To do this, they separate the internal energy in three contributions:

$$F[\rho] = T_s[\rho] + \frac{1}{2}\int \mathrm{d}\mathbf{r}\mathrm{d}\mathbf{r}' \frac{\rho(\mathbf{r})\rho(\mathbf{r}')}{|\mathbf{r}-\mathbf{r}'|} + E_{xc}[\rho]$$

in which $T_s[\rho]$ is the kinetic energy of a non interacting gas of density ρ, the second term is the classical electrostatic energy (Hartee-like) and the final term is an implicit definition of the exchange correlation energy. The latter contains both the energy contribution from non-classical interactions and the one from the difference between kinetic energy of non-interacting system and interacting one. The aim of the separation is that the two first terms can be dealt simply while the last term is only a small fraction of the total energy and it can be estimated with further approximations. The easiest of these approximations is the Local Density Approximation (LDA) which evaluates the exchange-correlation energy for each infinitesimal volume $\mathrm{d}\mathbf{r}$ as the value that it would have if the whole space were filled with an homogenoeus gas with the same density as in $\mathrm{d}\mathbf{r}$:

$$E_{xc}[\rho] = \int \mathrm{d}\mathbf{r}\varepsilon_{xc}(\rho(\mathbf{r}))\rho(\mathbf{r})$$

where ε_{xc} is the exchange-correlation energy per electron in a homogeneous electron gas of density $\rho(\mathbf{r})$.

The line of reasoning presented up to now summarizes the fundamental approximations that are needed to face a solvable problem. However, many more approximations and choices have to be made to actually solve the hamiltonian related to the real system. The firs step is to choose a basis of wave-functions that could efficiently describe the one-body density:

$$\rho(\mathbf{r}) = \sum_i^N |\psi(\mathbf{r}_i)|^2$$

This is properly done according to the system nature (metal crystal, semiconductor crystal, etc.), but some possibilities are Plane Waves (PW), Linear Combination of Atomic Orbitals (LCAO) and mixed bases. However, because of the tightly bound states (strongly localized) and the rapid oscillations of the wave functions near the nucleus, these approach would exceed any calculation limit. Therefore, the solution is to introduce the frozen core approximation together with the pseudo-potential method. The former considers the inner electrons as not perturbed from the molecular bonding, thus their states and energy are pre-calculated in an atomic environment and kept frozen in the following calculations. The latter substitute the real

potential between electrons and nuclei with a pseudo-potential that can be different according to the desired constraints; in particular, VASP can use the ultra-soft pseudo-potential or the Projector Augmented Wave (PAW) method.

The scheme of matrix-diagonalization used by VASP and required to perform such calculations can be found at [43].

Acronyms

AFM Atomic Force Microscope

BAG Bayard-Alpert Ionization Gauge

BEP Beam Equivalent Pressure

BF Bright Field

DF Dark Field

DFT Density Function Theory

DIW Deionized Water

DP Diffraction Pattern

EBL Electron-Beam Lithography

EDX Energy Dispersive X-Ray

FET Field Effect Transistor

FIB Focused Ion Beam

HRTEM High Resolution Transmission Electron Microscope

kMC Kinetic Monte Carlo

LDA Local Density Approximation

MAF Mass Air Flow (sensor)

MBE Molecular Beam Epitaxy

ML Monolayer

MOCVD Metal-Organic Chemical Vapor Deposition

MOVPE Metal-Organic Vapor Epitaxy

NEB Nudged Elastic Band

NIL Nano-Imprint Lithography

NW Nanowire

PBC Periodic Boundary Conditions

RF Radio Frequency

RHEED Reflection High Energy Electron Diffraction

SA-MBE Selective Area Molecular Beam Epitaxy

SEM Scanning Electron Microscope

STEM Scanning Transmission Electron Microscope

TEM Transmission Electron Microscope

UHV Ultra High Vacuum

VLS Vapor-Solid-Liquid

VS Vapor-Solid

VSS Vapor-Solid-Solid

WZ Wurtzite

ZB Zincblende

Bibliography

[1] `http://www.intel.com/content/www/us/en/silicon-innovations/intel-14nm-technology.html`.

[2] `http://www.intel.com/content/www/us/en/silicon-innovations/intel-22nm-technology.html`.

[3] Tomioka K., Motohisa J., Hara S., and Fukui T. Control of InAs nanowire growth directions on Si. *Nano Lett.*, 8(3):3475–3480, 2008.

[4] Bakkers E., van Dam J., De Franceschi S., Kouwenhoven L., Kaiser M., Verheijen M., Wondergem H., and van der Sluis P. Epitaxial growth of InP nanowires on germanium. *Nat. Mater.*, 3:769–773, 2008.

[5] Zervos M. and Feiner L.F. Electronic structure of piezoelectric double-barrier InAs / InP / InAs / InP / InAs (111) nanowires. *J. Appl. Phys.*, 95:281, 2004.

[6] Wagner R. S and Ellis. W. C. Vapor–liquid–solid mechanism of single crystal growth. *Appl. Phys. Lett.*, 4:89, 1964.

[7] Tomioka K., Yoshimura M., and Fukui T. A III–V nanowire channel on silicon for high–performance vertical transistors. *Nature*, 488:189–193, 2012.

[8] Larrieu G. and Hanb. X.-L. Vertical nanowire array-based field effect transistors for ultimate scaling. *Nanoscale*, 5:2437, 2013.

[9] Law M., Greene L. E., Johnson J. C., Saykally R., and Yang P. Nanowire dye–sensitized solar cells. *Nat. Mater.*, 4:455–459, 2005.

[10] Garnett E. C. and Yang P. Silicon nanowire radial p-n junction solar cells. *J. Am. Chem. Soc.*, 130:9224–9225, 2008.

[11] Czaban J. A., Thompson D. A., and LaPierre R. R. GaAs core–shell nanowires for photovoltaic applications. *Nano Lett.*, 9:148–154, 2009.

[12] Huang M. H., Mao S., Feick H., Yian H., Wu Y., Kind H., Weber E., Russo R., and Yang P. Room–temperature ultraviolet nanowire nanolasers. *Science*, 292:1897–1899, 2001.

[13] Duan X. F., Huang Y., Agarwal R., and Lieber C. M. Single–nanowire electrically driven lasers. *Nature*, 421:241–245, 2003.

[14] Chin A. H., Vaddiraju S., Maslov A. V., Ning C. Z., Sunkara M. K., and Meyyappan M. Near–infrared semiconductor subwavelength–wire lasers. *Appl. Phys. Lett.*, 88:16115, 2006.

[15] Wang J., Gudiksen M. S., Duan X .and Cui Y., and Lieber C. M. Highly polarized photoluminescence and photodetection from single indium phosphide nanowires. *Science*, 293:1455–1457, 2001.

[16] Park H. G., Barrelet C. J., Wu Y., Tian B., Qian F., and Lieber C. M. A wavelength–selective photonic–crystal waveguide coupled to a nanowire light source. *Nat. Photonics*, 2:622–626, 2008.

[17] Cui Y., Wei Q., Park H., and Lieber C. M. Nanowire nanosensors for highly sensitive and selective detection of biological and chemical species. *Science*, 293:1289–1292, 2001.

[18] Glas F., Hermand J.-C., and Patriarche G. Why does wurtzite form in nanowires of III–V zinc blende semiconductors. *Phys. Rev. Lett.*, 99:146101, 2007.

[19] Joyce H. J., Wong-Leung J., Gao Q., Tan H. H., and Jagadish C. Phase perfection in zinc blende and wurtzite III-V nanowires using basic growth parameters. *Nano Lett.*, 10:908–915, 2010.

[20] Jing Y., Bao X., Wei W., Li C., Sun K., Aplin D. P. R., Ding Y., WAng Z.-L., Bando Y., and Wang D. Catalyst free heteroepitaxial MOCVD growth of InAs nanowires on Si substrates. *J. Phys. Chem.*, 118:1696–1705, 2014.

[21] Mandl B., Stangl J., Hilner E., Zakharov A. A., Hillerich K., Dey A. W., Samuelson L., Bauer G., Deppert K., and Mikkelsen A. Growth meachanism of self–catalyzed gruop III–V nanowires. *Nano Lett.*, 10:4443–4449, 2010.

[22] Robson M. T. and LaPierre R. R. InAs nanowire growth modes on Si (111) by gas source molecular beam epitaxy. *J. Cryst. Growth*, 436:1–11, 2016.

[23] Wang X., Yang X., Du W., Ji H., Luo S., and Yang T. Thickness influence of thermal oxide layers on the formation of self-catalyzed InAs nanowires on Si(111) by MOCVD. *J. Cryst. Growth*, 395:55–60, 2014.

[24] Hertenberger S., Rudolph D., Bichler M., Finley J. J., Abstreiter G., and Koblmuller G. Growth kinetics in postion-controlled and catalyst-free InAs nanowire arrays on Si(111) grown by selective area molecular beam epitaxy. *J. Appl. Phys.*, 108:114316, 2010.

[25] Koblmuller G., Hertenberger S., Vizbaras K., Bichler M., Bao F., Zhang J.-P., and Abstreiter G. Self-induced growth of vertical free-standing InAs nanowires on Si(111) by molecular beam epitaxy. *Nanotechnology*, 21:365602, 2010.

[26] Hertenberger S., Rudolph D., Bolte S., Doblinger M. adn Spirkoska D., Finley J. J., Abstreiter G., and Koblmuller G. Absence of vapor-liquid-solid growth during molecular beam epitaxy of self-induced InAs nanowires on Si. *Appl. Phys. Lett.*, 98:123114, 2011.

[27] Hertenberger S., Rudolph D., Becker J., Bichler M., Finley J. J., Abstreiter G., and Koblmuller G. Rate-limiting mechanisms in high-temperature growth of catalyst-free InAs nanowires with large thermal stability. *Nanotechnology*, 23:235602, 2012.

[28] Janghyuk M., Byeongchan L., Maenghyo C., and Kyeongjae C. Ab initio and kinetic Monte Carlo study of lithium diffusion in $LiSi$, $Li_{12}Si_7$, $Li_{13}Si_5$ and $Li_{15}Si_4$. *Journal of Power Sources*, 328:558–566, 2015.

[29] Obot I. B., Savas K., Cemal K., and Burak T. Density Functional Theory (dft) modeling and Monte Carlo simulation assessment of inhibition performance of some carbohydrazide Schiff bases for steel corrosion. *Physica E: Low-dimensional Systems and Nanostructures*, 80:82–90, 2016.

[30] Wolfram M. *Handbook of Crystal Growth.* 2015.

[31] J. H. Neave, B. A. Joyce, P. J. Dobson, and N. Norton. Dynamics of film growth of GaAs by MBE from Rheed observations. *Appl. Phys. A*, 31:1–8, 1983.

[32] P. R. Pukite J. M. Van Hove, C. S. Lent and P. I. Cohen. Damped oscillations in reflection high energy electron diffraction during GaAs MBE. *J. Vac. Sci. Technol. B*, 1:741, 1983.

[33] Jung J., Bork J., Holmgaard T., and Kortbek N. A. Ellipsometry. Technical report, 2004.

[34] Gomes U. P., Ercolani D., Sibirev N. V., Gemmi M., Dubrovskii V. G., Beltram F., and Sorba L. Catalyst-free growth of InAs nanowires on Si(111) by CBE. *Nanotechnology*, 26:415604, 2015.

[35] Cheng C. and Kunc K. Arsenic adatom structure for Ge(111) and Si(111) surfaces: first-principles calculations. *Surface Science*, 365:383–393, 1996.

[36] Patterson C. H. and Messmer R. P. Structural compromise of the arseinc-terminated silicon (111) surface. *Phys. Rev. B*, 39(2):1372–1374, 1989.

[37] A. Szekeres A. Paneva. Effect of r.f. hydrogen plasma annealing on the properties of Si/SiO_2 interface: a spectroscopic ellipsometry study. *Thin Solid Films*, 433:367–370, 2003.

[38] Tomioka K., Motohisa J., Hara S., and Fukui T. Control on InAs nanowires growth direction on Si. *Nano Letters*, 8(10):3475–3480, 2008.

[39] Marjorie Olmstead A., Bringans R. D., Uhrberg R. I. G., and Bachrach R. Z. Arsenic overlayer on Si(111): Removal of surface reconstruction. *Phys. Rev. B*, 34(8):6041–6044, 1986.

[40] Backer R. S., Klitsner T., and Vickers J. S. Arsenic-terminated silicon and germanium surfaces studied by scanning tunneling microscopy. *Journal of Microscopy*, 152:157–165, 1988.

[41] Patel J. R., Golovchenko J. A., Freeland P. E., and Gossmann H-J. Arsenic atom location on passivated silicon (111) surfaces. *Phys. Rev. B*, 36(14):7715–7717, 1987.

[42] Peter D. Heynes. *Linear-scaling methods in ab initio.* 1998.

[43] `http://cms.mpi.univie.ac.at/vasp/vasp/Algorithms_used_in_VASP_calculate_electronic_groundstate.html`.